MULTI-SENSOR METHODS FOR MOBILE RADAR MOTION CAPTURE AND COMPENSATION

A DISSERTATION SUBMITTED TO THE GRADUATE DIVISION OF THE UNIVERSITY OF HAWAI'I AT MĀNOA IN PARTIAL FULFILLMENT OF THE REQUIREMENTS FOR THE DEGREE OF

DOCTOR OF PHILOSOPHY
IN
ELECTRICAL ENGINEERING

May 2017

By
ROBERT NAKATA

Dissertation Committee:

Victor Lubecke, Chairperson

Olga Boric-Lubecke

David Garmire

Scott Miller

Jan Prinz

ACKNOWLEDGEMENTS

For the wearable sensor motion capture research:

This research was conducted with funding from the US Army under a Phase I SBIR contract. The methods and data are the property of Oahu Group LLC with US government data rights per the contract below.

SBIR DATA RIGHTS

Contract NO. W911QX-13-C-0148

Contractor Name: Oahu Group LLC (DBA Diamondhead Research)

Contractor Address: 455 Anolani St, Honolulu, HI 96821

Expiration of SBIR Data Rights Period: Jan 28, 2019

Team Members and Roles:

For the wearable sensor motion capture research:

Bob Nakata (PI): system design and build, system analysis and test, hardware assembly, sensor fusion, sensor coverage simulations, error sensitivity analysis, IMU analysis, ultrasonic sensor analysis

Isar Mostafanezhad: system design, data processing and analysis, signal processing algorithm, switched phased array antenna

Robbie Nakata: robot arm design and fabrication, tag housing CAD, GUI, ultrasonic sensor test

For the platform stabilization research:

Bob Nakata (PI) with x96 students assisting with Arduino coding and data collection by Brian Haruna, Anh Lam, Alex Lee, Scott Clemens, Arne Nakahara, Dean Kurozumi, Daren Martin and Charles Jarquino.

I’d like to thank my PhD advisor, Professor Victor Lubecke, for his guidance and support on this dissertation research topic. His technical expertise and ability to cultivate working relationships is second to none in my 35 years of working with industry, academia and government colleagues. I would also like to thank my PhD committee members who have guided me through this process. Pursuing this research was a challenge given the many other work, personal and family commitments, but looking back, it was a rewarding journey. I could not have accomplished this without the support and encouragement from my wife, Beth, and from my understanding daughter, Angelina, who sacrificed many weekend beach outings, so to them, I owe a debt of gratitude and dedicate this endeavor to them.

ABSTRACT

Remote sensing has many applications, including surveying and mapping, geophysics exploration, military surveillance, search and rescue and counter-terrorism operations. Remote sensor systems typically use visible image, infrared or radar sensors. Camera based image sensors can provide high spatial resolution but are limited to line-of-sight capture during daylight. Infrared sensors have lower resolution but can operate during darkness. Radar sensors can provide high resolution motion measurements, even when obscured by weather, clouds and smoke and can penetrate walls and collapsed structures constructed with non-metallic materials up to 1 m to 2 m in depth depending on the wavelength and transmitter power level. However, any platform motion will degrade the target signal of interest. In this dissertation, we investigate alternative methodologies to capture platform motion, including a Body Area Network (BAN) that doesn't require external fixed location sensors, allowing full mobility of the user. We also investigated platform stabilization and motion compensation techniques to reduce and remove the signal distortion introduced by the platform motion. We evaluated secondary ultrasonic and radar sensors to stabilize the platform resulting in an average 5 dB of Signal to Interference Ratio (SIR) improvement. We also implemented a Digital Signal Processing (DSP) motion compensation algorithm that improved the SIR by 18 dB on average. These techniques could be deployed on a quadcopter platform and enable the detection of respiratory motion using an onboard radar sensor.

Table of Contents

Table of Figures

1.0 Introduction and Background

Multi-sensor systems can be used to capture and compensate undesirable platform motion and thereby enable the isolation of motions of interest using a remote sensing radar. Radar sensors measure target motion and any unintentional motion of the radar sensor itself will corrupt the target signal. A motion capture system that accurately senses position enables the use of a radar sensor from a non-stationary platform. Such a system can be used for radar remote sensing in battlefield triage scenarios without endangering medics, for search and rescue operations of victims buried under collapsed structures and for situations where adversaries may be hiding behind a wall.

This dissertation describes the motivation and need for multi-sensor motion capture and motion compensation when using a radar sensor. We first describe a case study for a wearable sensor system that monitors human body kinematics. For the second case study, we describe methods that enable the isolation of the motion of interest, such as respiratory motion, using a radar sensor on a platform that has unwanted motion that corrupts the signal.

Motion capture of human body kinematics has applications for the military, first responders, sports performance monitoring, physical therapy, movie animation and the gaming industry [1]. Existing commercially available body motion capture sensors include fixed location camera based systems [2], IMU based sensors [3] and Ultra Wide Band (UWB) sensors [4]. Infrastructure based sensors such as cameras and RF localization sensors are limited by range of coverage and require fixed location external sensors that limit the mobility of the tracked subject. Wearable IMU sensors have performance limitations due to accumulated accelerometer drift and magnetic field distortions resulting in position errors. While UWB sensors have the capability for high temporal resolution given their wide bandwidth, pulse distortion due to RF interaction with the body, compromises the Time of Flight (ToF) accuracy leading to imprecise position measurements [4].

To overcome these limitations, a stand-alone system that permits mobile motion capture has been developed using sensor fusion of RF Direction of Arrival (RFDOA) and Inertial Measurement Units (IMUs). This part of the research was sponsored by the US Army under a Phase I SBIR grant [5].

A Proof-of-Concept (POC) RFDOA prototype for motion capture was designed and built using a 16 element switched phased array antenna that measures the amplitude and phase of a RF signal emanating from tags attached to a moving appendage, simulated by a robotic arm that provides a position reference. Measured results were a position mean error of 0.1 degrees with respect to the robot arm reference.

The RFDOA measurements were combined with an IMU embedded in the tag attached to the robot arm. Sensor fusion combines each output to compensate for IMU errors and RF shadowing.

Similar techniques can be implemented for motion compensation of a mobile or handheld platform where the primary sensor payload requires a stable measurement platform. An Unmanned Aerial Vehicle (UAV) platform is subject to unwanted motion due to aerodynamic disturbances, resulting in the corruption of phase sensitive signals of interest detected by on-board radar sensors. Platform stabilization enables the deployment of a radar sensor on a UAV capable of detecting respiration vital signs on immobilized victims. Platform motion was emulated using linear motion actuators in the laboratory where the platform motion was reduced using a secondary ultrasonic or radar sensor embedded in a feedback control loop. The platform motion was reduced to an acceptable level to allow additional motion compensation with baseband signal processing using sensor fusion from a secondary radar sensor. For a quadcopter platform, a feedback stabilization system can cancel the extraneous platform motion by applying an error control voltage to the Electronic Speed Controllers (ESC) that adjusts the thrust of each quadcoptor motor, thereby stabilizing the platform. For this investigation, we tested the platform stabilization and motion compensation algorithms using a laboratory bench top test setup with linear actuators simulating the platform motion and platform stabilization counter motion.

For baseband signal processing motion compensation, phase compensation proportional to the platform motion can cancel the in-range motion component. Phase delay measurements between adjacent multi-element antenna arrays can be used to determine Direction of Arrival (DOA) and stabilize the platform in the cross-range direction. As an alternative, the Received Signal Strength Indication (RSSI) can be used to track the cross-range position and apply an error signal in a feedback loop to maintain a position directly over the target. A Commercial-Off-the-Shelf (COTS) radar transceiver was used to evaluate the in-range motion compensation algorithm and DOA measurement capability. Motion compensation can use some of the same sensors used for motion capture. See Figure *1*.

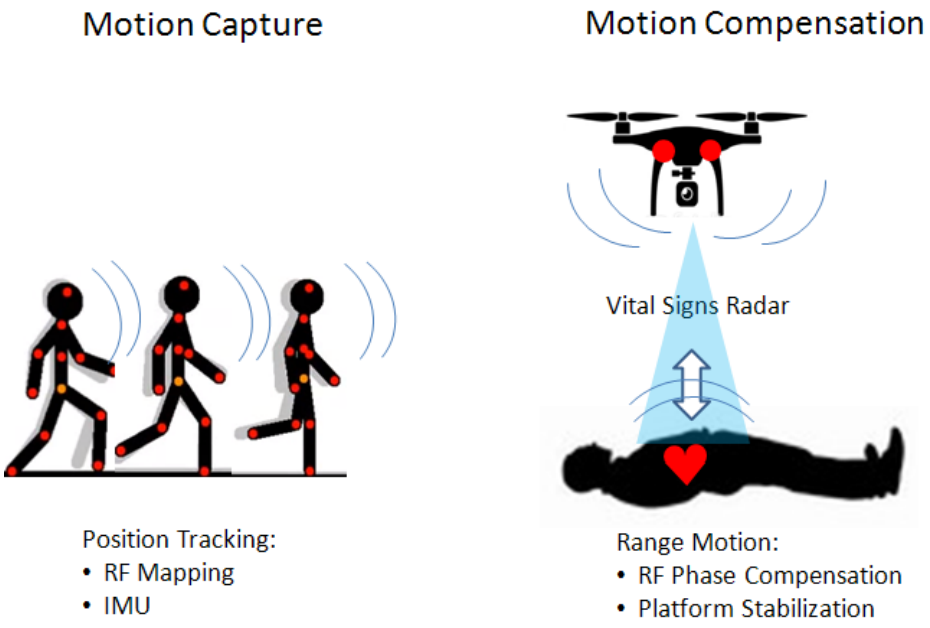

Figure 1. Motion capture and motion compensation. Sensors allow precise body motion tracking and radar detection of vital signs motion from a mobile platform.

The Proof-of-Concept (POC) motion capture system requirements are described in Section 6 to Section 9. The hardware and software design for the POC system are described in Section 10 to Section 15. The design leveraged Commercial-Off-the-Shelf (COTS) components to minimize the development time (6 months Phase I SBIR contract period of performance). A COTS software defined radio was adapted for the receiver and a custom switched antenna array was built. Section 15 summarizes the

POC system performance that demonstrated the concept. Empirical measurements of the COTS IMU module confirmed the need for sensor fusion with the RFDOA sensor to overcome the limitations of the IMU.

The background and motivation for motion compensation that enables a mobile radar vital signs sensor is described in Section 16. Section 17 provides an overview of position sensor technologies. Sensor fusion design considerations are described in Section 18 followed by a discussion of the methods developed for platform stabilization and motion compensation algorithms in Section 19 to Section 22. Experimental results are summarized in Section 23 to Section 25 with conclusions and future work described in Section 26 and Section 27.

2.0 Wearable Motion Capture Sensor Background

The objective of this part of the investigation is to evaluate and demonstrate the feasibility of producing a wearable high resolution sensor system Body Area Network (BAN) to monitor body motion with a self-contained system that doesn't require external fixed location sensors. Such a self contained sensor network would allow the user to capture their body motion while mobile without being constrained to the field of view of fixed location external sensors. Applications include virtual reality gaming, virtual collaboration, physical therapy monitoring and military training. For example, the military could monitor soldier body dynamics to assess and evaluate training and battlefield performance of the dismounted soldier.

Existing solutions rely on camera based systems with line-of-sight limitations resulting in confined measurements or rely on Inertial Measurement Units (IMUs) which are prone to noise and drift, resulting in position inaccuracies. We designed, built and evaluated a wearable sensor network based on a hybrid combination of Radio Frequency (RF) positioning sensors combined with Micro Electro Mechanical System (MEMS) based IMU sensors. The combined sensors provide performance advantages over that of a single sensor, e.g., the RF derived position information can compensate for the IMU drift using sensor fusion.

Successful development of the proposed system will provide the military with an operational capability to monitor soldier dynamics during training and combat missions. Commercial applications include gaming, sports performance assessment, robotics and medical kinesiology applications including biomechanics, prosthetics, occupational health and rehabilitation monitoring.

Many approaches have been developed for accurate real time position tracking of an object. These solutions can be categorized as inertial or dead reckoning navigation, and absolute position measurement systems. These include Inertial Measurement Units (IMUs), camera based systems or Radio Frequency (RF) positioning using trilateration for geolocation.

An IMU sensor combines the outputs from an accelerometer, gyroscope and magnetometer to determine the yaw, pitch and roll (YPR) of the object to which it is attached. The multiple sensors are fixed relative to each other, and are thus able to provide readings from a single body. Post processing is required to combine the sensor signals into useable coordinates for localization. This results in a degree of uncertainty that increases over large movements or long time spans due to the susceptibility of IMUs to integration noise that creates drifting.

Camera based systems comprise multiple cameras that visually track a certain feature or physical marker attached to an object. Typical body tracking systems require many markers to be externally attached to a user to determine an accurate reading. These markers can interfere with movement patterns and can be easily obstructed from the view of the camera. Furthermore, this type of system requires that the user be within the viewing range of the cameras, restricting the user to a confined, indoor environment.

Traditional RF and ultrasonic positioning sensors measure the Time-of-Flight (ToF) of signals transmitted from radio transmitters to a receiver given that a RF signal propagates at the speed of light and an ultrasonic signal propagates at the speed of sound between the transmitter and the receiver. Based on this time difference and the speed at which the signal travels, the relative distance can be determined between the transmitter and receiver. By using multiple signals at multiple frequencies, emitted from multiple transmitters, it is possible to trilaterate the exact position of the receiver with respect to the transmitters. This approach, referred to as Time Difference of Arrival (TDOA), is what the Global Positioning System (GPS) uses for geolocation. The issue with this type of system is that radio signals travel at the speed of light which makes the measurement of the time of transmission and time of arrival difficult to measure for the short ranges in a BAN and requires precision synchronized system clocks at each node.

Acoustic positioning systems operate on a similar principal as radio frequency systems but utilize acoustic signals instead of radio signals. The advantage is that acoustic signals travel at the speed of sound which is orders of magnitude slower than the speed

of light. This makes time of flight signal calculations relatively simple. The disadvantage of acoustic signals, especially those operating in the ultrasonic frequency, is the tendency for the signals to echo, causing multipath signals and potentially corrupting any distance measurements.

3.0 Requirements

The requirements for the Wearable Sensor Network are summarized in Table 1. Requirements Traceability Matrix (RTM)below.

Table 1. Requirements Traceability Matrix (RTM)

	Requirements	Derived Requirements	Requirements Compliance
1	The U.S. Army requires a system that can measure the 3-D position, velocity and acceleration of the Soldier's head, trunk, limbs and equipment using small, lightweight sensors that don't interfere with uniforms, body armor, or equipment.	Measure position and velocity on the head (possibly a sensor attached to the helmet), trunk (receiver array attached to the chest) limbs (sensors attached at the anterior rotator cuff, interior forearm at the elbow and inside wrist), legs (below the anterior hip joint, above the anterior knee joint) and torso.	We have demonstrated the capability to measure position, velocity and acceleration using a reference robotic arm on a benchtop testbed.
2	The system must be accurate to 0.5mm within a local coordinate system for the position of body segments and equipment.	Use a hybrid combination of MEMS IMU sensor and RF positioning in each sensor to achieve .5mm accuracy.	Position accuracies for the RF phase technique demonstrated 0.5mm position accuracy.

Table 2. Requirements Traceability Matrix (continued)

	Requirements	Derived Requirements	Requirements Compliance
3	The system and software need to provide, derive, or integrate the following signals to sufficiently capture each Soldier's movement: linear and angular acceleration, linear and angular velocity, position and orientation, joint torques and segment kinematic energy.	Use a 6 Degree of Freedom (DOF) IMU to measure x,y,z axes and yaw about each axis. Use RF positioning sensor to compensate for IMU drift. Compute torque and kinematic energy from sensor outputs.	GUI displays acceleration, velocity, position, orientation and joint torques. Kinematic energy can be derived.
4	In addition to the body kinematics, the system would be used to monitor the movement of the weapon and to track the weapon aim trace. At 25 m, the accuracy of the weapon aim point at the target should be 1.0 cm.	Apply 2 sensors to determine aim: one sensor at rifle butt and second sensor below the rifle barrel tip. Pointing accuracy = arctan (.01/25) = .0229 deg pointing accuracy	To be verified.

Table 3. Requirements Traceability Matrix (continued)

	Requirements	Derived Requirements	Requirements Compliance
5	This data should be transmitted wirelessly and viewable in real-time, as well as saved to a computer.	Use WiFi backhaul using 802.11 WiFi modem chipset embedded in the Main Processor Unit (MPU) Develop GUI application for ruggedized Smartphone, tablet, laptop (e.g. Panasonic Toughbook)	Demonstrated WiFi connectivity between Proof-of-Concept (POC) MPU and display computer.
6	The system should be weatherproof, rugged for data collection in any environment, and not impede Soldier movement. The system needs to attach firmly to the body, be resistant to breakage, loosening, and minimize motion artifact.	Use sealed sensor housing to meet IPX liquid intrusion standard. Sensor is attached directly to skin using biocompatible adhesive backed flexible foam substrate that retains the tag sensor assembly.	Ruggedized, IPX design to be completed during commercialization. Custom designed skin compatible substrates have been obtained from medical grade supplier.
7	Each sensor should be 2 cm x 2cm or smaller, and weigh less than 5 grams, including the rechargeable battery.	Preliminary power consumption, battery capacity sizing and component sizing indicates SWaP requirement is achievable. This will be confirmed with the prototype.	SWaP requirements are achievable – To be finalized during product development.

Table 4. Requirements Traceability Matrix (continued)

	Requirements	Derived Requirements	Requirements Compliance
8	The system should include a graphical user interface (GUI) for experimenter to use when collecting and processing data, as well as access to source code for data analysis. The GUI should run on a tablet, smartphone or other portable device. The GUI should provide a means to initialize/calibrate the sensor array, view sensor data and any calculated variables in real time, extract/download raw data from the sensors and export both raw and processed data for further processing in other software packages (e.g. MS Excel, Matlab).	The GUI will be defined during the system design portion and coded for the prototype. See screenshots under GUI description.	A simple stick figure GUI was built that demonstrated real-time tracking of the robotic arm motion.

Table 5. Requirements Traceability Matrix (continued)

	Requirements	Derived Requirements	Requirements Compliance
9	PHASE I: Develop hardware for body worn sensor array and approaches for analyzing 3-D segment and joint kinematics. A prototype system is expected at the end of phase I.		A POC prototype was designed and constructed to demonstrate 3D segment motion tracking.

4.0 Technical Objectives

The specific objectives of this part of the investigation were to:

1. Design the hybrid IMU and RF positioning sensor network prototype.
   The Main Processor Unit (MPU) design, including the antenna array, is discussed in Section 10. The tag design, including the IMU, is discussed in Section9.0. The GUI design and functions are discussed in Section 10.0.
2. Conduct Matlab simulations of the expected system position accuracy including determination of optimum placement of receiver antenna array (to provide a fixed reference) and number and placement location of limb sensors. Details are discussed in Section 9.0.
3. Assess achievable size and weight constraints for the sensor based on sensor and battery cell watt-hour requirements. The tag Size, Weight and Power (SWaP) for the POC system and targeted SWaP for the production units are discussed in Section 9.0.
4. Build prototypes of the hybrid IMU and RF positioning sensors and measure actual position accuracies. See Section 15.0.

5.0 System Concept

We have developed a Proof-of-Concept (POC) hybrid wearable sensor network comprising IMUs and a RF positioning system. By incorporating two different positioning systems (IMU and RF), the sensors can provide accurate positioning data over a range of movements. For situations where the RF signals are directly blocked by an object, or are otherwise obstructed by the body, the IMU can be used solely for tracking. In the typical situation, where RF signals are visible, the positions reported from each sensor can be both used in a sensor fusion algorithm. This will help to further decrease inaccuracies in the final reported position of each tag.

In the operational system, small form factor tags are attached to the user's limbs and a receiver array is worn on the chest to provide accurate position, velocity and acceleration information. See Figure 2.

Each tag is attached at various locations on the body and incorporates a Micro-Electro-Mechanical Systems (MEMS) Inertial Measurement Unit (IMU) combined with a modulated RF positioning beacon that transmits a Continuous Wave (CW) RF signal. The modulated signal allows for identification of each tag via a preamble sequence unique to each tag. This RF signal is used for calculating RF Direction of Arrival (RFDOA) and RF phase information from each tag to the body worn receiver array. IMUs are prone to position drift which can be compensated with the RF positioning information. This hybrid combination of the RF and IMU sensors provides for a robust solution that leverages the performance advantages of each technology, thus providing a more accurate and robust kinematics measurement and tracking capability than either sensor alone.

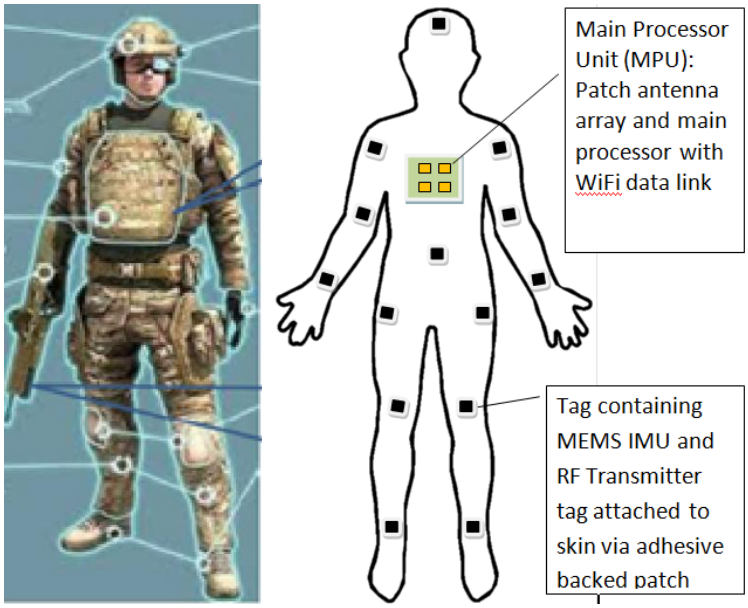

Figure 2. Wearable wireless sensor network. Distributed tags provide position information via an integrated IMU and RF transmitter contained in each tag. The MPU computes tag positions via Direction-of-Arrival (DOA) and range determination via the demodulated phase of the RF positioning signal to correct the IMU drift.

As demonstrated in previous work, Doppler radar provides precise (< 0.5mm) position measurements since it uses phase measurement comparisons between the transmitted and received waveforms. In our approach we will use a RF positioning system that is similar to Doppler radar but does not rely on backscatter from an object, instead the RF path exists between the transmitting tag and the receiver array. Since it is a Continuous Wave (CW) waveform, synchronized system clocks at each tag are not required, thus simplifying the system compared to a pulse radar or time of flight RF system.

The Main Processor Unit (MPU) collects the tag data via the multi-element antenna array and forwards the data via a WiFi connection between the receiver array controller and the external remote computer that displays the data on a Graphical User Interface (GUI). The system block diagram is depicted in Figure 3.

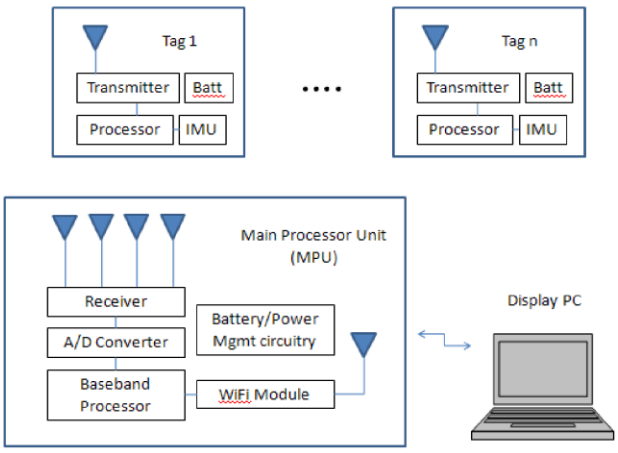

Figure 3. System block diagram for the Wearable Sensor Network. Tags transmit Continuous Wave (CW) RF signal and Inertial Measurement Unit (IMU) data. Main Processor Unit (MPU) determines tag positions using phase demodulation of the received RF signal and IMU data and transmits the position data via WiFi to the display computer.

6.0 Main Processor Unit (MPU) Design

The MPU comprises the phased array antenna and receiver, the 2.4 GHz RF transmitter that is distributed to each tag using a programmable RF switch, and a laptop PC that collects, processes and transmits the data to the display PC. The MPU block diagram is shown in Figure 4 and component layout is shown in Figure 5.

For the prototype, we chose to simplify the system by placing the tag RF switch in the MPU rather than in each tag. We also powered the system via an AC/DC power supply to eliminate the need for a battery sub-system. The MPU computer uses an external laptop running the Linux Ubuntu Operating System.

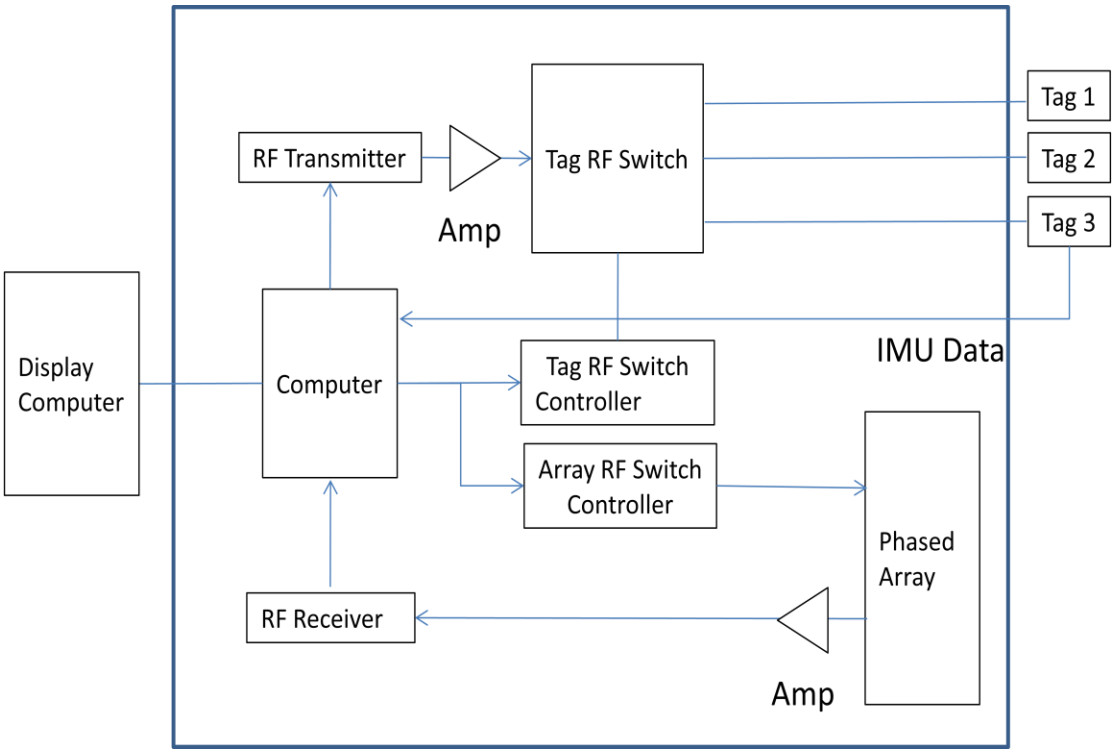

Figure 4. MPU POC block diagram

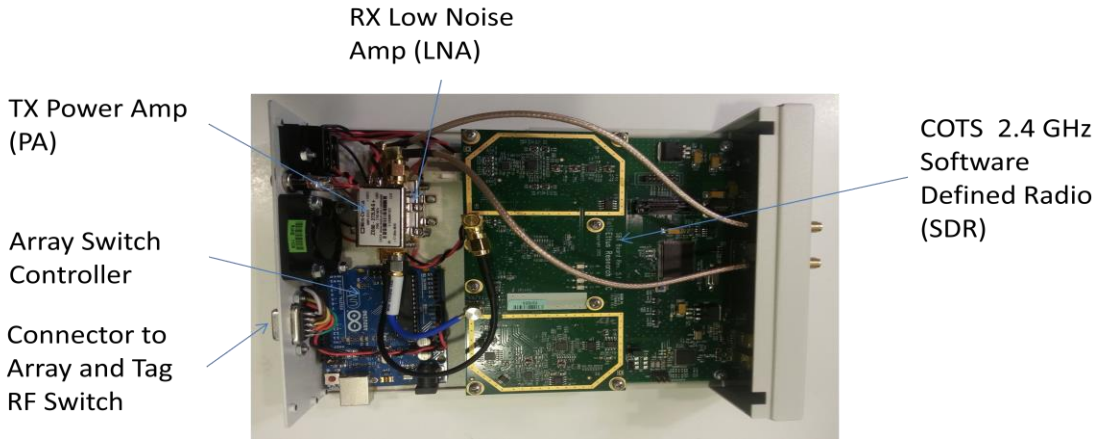

Figure 5. Main Processor Unit (MPU).
MPU components integrated into a COTS Software Defined Radio (National Instruments USRP N200) housing including receiver LNA, transmitter PA and array switch controller.

7.0 Antenna Array Design

The MPU phased array antenna will determine the RFDOA and RF phase of each received tag RF signal. Using a switched antenna array eliminates the need for multiple receiver channels and therefore reduces the Size, Weight and Power (SWaP) and cost of the system. However, the hardware and signal processing complexity is increased to demultiplex the individual channels.

The antenna array was designed to operate at the 2.4 GHz ISM band to leverage the availability of Commercial-Off-the-Shelf (COTS) components. This resulted in an array dimension of 11 x 11 inches which is larger than a commercialized version that would likely operate at 24 GHz. Existing 24 GHz arrays have dimensions that are approximately 4 inches x 4 inches.

We designed a switched array using Single-Pole-4-Throw (SP4T) RF switches for each 2x2 subarray and another SP4T switch to select one of the four sub-arrays. The array was simulated and designed using a RF CAD tool based on the performance requirements, including operating frequency, bandwidth, phase linearity and DOA angular resolution.

The layout was designed for a center frequency of 2.43 GHz using a 62 mil thickness conventional FR-4 dielectric substrate printed circuit board. We used a two layer board design. The appropriate width for the 50 ohm impedance lines was calculated to be 123.75 mil and implemented in the design. The micro-strip patches were designed to resonate at 2.45 GHz resulting in dimensions of 1471.25 mil x 1133.00 mil. In this design, due to space limitations, we used an inset feed instead of the more conventional impedance transformer. The inset feed results in a more compact design. The inset length was calculated at 423.50 mil for this frequency and substrate. In order to maintain 50 Ohms across all lines, we used arc transitions at bends to minimize unwanted reflections.

Figure 6 shows the top layer of the array design where patch elements and feed lines are visible. The bottom layer is an all conductor ground plane layer and is hidden for clarity.

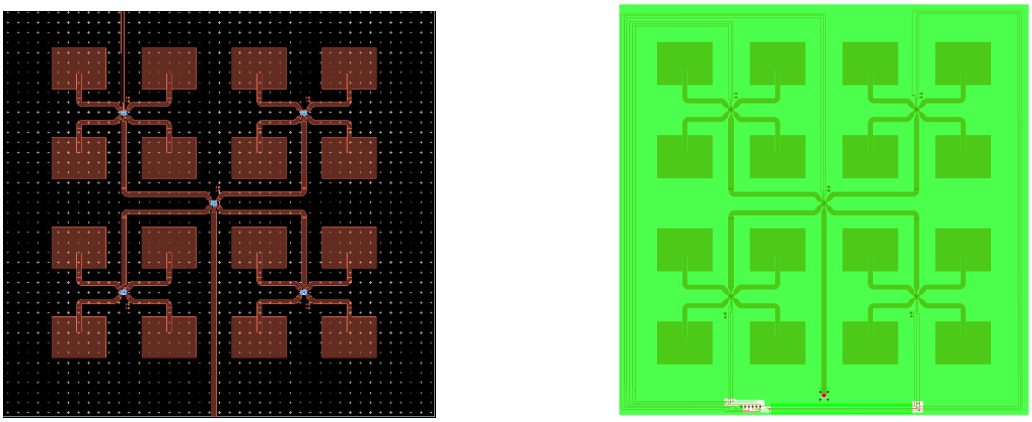

(a) (b)

Figure 6. Phased array antenna.
(a) Preliminary board layout used for EM simulations. (b) Board layout of the MPU 4x4 phased antenna array. Larger traces are the RF feed lines and smaller traces are the switch control and power lines.

The assembled board and switch network is shown in Figure 7.

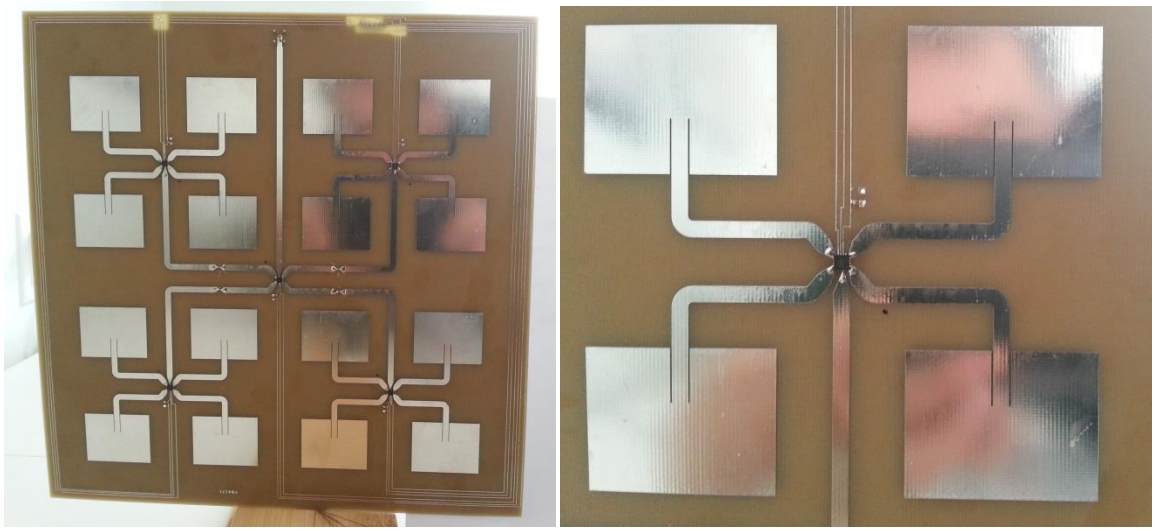

Figure 7. Phased array PCB antenna.
(a) Assembled phased array antenna board with RF feed, RF switches and control lines. (b) Closeup view of 2x2 subarray and switch.

7.1 RF Phase Demodulation Characterization

To achieve a radial motion tracking accuracy of 1mm, we require a phase demodulation measurement accuracy of 2.9 degrees of the RF wavelength (See Table 6. Phase precision requirements.). This is determined from the physical wavelength of 0.125 m at 2.4 GHz.

Table 6. Phase precision requirements.

Parameter	Relationship	Value	Units
frequency	f	2.4	GHz
wavelength	λ = c/f	0.125	m
spatial precision	requirement	0.001	m
phase precision	derived	2.9	deg

We characterized the RF phase demodulation accuracy by measuring the position of the tag antenna using the demodulated RF phase at the receiver. The phase derived position waveform was compared to the position waveform as measured by a potentiometer attached to a linear actuator that serves as a reference. See Figure 8. RF phase versus range. The Root Mean Square (RMS) difference is 0.075 cm, the mean difference is 0.02 cm. and the Standard Deviation (SD) of the difference is 0.07 cm, confirming that the RF phase measurements are highly accurate. For higher frequency changes in position, the sample rate can be increased up to several KHz to detect the change in position.

Because Doppler radar has range ambiguity, additional information is required to determine the absolute range. As shown in a later section, RF mapping provides position information by mapping the phase and amplitude response at each spatial position. The phase demodulation capability is implicit in the phased array antenna response and the signal processing for the combined phase demodulation and RFDOA provides the measured position.

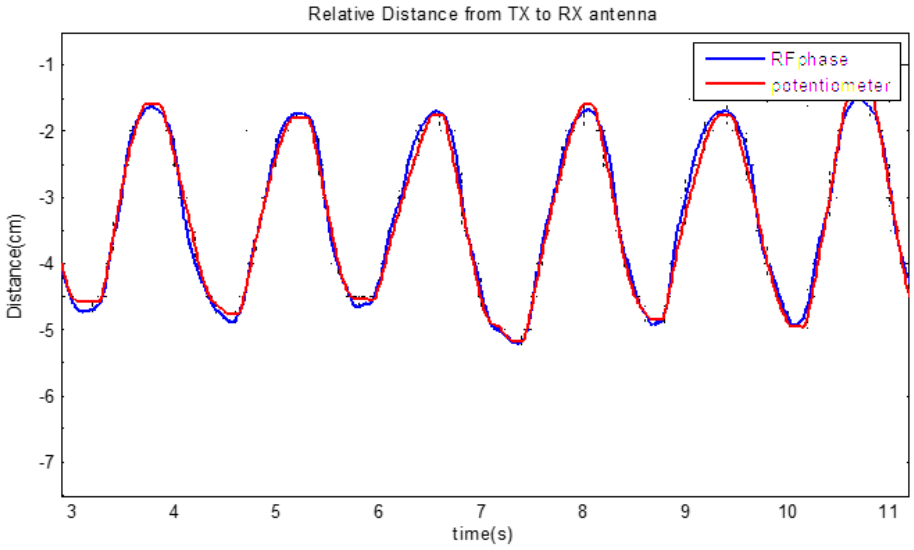

Figure 8. RF phase versus range.

Plot of measured distance from the TX to RX antenna using two different methods - RF phase delay and a potentiometer attached to a linear actuator to provide a position reference.

7.2 Array Direction of Arrival Characterization

Since the phased array antenna will determine the RFDOA of the received tag signals and given the mutual coupling effects present in the array, we characterized the amplitude and phase response of the antenna array over the range of its usable azimuth and elevation angles. Figure 9 shows the coordinate system used for the measurements.

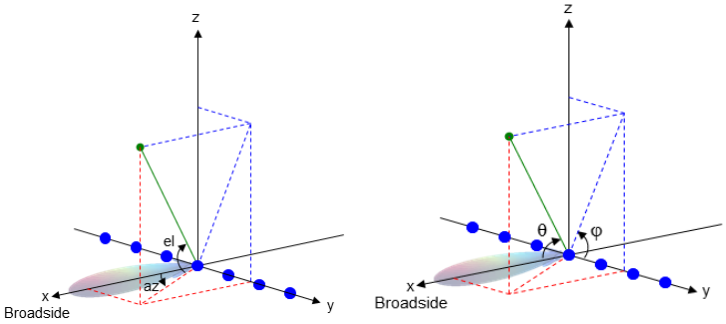

Figure 9. Array DOA geometry.

Definition of azimuth, elevation, phi and theta angles and the geometry used for the array.

We measured the array's actual pattern and use that information to create the position estimation algorithm to determine the DOA as summarized in the RF DOA test results in section 15. We assembled the array on the robotic platform as shown in Figure 10 and measured the array antenna pattern using automated azimuth and elevation sweeps.

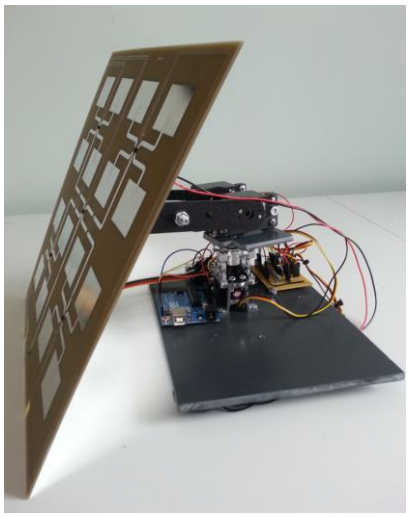

Figure 10. Antenna array testbed.

Antenna array test bed using robotic arm to step the array in pre-determined angular azimuth and elevation steps to measure the individual antenna element gain and phase response.

Based on the antenna pattern information and using the Maximum Likelihood (ML) criteria, we were able to determine the DOA for each tag position using the simulated antenna pattern.

The general Maximum Likelihood (ML) problem can be formulated by first starting with a signal model. We can define the received signal model as:

$$r = S(\theta) + n \tag{1}$$

where *r* is the antenna output, θ is the vector of arrival angles (DOA) and *n* is the noise matrix. *S* defines the sensor array's behavior, in this case it is a function of individual antenna patterns and DOA.

The log likelihood function is defined as:

$$L(\theta) = -\frac{k}{2}\ln 2\pi - \frac{k}{2}\ln \det K_n - \frac{1}{2}\{[R - S(\theta)]^T K_n^{-1}[R - S(\theta)]\} \quad (2)$$

where K_n is the noise covariance matrix and *k* is the number of sensors. For a maximum likelihood estimate (ML) the goal is to find θ_{ml} such that $L(\theta)$ is maximized so that

$$\frac{\partial L(\theta)}{\partial \theta} = 0\ , \theta = \theta_{ml} \quad (3)$$

For a case where *S* is a linear function of θ, this derivative can be calculated fairly simply and there exists a closed form solution. For the case where *S* is non-linear we need to revert to searching a lookup table for ML criteria. Due to the dimension of the problem and the fact that the antenna patterns are non-linear functions of DOA, we created a Maximum Likelihood estimator, $L(\theta)$, for all possible DOAs using the simulated antenna pattern. We were able to calculate the DOA of an impinging wave from a tag signal source based on this approach. An example scatter plot is shown in Figure 11.

We calculate RF DOA based on the likelihood surface. The peak of the likelihood surface will determine the position. Determining the peak accurately will require having a sharp and well defined maximum. This will not always be the case and hence there will be an ambiguity surface. Figure 11 shows the ambiguity surface for the actual and estimated locations. The ambiguity surface can be calculated while position estimation is in progress and can be an indication of how accurate and reliable the position estimate is.

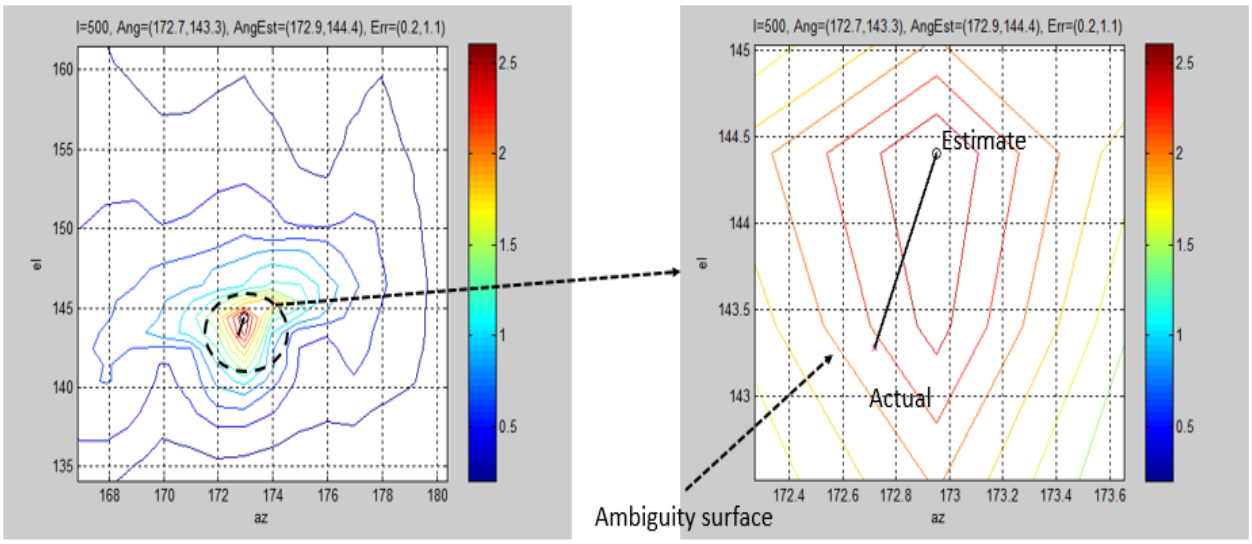

Figure 11. Maximum likelihood surface contours.
Log likelihood contour surface for the ML estimation algorithm. A sharper gradient of the ambiguity surface increases the estimation accuracy.

8.0 Sensor Fusion Algorithm

The sensor data fusion flow diagram is shown in Figure 12 below. The position output is a weighted linear combination of the IMU, RF Phase Modulation (PM) and RFDOA sensor inputs. The sensor input values are weighted by a scaling factor depending on the estimated angular position to account for the measurement accuracy of each sensor input. The weight factors, W_n, n = 1 to 6, are empirically derived to minimize the position estimation error with respect to the reference measurements reported by the robot forward kinematic position. A candidate spatial distribution of the weighting factors is depicted in Figure 13.

In the future, we plan to determine the values for the weights, W_n, by comparing the position errors of the IMU versus the position errors of the RF DOA/RF PM as a function of spatial position. Once we have characterized the spatial distribution of position errors, we will assign higher weights to the more accurate sensor and lower weights to the lower accuracy sensor.

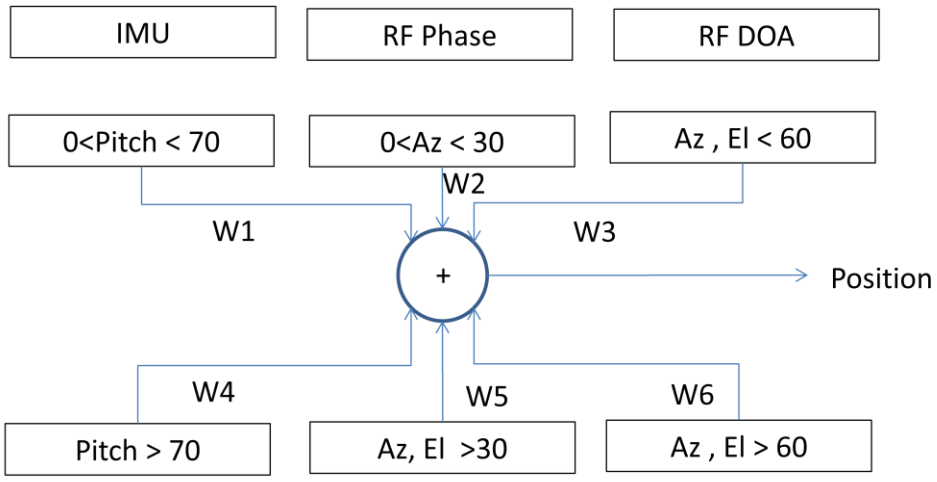

Position = W1*IMU+W2*RFP+W3*RFDOA+W4*IMU+W5*RFP+W6*RFDOA

Figure 12. Sensor fusion algorithm flow diagram.

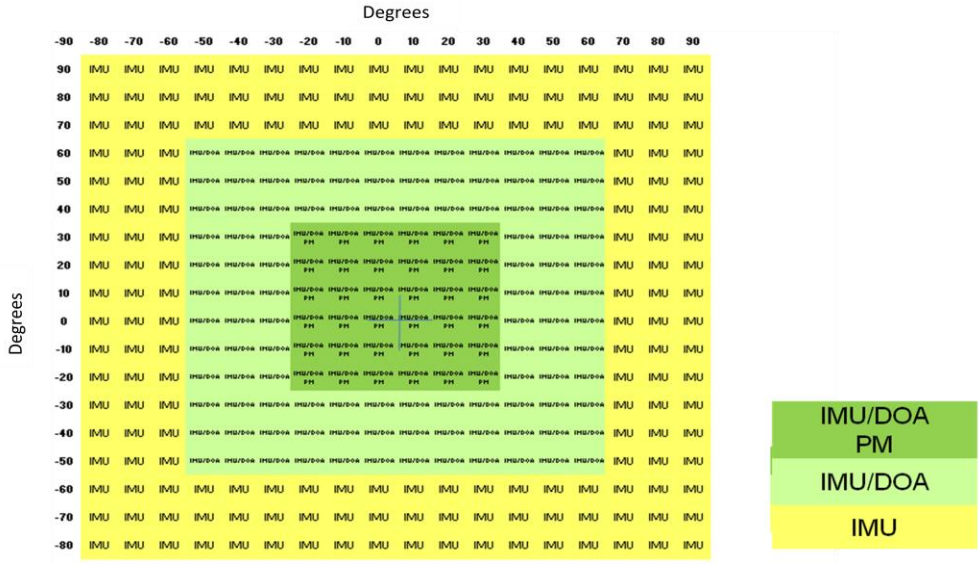

Figure 13. Sensor fusion spatial distribution.
Example of spatial distribution of sensor inputs (IMU, IMU+DOA, IMU+DOA+PM) used in the position estimation algorithm (PM = Phase Modulation).

9.0 Tag Design

The tag design comprises a Commercial-Off-The-Shelf (COTS) IMU and a stub antenna. For the POC system, the antenna is connected via a coaxial cable to a 3 way RF switch in the MPU that sequentially switches each tag RF signal. The sequential switching permits time division multiplexing multiple tag transmissions from a common RF source to determine the location of each tag via the RF beacon. A block diagram is shown in Figure 14.

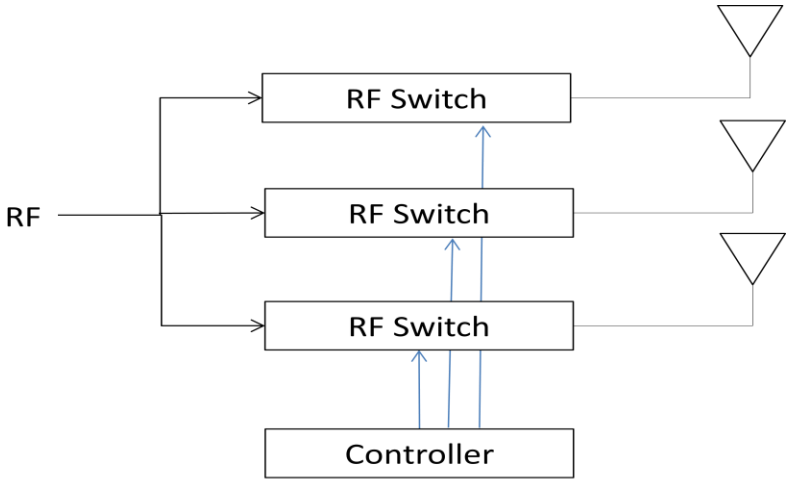

Figure 14. Multiple tag block diagram with controller for time division multiplex beacon transmission.

9.1 IMU

The IMU is based on the Sparkfun 9 degree of freedom Razor that uses the Analog Devices ADXL accelerometer, gyro and magnetometer. Because all IMUs are prone to position errors as a result of double integrating a noisy accelerometer sensor, we chose to rely on the yaw, pitch and roll derived from the accelerometer, gyro and magnetometer sensors in the IMU to provide the tag orientation and position. When attached to the robot test fixture, the IMU pitch angle corresponds to the elevation angle and the IMU yaw angle corresponds to the azimuthal angle.

To validate the POC system, we designed and fabricated a 3 axis, dual segment robotic arm that provides reference azimuthal and elevation angles. The robotic arm was used to re-position the IMU/RF antenna tag in controlled experiments and the robot's forward

kinematic derived positions are compared with the IMU/RF position estimates as shown in Section 15.

To derive the segment end point positions and segment angles, the following forward kinematic equations are applied to the reported IMU angles where θ1= upper arm elevation angle and θ2 = lower arm elevation angle (The robot arm shoulder is at the base of the robot platform, thus L1 is the upper arm and L2 is the lower arm).

$$(x1, y1) = (L1\cos(\theta 1), L1\sin(\theta 1)) \quad (4)$$

$$(x2, y2) = ((L1\cos(\theta 1) + L2\cos(\theta 2), L1\sin(\theta 1) + L2\sin(\theta 2)) \quad (5)$$

$$\text{Segment angle} = 180 - \theta 2 + \theta 1 \quad (6)$$

Figure 15 shows the geometry of the robot arm segments in the vertical plane. A sensitivity analysis was completed to determine the position error as a function of IMU angular error. An angular error of 1 degree corresponds to 2.7mm at the segment joint (x1, y1) while a 5 degree angular error corresponds to a 13.3mm error at the distal segment end point. See Table 7. Position errors.These IMU errors are corrected by the RFDOA and RF phase information in the sensor fusion processing described in section 12.

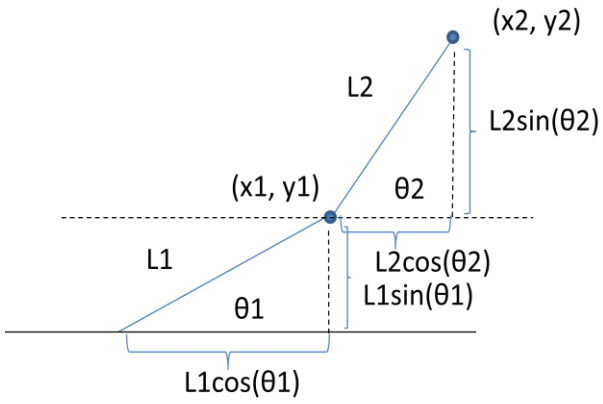

Figure 15. Arm vertical plane geometry for inverse kinematics equations.

Table 7. Position errors.

Distal segment position errors for corresponding IMU angular errors for IMU attached to robot upper (L1) and lower arm (L2), e.g. 1 deg of IMU error produces 2.7 mm error for L1 position at (x1,y1).

Segment	Arm Length (mm)	1 deg IMU error (mm)	2 deg IMU error (mm)	5 deg IMU error (mm)
L1	152.4	2.7	5.3	13.3
L2	167.3	2.9	5.8	14.6
L1+ L2	319.7	5.6	11.2	27.9

9.2 Low Phase Noise RF Transmitter

During the evaluation phase of the RF tag design, we discovered that the RF phase noise was excessive and masking the desired RF phase demodulation corresponding to the tag motion. This issue was resolved by sharing the same RF reference source for both the tag transmitter and the receiver using coaxial lines between the MPU and the tags. This architecture validates the system concept and the RF phase noise issue is addressed in the low noise design described below. The wired approach has the added benefit of removing the need for batteries in the tags for the POC system.

Phase noise is typically characterized as the power spectral noise level relative to the carrier frequency or dB down from the carrier (dBc) at a specified offset frequency. In our case, we are interested in the phase noise at 1 Hz offset from the carrier. The overall phase noise contribution from the Phase Locked Loop (PLL) is given by:

$$PN_{PLL} = 20*\log10(f_{out}/f_{ref}) + PN_{ref} \quad (7)$$

where f_{out} = carrier frequency = 2.4 GHz and f_{ref} = crystal oscillator frequency and PN_{ref} = TCXO phase noise.

For the selected TCXO, the reference phase noise level, PN_{ref}, is specified as -65 dBc. Substitution yields:

$$PN_{PLL}=20*\log10(2400/10) - 65= \text{ -37 dBc/Hz} \quad (8)$$

$$\text{RMS Phase Jitter (deg) = Sqrt}[2*10^{A/10}] * 57.3 \quad (9)$$

where A is the integrated phase noise power (dBc) of the PLL.

Substitution of the PLL phase noise value of -37 dBc/Hz yields 1.1 deg, which is within our phase noise jitter requirement. This level corresponds to an acceptable level of phase noise that permits position detection with sub-millimeter spatial resolution. Given this analysis, we identified the Analog Devices ADF4360 synthesizer with the -65 dBc PN_{ref} TCXO and plan to design and fabricate the tag transmitter based on this component during future product development. See Figure 16. Low phase noise frequency synthesizer.

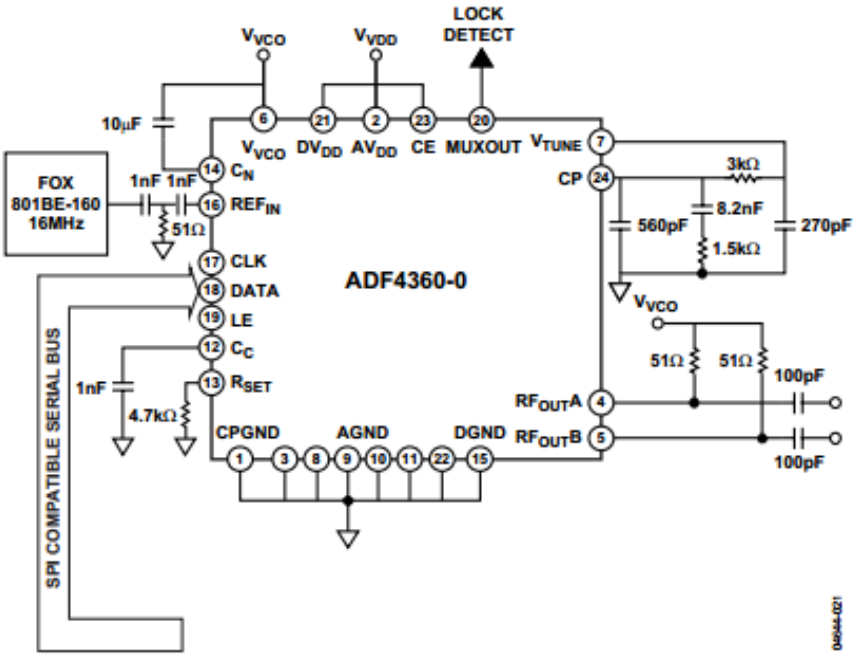

Figure 16. Low phase noise frequency synthesizer.
Analog Devices ADF4360 frequency synthesizer for low frequency jitter transmitter design.

9.3 Tag Battery Life

While the POC prototype tag is powered via the MPU, the target design will be battery powered. Tests were conducted to characterize a small form factor 450 maH LiPo battery while powering the IMU and a low power transmitter. Approximately 6.5 hours of battery life was obtained. Results of the battery life test are shown in Figure 17. Battery life.

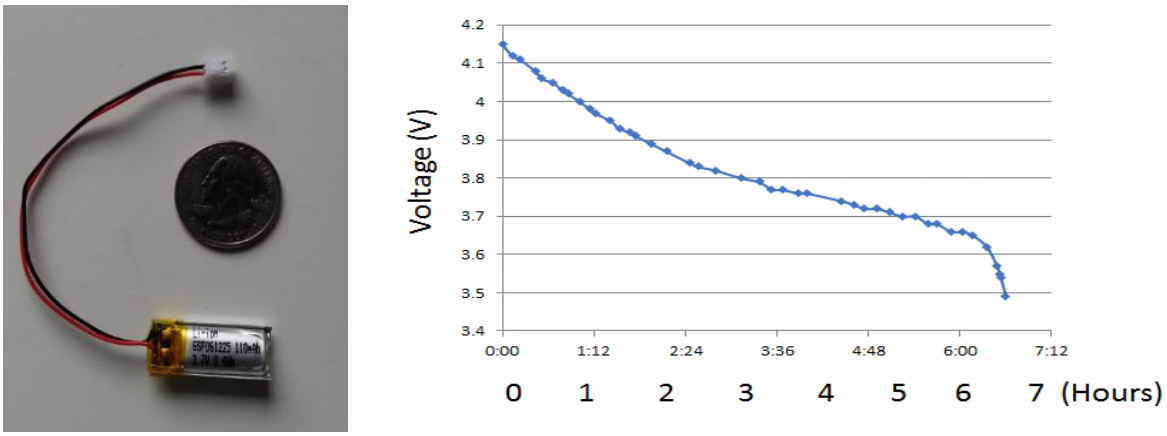

Figure 17. Battery life.
(a) 0.4WH Li Ion battery (b) Battery discharge curve vs. time (h:mm) while powering the COTS NRF24L01 transceiver module and 9DOF IMU.

9.4 Tag and Array Location Simulation

We simulated the location of the tags with respect to the Field of View (FOV) of the receiver array to determine the angular variation of the tags while the arms and legs are in motion. Figures 18 and 19 illustrate the tag positions over a 1 second interval while walking. The simulation shows when the tags are within the FOV and hence when the RF position estimates can be used for tracking and providing position updates to the IMU. While the tags are shadowed, the sensor fusion algorithm relies on the IMU inputs, thus providing full temporal position estimates. The percentage of time that the tags are in the RF FOV will increase for activities when the arms are in front of the body.

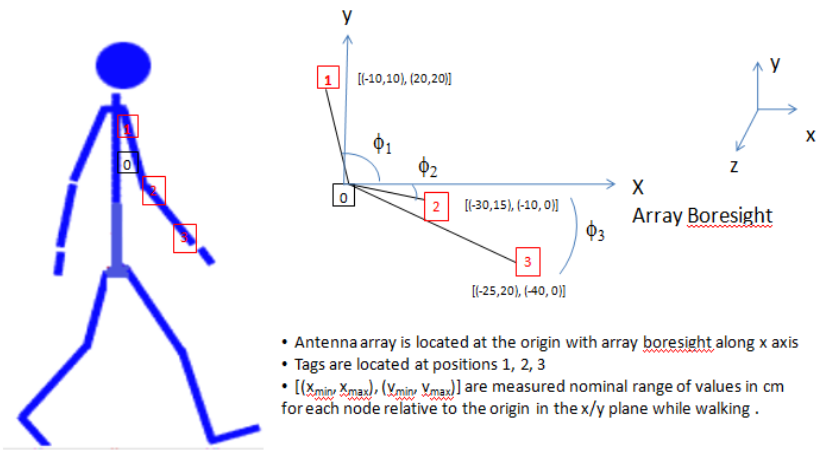

Figure 18. Arm geometry.

Geometry used in the simulation to determine angular variation of the tags while walking.

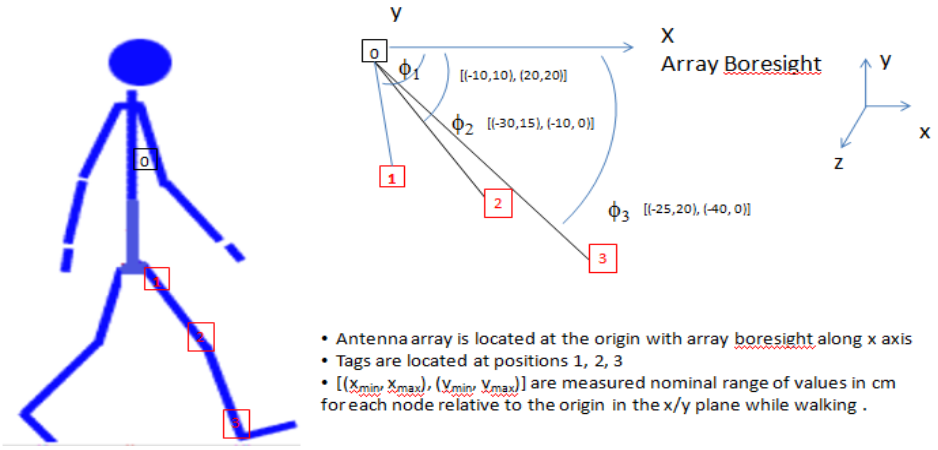

Figure 19. Leg geometry.

Geometry used in the simulation to determine angular variation of the tags attached to the leg while walking.

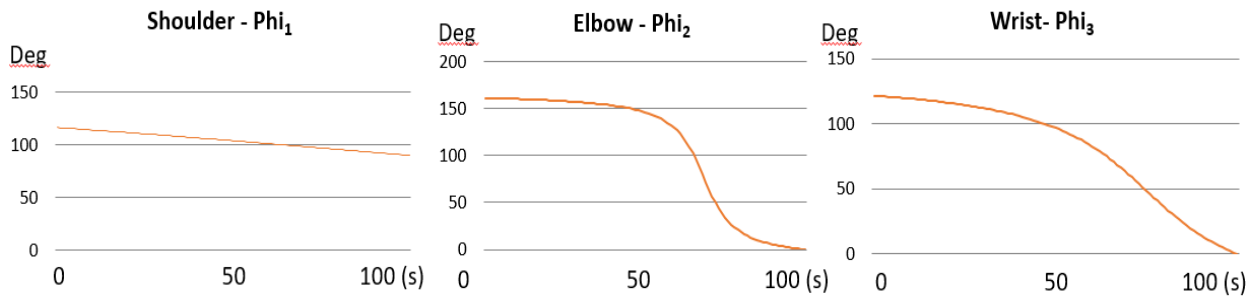

Figure 20. Arm angular range.
Shoulder, elbow and wrist angular position with respect to the receiver array antenna for the geometry as defined in Figure 18 over a 1 second interval while walking.

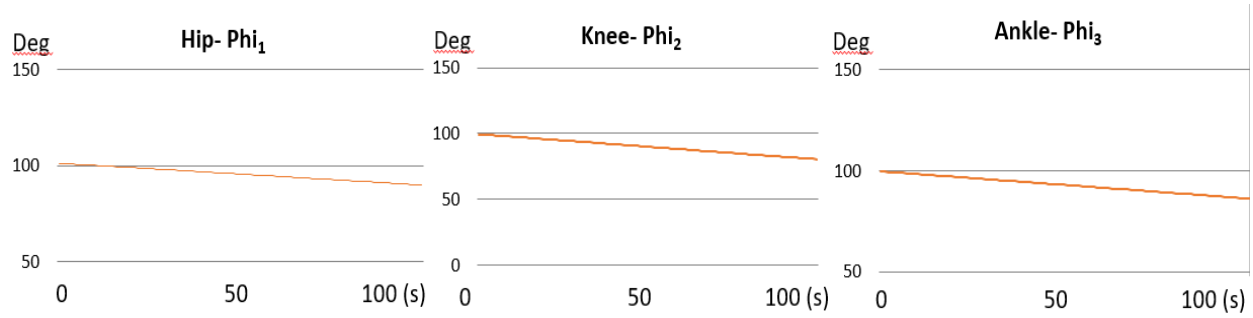

Figure 21. Leg angular range.
Hip, knee and ankle angular position with respect to the receiver array antenna for the geometry as defined in Figure 19 over a 1 second interval while walking.

10.0 GUI Design

A graphical user interface (GUI) has been developed to physically visualize the output of the sensor array. The initial GUI was developed in the *Processing* programming environment to facilitate easy communication between the MPU and the PC running the software.

The GUI currently can run on any device running Windows or Linux operating systems. It communicates using the TCP/IP protocol to gather data that has been processed in the MPU. This allows the data to be securely transferred wirelessly (via point-to-point WiFi) or wired (via Local Area Network). The transferred data includes the 3 dimensional position, velocity, acceleration, segment angle, and torque for each sensor. The data is displayed graphically by the GUI allowing the user to visualize it in real time.

The main display window is a 3 dimensional window that shows the location of each tag. A camera position slider can be found here to adjust the angle that the window is viewed from, thus allowing all tags to be viewed.

Since the 3D display is only useful for visualizing the approximate position of each tag, a secondary display allows viewing a 2D graph of the data streams. A dropdown menu allows the user to select which tag they would like to visualize and then choose the type of graphs they would like to display (position, velocity, acceleration, torque, or angle each plotted against time). Whether or not the data is displayed, all values are written to a text file along with a timestamp for post processing analysis.

Sequential screenshots of the GUI displaying an arm performing a curling action are shown in Figure 22 below.

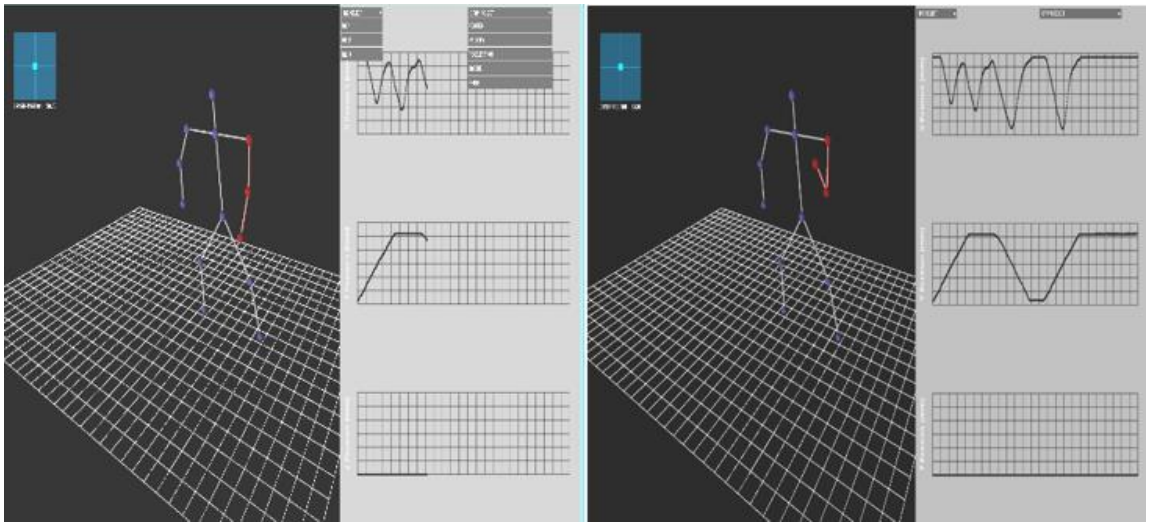

Figure 22. GUI.
GUI screenshots depicting robotic arm motion. A dropdown menu allows the user to select an individual tag and view the acceleration, velocity, position, segment angle and torque for each tag in the graph panel.

11.0 System Performance

The system position accuracy performance is summarized in the following sections.

11.1 Test Validation Platform

The POC system performance was validated with the system shown in Figure 23. System test setup with spectrum analyzer, control PC, robot arm platform with attached tags and antenna array. Multiple tags are attached to the robot arm (described below) and the tag signals were collected by the antenna array and analyzed with a PC. The relative signal levels were also measured with a spectrum analyzer.

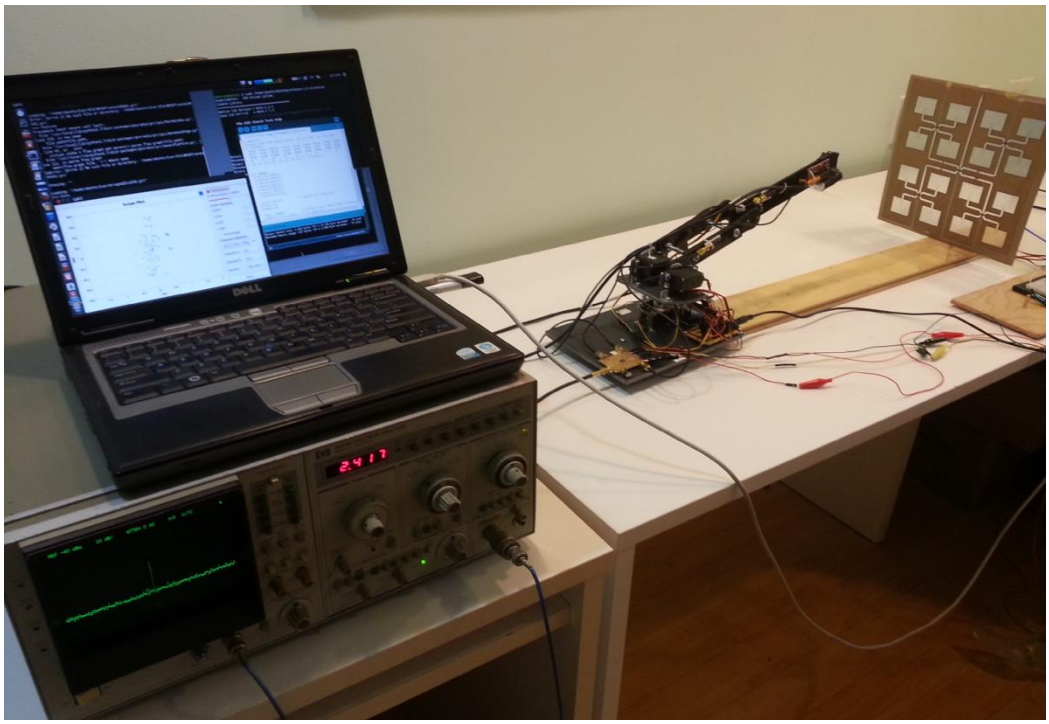

Figure 23. System test setup with spectrum analyzer, control PC, robot arm platform with attached tags and antenna array.

11.2 Robot Arm

As discussed earlier, we designed and constructed a 3 Degree of Freedom (DOF) robotic arm with positional feedback to assess the RF positioning accuracy. The arm has been designed to closely mimic the abilities (position, velocity, and acceleration) that a human arm may move in under typical scenarios. The arm is controlled by a number of high precision servo motors that have been modified to provide angular

feedback. The arm segments were cut using a CNC router and were constructed from PVC sheets which have a high modulus of elasticity while still maintaining a low density which will allow for rigid and precise movements.

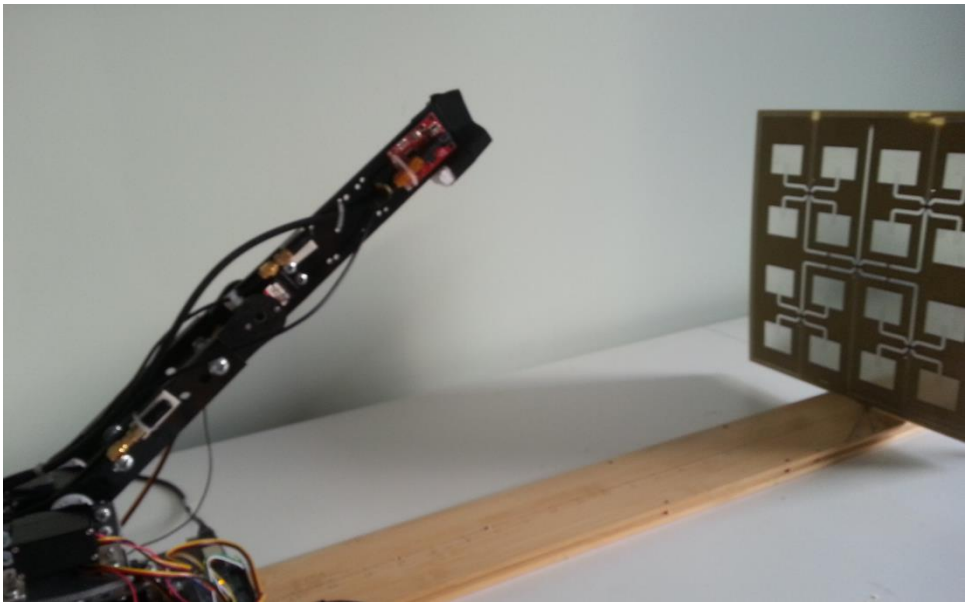

Figure 24. 3D arm motion test platform.

Multiple tags were mounted to the arm to verify segment position, velocity and acceleration tracking accuracy as well as the determination of adjacent segment angles as the arm moves in three dimensions. Using inverse kinematics, a position can be sent to the robotic arm and an on board microcontroller can control the various servos to move the tag to the specified position. This position can then be compared with the position reported by the tag and any discrepancies will then become apparent. The inverse kinematic equations have been solved for the arm and were applied to determine the platform dynamics (see equations below).

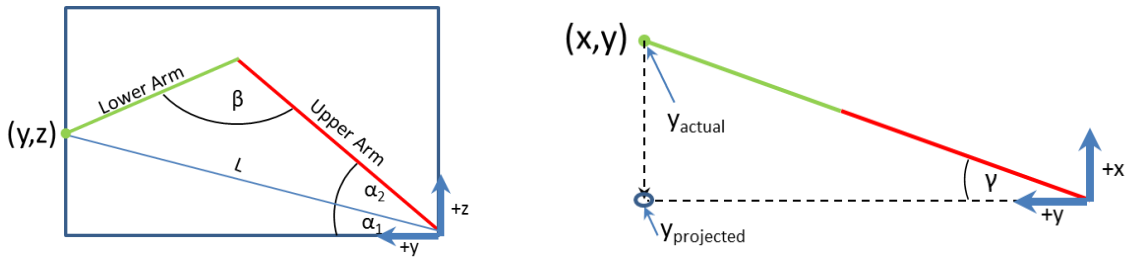

(a) (b)

Figure 25: (a) Side View of 3 DOF Arm (b) Top View of 3 DOF Arm

$$\frac{x}{y} = \tan(\gamma)$$

$$\rightarrow \gamma = \tan^{-1}\left(\frac{x}{y}\right) \quad (10)$$

$$y_{projected} = y_{actual} * \cos(gamma)$$

$$L = \sqrt[2]{y_{projected}^2 + z^2}$$

$$\alpha_1 = \cos^{-1}(\frac{z}{L})$$

$$Lower\ Arm^2 = Upper\ Arm^2 + L^2 - 2(Upper\ Arm)(L)\cos(\alpha_2)$$

$$\rightarrow \alpha_2 = \cos^{-1}\frac{Lower\ Arm^2 - Upper\ Arm^2 - L^2}{-2(Upper\ Arm)(L)}$$

$$\alpha = \alpha_1 + \alpha_2$$

$$\alpha = \cos^{-1}(\frac{z}{L}) + \cos^{-1}\frac{Lower\ Arm^2 - Upper\ Arm^2 - L^2}{-2(Upper\ Arm)(L)} \quad (11)$$

$$L^2 = Lower\ Arm^2 + Upper\ Arm^2 - 2(Lower\ Arm)(Upper\ Arm)\cos(\beta)$$

$$\rightarrow \beta = \cos^{-1}\frac{L^2 - Lower\ Arm^2 - Upper\ Arm^2}{-2(Lower\ Arm)(Upper\ Arm)} \quad (12)$$

11.3 Motion Capture Test Results

11.3.1 IMU Measurements

A graph comparing the IMU position versus the robot arm reference position for the elevation plane as a function of time is shown in Figure 27. Position derived from RF phase (Phase) compared with robot arm position (using inverse kinematics) showing less than 0.5mm error in the vertical plane. Note that what appears to be quantization noise on the robot reference trace, Robot Ref EL, (jitter on the rising/falling slopes while the robot arm is in motion) is due to the robot arm servos internal control loop that uses a Pulse Width Modulation (PWM) control pulse to drive the servo. This creates the jitter pattern on the black trace in Figure 26.

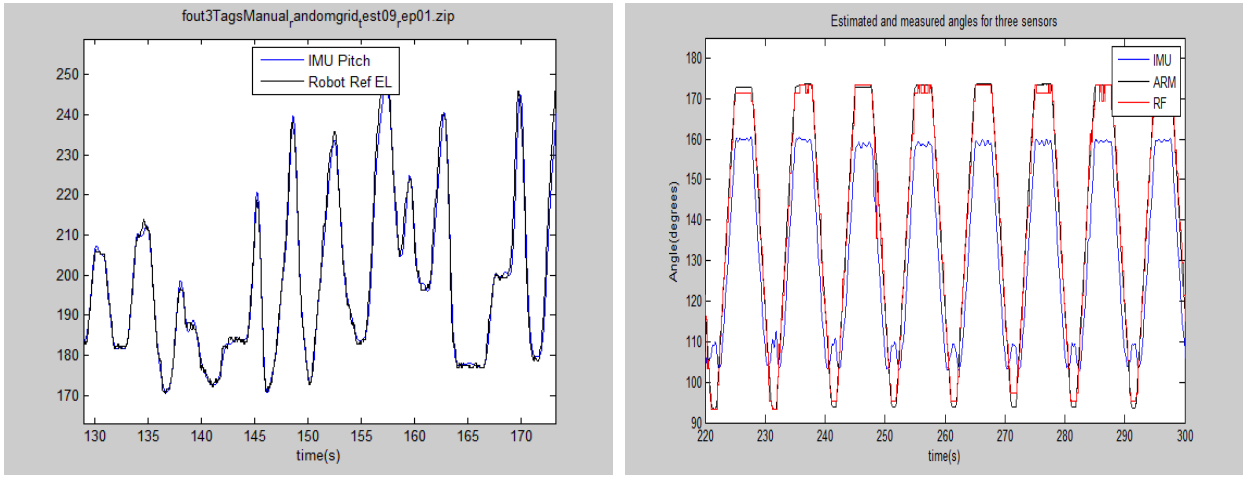

(a) (b)

Figure 26. IMU pitch angle and error.
Elevation plane measured position from IMU sensor (IMU Pitch) compared with robot arm reference position (Robot Ref EL) as a function of time (a) for the IMU mounted at the robot shoulder (b) for the IMU mounted at the robot wrist with a 30 deg fixed shoulder pitch angle, where the elevation response was limited at the peaks due to the additional shoulder pitch angle. (Note: the left graph vertical axis is the elevation angle and the right graph vertical axis is the segment angle as defined in Figure 15).

While conducting additional tests, we found that the COTS IMU accuracy did not always track the reference position at the low and high pitch angles, particularly for the wrist IMU which had an additional fixed pitch angle contribution of 30 degrees from the shoulder. Sensor fusion using the RF position sensor overrides this IMU error.

11.3.2 RF Phase Measurements

The RF phase based position measurement was also compared with the robot arm reported position in Figure 27. Position derived from RF phase (Phase) compared with robot arm position (using inverse kinematics) showing less than 0.5mm error in the vertical plane. Note that the difference in the robot position versus the position derived from the RF phase is less than 0.5mm during the measurement interval.

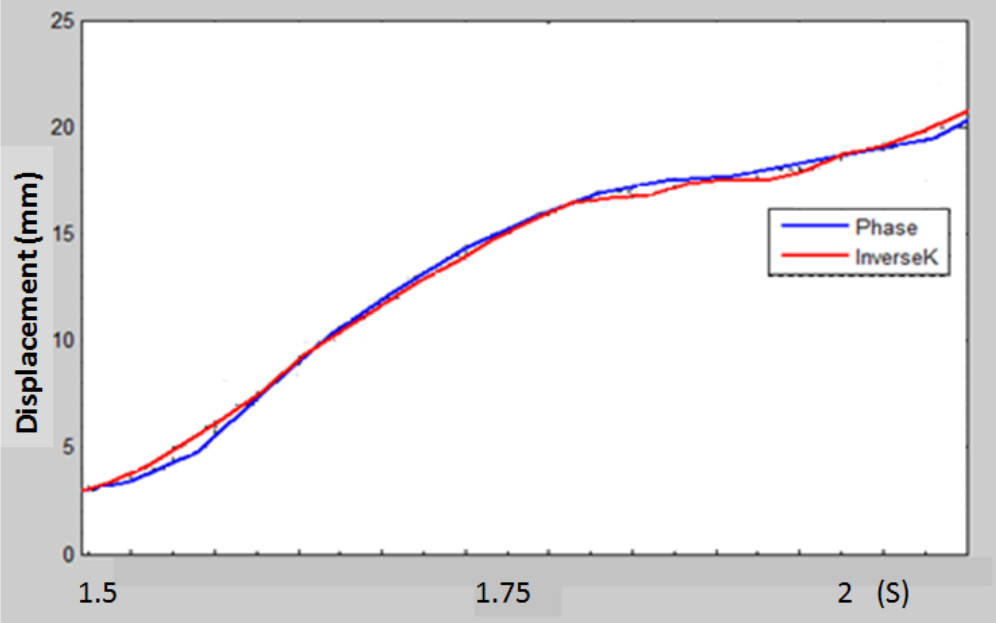

Figure 27. Position derived from RF phase (Phase) compared with robot arm position (using inverse kinematics) showing less than 0.5mm error in the vertical plane.

11.3.3 RFDOA Measurements

The RFDOA and phase modulation (PM) derived positions are shown in Figure 28 below. The scatter plot is created by plotting the robot position (red circles) from an initial calibration sweep of the robot arm. During this initial calibration sweep, the RF

phase and amplitude response is measured to create a position estimate based on the Maximum Likelihood estimator as described earlier.

During a subsequent sweep representing the test measurement, the tag RF position estimates (blue circles) are determined from the Maximum Likelihood signal processing algorithm.

In the ideal case, the red and blue dots would overlay exactly if the Maximum Likelihood estimator was perfect. A higher resolution search space for the Maximum Likelihood estimator can mitigate these measurement errors by creating a search space with more entries thus reducing the nearest neighbor mapping distance when assigning a position estimate.

The servo motor noise described earlier may also be a contributing factor to the measured position standard deviation resulting in some of the observed outliers. We can address this by increasing the sweep velocity which will reduce the servo jitter.

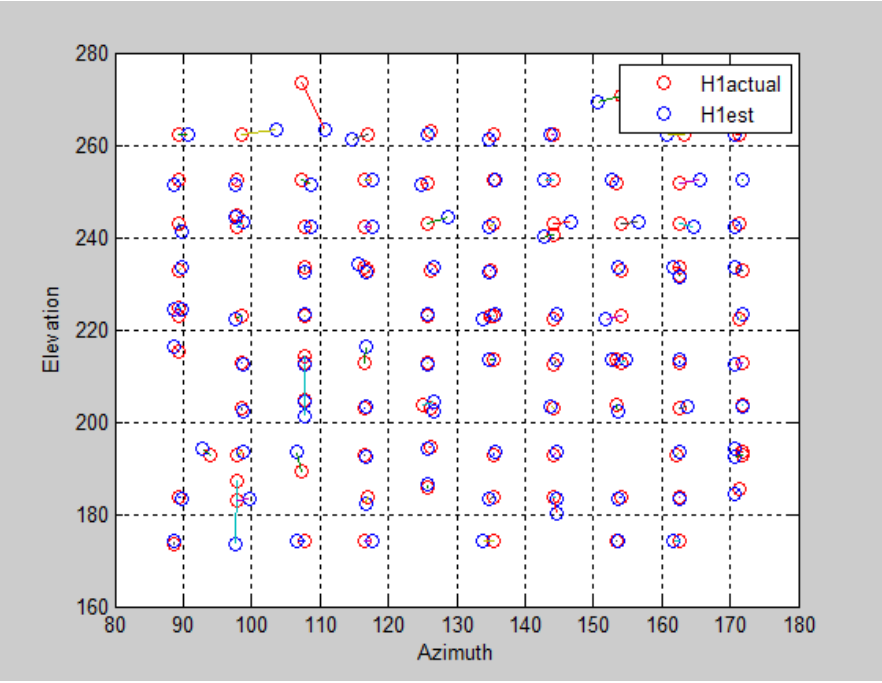

Figure 28. RF position estimates versus robot arm reference positions for azimuth and elevation (in degrees).

12.0 Future Work for the Wearable Sensor System for Body Motion Capture

The wearable motion capture system just described enables the use of a handheld radar sensor to measure physiological vital signs motions. By measuring the user's arm motion holding the radar sensor and applying the motion capture data to a motion compensation algorithm, the target respiration motion can be isolated.

Motion capture with a RF sensor that detects the position of a RF tag was shown to be feasible with a proof-of-concept prototype. The measured position accuracy was 0.1 degrees with 1.3 degrees standard deviation. Using sensor fusion, the RFDOA sensor can improve the position accuracy of the system over an IMU sensor alone, thus improving the accuracy of the motion compensation algorithm. Details of such a motion compensation algorithm are described next.

The wearable sensor system for capturing kinematic body motion was patented and licensed to a 3rd party in 2016. Work has commenced on developing a portable version where the electronics will be contained in a back pack for demonstration purposes. A higher frequency sensor is required for smaller form factors and additional signal processing algorithm development is required to eliminate the need for system calibration.

13.0 Background and Motivation for Motion Compensation

Motion compensation for radar sensors is required if the sensor is on a mobile platform such as a vehicle or if the radar sensor is mounted in a handheld device. There are many applications including military, security and first responder scenarios where it would be useful to detect the presence of a hidden adversary behind a wall or a victim buried under debris with a remote radar sensor. Unmanned Aerial Vehicles (UAVs) have the potential for post-disaster search and rescue missions where triage can be conducted on victims using an on-board radar sensor to detect respiratory motion [6]. However, such a system requires platform stabilization and a motion compensation algorithm so that physiological motion signals such as respiration and heart rates can be extracted. The motion capture methods described earlier can be used to measure platform motion and enable the isolation of motion signals of interest.

Vital signs measurements using a stationary Continuous Wave (CW) Doppler radar sensor have been previously demonstrated [7] [8]. Since the radar signal corresponds to the phase modulation resulting from the range variation between the radar and the subject, any sensor platform motion will induce an undesired phase component on the respiration signal. Other papers describe motion cancellation techniques for vital signs sensing when the subject's motion interferes with the measurement [9] [10] .

Empirical Mode Decomposition (EMD) uses an iteration of the Intrinsic Mode Function (IMF) to decompose the signal. While promising, the ability to recover a heart rate signal in the presence of a larger amplitude respiration signal is not possible without attenuating the respiration signal [10].

For our scenario, the assumption is that the subject is stationary as is likely the case for a post-disaster scenario where victims are prone on the ground.

Our hypothesis is that the combination of mechanically stabilizing the platform in conjunction with baseband signal processing will improve the Signal to Noise Ratio (SNR) of the target signal and improve the probability of detection. The concept is similar to camera stabilization systems that apply vibration reduction and pixel shifting to de-blur images resulting from camera shake [11].

We first describe the concept of operations (CONOPS) for a UAV post-disaster search platform and the platform stabilization and motion compensation architecture that enable this concept. Experimental results for an ultrasonic sensor and radar sensor that provides error signals for the mechanical platform stabilization are described. A programmable bench top test platform was constructed to simulate the unwanted UAV platform motion. A platform stabilization sub-platform was mounted on the base platform and was programmed to compensate for the base platform motion based on inputs from an ultrasonic sensor or secondary radar sensor that measured the unwanted motion in real-time. The primary radar, a 10GHz radar sensor was mounted on the sub-platform and pointed at a respiration phantom to assess the performance with and without the platform stabilization and/or motion compensation.

In the following sections, we describe the CONOPS, the motion analysis, simulation, experiment configurations, ultrasonic ranging sensor and experimental results.

13.1 CONCEPT OF OPERATIONS

The operational concept is for the system to have a search mode, a platform stabilization mode and signal acquisition mode as shown in Figure 29 and Figure 30. In the search mode, the UAV navigates to the area of interest using GPS waypoint coordinates or could navigate autonomously. An onboard camera with image recognition could be used to identify potential victims (targets) [6]. In the stabilization mode, a suite of sensors, including GPS, IMU, LIDAR and/or ultrasonic range sensors, could be used to adjust the quadcopter’s Electronic Speed Controllers (ESC) to maintain a steady altitude and fixed Yaw, Pitch and Roll (YPR) attitude. In the platform stabilization mode, the UAV hovers above the subject and uses the stabilization techniques described in later sections to improve the target Signal to Noise Ratio (SNR).

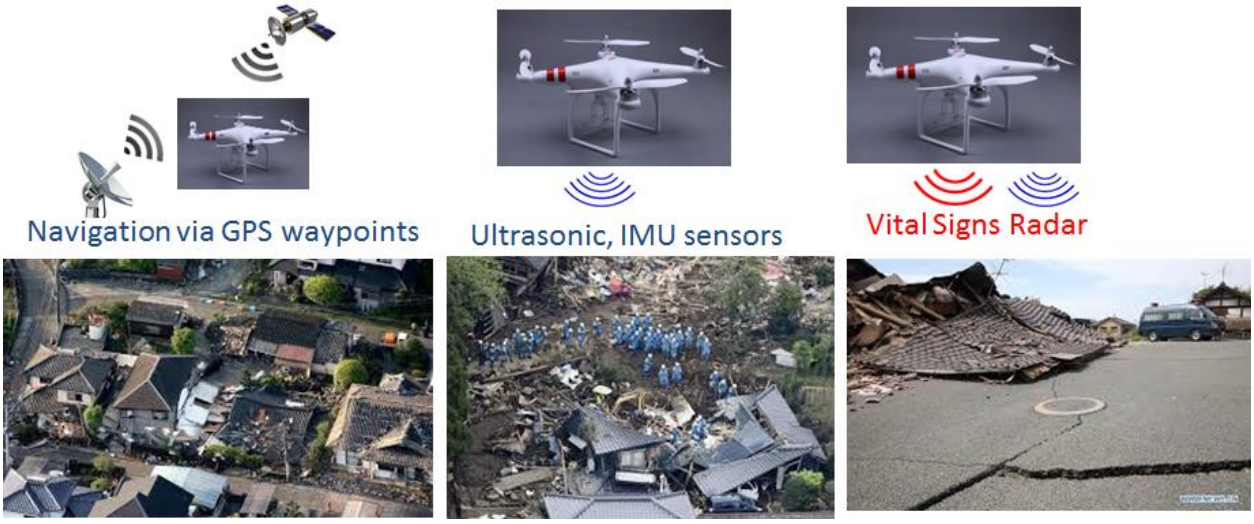

Figure 29. Concept of operations for a UAV search and rescue platform with remote sensing radar.

Figure 30 shows the modes of operation including the search mode, platform stabilization mode and motion compensation signal processing. During the search mode, GPS and waypoints are used to navigate to the general search area. Image recognition can then be used to pinpoint potential targets. Once a target is located, the platform stabilization mode is invoked using altitude and attitude sensors to reduce the in-range motion. Cross-range stabilization is achieved by tracking the RFDOA, RSSI or using image recognition to maintain a hovering position directly above the target. Finally, baseband signal processing extracts the recovered signal using phase motion compensation.

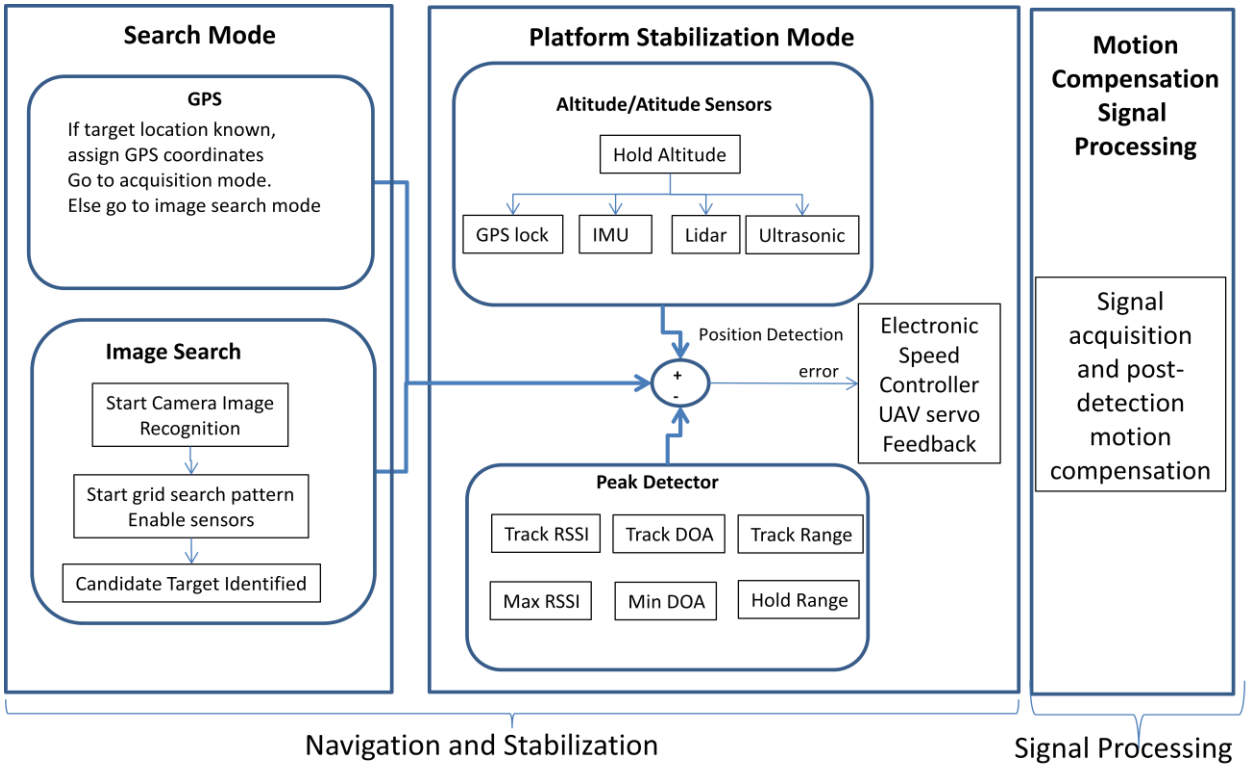

Figure 30. Search and stabilization modes for the UAV radar sensor platform. Conventional sensors (GPS, IMU, barometric sensors) that determine altitude and yaw, pitch, roll (YPR) are supplemented with range sensors (ultrasonic, LIDAR) for motion compensation. The SNR of the on-board vital signs radar sensor pointed downward is improved by the platform stabilization and post detection baseband motion compensation signal processing.

14.0 Position and Motion Sensors Overview

Position sensors measure the absolute position of an object in 3 dimensions (x, y, z) in a fixed frame of reference, e.g., earth coordinates specified in latitude, longitude and altitude. Examples include GPS/Global Navigation Satellite Systems (GNSS) and optical systems that track reflective markers worn on the body.

Range sensors measure the distance to the object of interest, typically by observing the Time of Flight (ToF) and calculating the distance based on the propagation velocity of the reflected signal that was transmitted. By combining multiple range sensors, the object's position can be determined via trilateration.

Technologies for position and range sensors are summarized in Table 8 and described in the next section.

Table 8. Summary of position and range sensors with performance parameters to consider for motion compensation.

Position Measurement						Range Measurement						Lateral Position
	GPS	Cell Network	Camera Tracker	IMU	RF Mapping	Radar Phase	FMCW Radar	FSK Radar	Pulse Radar	Ultra-sonic	Lidar	Image
Measure-ment	Position	Position	Position	Position	Position	Range	Range	Range	Range	Range	Range	Cross-range
Metric	TDOA	TDOA, Cell ID, RF Pattern Matching	Optical Markers	Yaw Pitch Roll Dead Reckon-ing	Phase, amplitude RF map	Doppler phase	Beat freq	Phase offset	Time of Flight	Time of Flight	Time of Flight	Pattern Recog-nition
Absolute Position	Yes	Yes	Yes	Yes	Yes	Range + DOA scan	Range + DOA scan	Range + DOA scan	Range + DOA scan	Range + DOA scan	Range + DOA scan	Lateral Position only
Coverage	Worldwide except Indoors, Urban Canyons	Cell Networks	Camera line-of-sight	Host platform	Pre-calibration volume	Antenna Beamwidth	Antenna Beam width	Antenna Beam width	Antenna Beam width	Trans-ducer Beam width	Laser Beam-width	Sensor FOV
Resolution	GPS: 7m DGPS: 5cm	< 50 m	< 1 mm	< 1 deg 1 deg = 5.6 mm for 319 mm segment	7 cm @ 2.4 GHz, 3 m range	.84 mm @ 10 GHz, 10 deg phase noise	.8m @150M Hz BW	2.7 cm @150 MHz BW	3 cm @ 730 pS pulse	6 mm	1 cm	.36 mm Cross-range @ 3 m range, 1920 pixels
Vital Signs Radar Motion Compen-sation	Insufficient Resolution	Insufficient Resolution	Confined to Fixed external sensors range	Possible	Possible with calibration	Ideal	Insuf-ficient Resolu-tion	Insuf-ficient Resolu-tion	Insuf-ficient Resolu-tion	Mech-anical stabili zation	Mech-anical stabiliz ation	SNR maximiza tion

14.1 Position Measurement Technologies

There are many position sensing technologies available, but not all are suitable for the platform stabilization and motion compensation techniques described in this study. Table 8 summarizes the technologies and categorizes them into 3 dimensional position measurement (x,y,z), ranging measurement (z) and cross-range position measurement (x,y) capabilities. Many papers have been published on the topic of position location [23-27]. A brief summary of the most common position measurement technologies follows.

14.1.1 Global Navigation Satellite Systems (GNSS)/Global Position System (GPS)

GPS navigation is the most commonly used satellite navigation system, however, other satellite based navigation systems have been deployed, including the Russian GLONASS, EU's Galileo and India's IRNSS systems. Other regional systems will be deployed in the near future by China, Japan and France.

GPS satellites were deployed by the US Air Force in the 1980s to provide navigation and positioning for military combat missions before becoming an ubiquitous consumer technology. The GPS constellation comprises 4 satellites in each of 6 orbital planes at 55 degree inclination and 11,000 nautical miles altitude. Precise positioning is derived from measuring the Time Difference of Arrival (TDOA) from a minimum of 4 visible satellites at any location. Precise timing is derived from the on-board cesium clocks in order to accurately measure the TDOA. The P-code and C/A-code modes allow the system to be used for higher accuracy military use and lower accuracy commercial use. Typical errors are around 1 m to 3 m and are due to ionospheric/tropospheric propagation effects, multipath and measurement errors. GPS can be used for waypoint navigation in the proposed system, but the position accuracy is not sufficient for the platform stabilization and motion compensation algorithm.

Real-Time Kinematic (RTK)-GNSS positioning systems with multiple receivers can achieve centimeter level accuracy as described in recent papers presented at the Institute of Navigation GNSS conference [12] [13]. This is sufficient for real time

Simultaneous Location and Mapping (SLAM) applications but not sufficient for the phase motion compensation approach described later.

14.1.2 Cellular Networks

TDOA measurements from a transmitter to multiple base stations can also use trilateration to determine the transmitter location. However, multipath effects can significantly alter the “arrival” measurement at a given base station and reduce the accuracy of the derived range measurement. Network based location servers also supplement cell towers with known WiFi access point locations to increase positioning accuracy.

RF pattern matching (RFPM) techniques have been developed to “fingerprint” the phase and amplitude spatial distribution via city-wide drive tests to account for the multipath effects [14]. Some algorithms rely on RSSI measurements compared with simulated RSSI values to map a receiver’s position [15]. Companies such as US Wireless and Polaris Wireless, who the author previously consulted for, have deployed networks that allow position determination in indoor and GPS denied areas. Overall position accuracy, however, is in the tens of meters for network based RFPM, with improvements to < 3m for dedicated indoor networks [16].

14.1.3 Optical Tracking

Optical tracking is used when sub-millimeter level position measurements are required. The operating principal is based on stereoscopic imaging of reflective markers. These systems are often used for body motion capture in the movie industry. While highly accurate, these systems require fixed infrastructure that limit the range of coverage and the attachment of clusters of body markers using a body suit. Researchers have combined optical tracking with magnetic field trackers and achieved accuracies of 0.2 mm to 0.3 mm [17].

Optical tracking provides extremely precise position measurements, however, would not be practical for deployment on a mobile platform given the need for the fixed location camera infrastructure.

14.1.4 Inertial Measurement Unit (IMU)

IMUs were originally used in aircraft and missile navigation systems. The IMU measures acceleration via an accelerometer, attitude with respect to the earth's magnetic field using a magnetometer and relative rotation with a gyroscope. By measuring the overall spatial orientation (yaw, pitch and roll) combined with the direction vector, dead reckoning navigation can be used to determine the IMU position over time. Position can also be derived by double integrating the acceleration component, however, errors rapidly accumulate due to the integration constant and drift. As a result, position measurements using an IMU require sensor fusion, usually with an Extended Kalman Filter (EKF), of the accelerometer, magnetometer and gyroscope.

Recent advances in MEMS technology have introduced single chip IMUs that are ideal for small form factor devices and mobile platforms. Overall position measurement accuracy is typically 5% of the distance traveled [3] . Given this, an IMU would not be suitable for platform stabilization and motion compensation.

14.1.5 RF Mapping

RF mapping of the spatial distribution of the amplitude and phase of the tracked signal is described in Part I of this dissertation. RF mapping capitalizes on the unique spatial distribution of amplitude and phase signatures. This mapping contains a one-to-one correspondence that allows the position of a RF emitter to be determined. Position accuracies of a few millimeters have been measured for a receiver array at a fixed location that measured the variable position of an emitter. Note that this technique requires pre-calibration and thus would not be practical on a mobile platform in a dense multipath environment.

14.2 Range Measurement Technologies

The previous section described absolute position measurement technologies. Since relative range measurements are sufficient for phase compensation, in this section we review range measurement techniques that can be applied to motion compensation algorithms. Range measurement techniques can be categorized as: (1) Time of Flight

(ToF), (2) Indirect ToF (3) Time Difference of Arrival (TDOA) and (4) Phase Difference of Arrival (PDOA). See Table 8. A summary of range measurement techniques follows.

14.2.1 Continuous Wave (CW) Doppler Radar Phase

Doppler radar operates on the principle of capturing the target motion by measuring the phase of the reflected signal. The Doppler shift and range to target are described by

$$\Delta f = \frac{2\,f\,v(t)}{c} = \frac{2\,v(t)}{\lambda} \quad \text{and} \quad R = \frac{c\,T}{2} \tag{13}$$

where Δf is the receiver frequency shift, f is the transmitter frequency, v(t) is the target velocity, c is the speed of light, λ is the RF wavelength, R is the range and T is the measured transit time between transmission and reception.

The radar transmits the waveform

$$T(t) = \cos[2\pi f_t\, t + \phi(t)] \tag{14}$$

and the received waveform is

$$R(t) = \cos[2\pi f_t\, t + \theta + p(t) + \phi(t - 2R/c)] \tag{15}$$

where f_t is the transmitter frequency, $\phi(t)$ is the transmitter phase offset, θ is the receiver phase offset, p(t) is the phase modulation from the target motion and $\phi(t - 2R/c)$ is the phase delay due to the roundtrip signal propagation.

Continuous Wave (CW) Doppler radar phase measurements are as precise as the ability to resolve the phase angle of the reflected baseband signal. The phase resolution measurement is limited by the Signal to Noise Ratio (SNR) determined by the reflected signal power, background clutter and the phase noise of the local oscillator. As an example, if the phase measurement resolution is 5 degrees for a 24 GHz radar, the position measurement accuracy is limited to 0.17 mm.

A CW Doppler radar suffers from range ambiguity because the baseband signal is a continuous reflection of the transmitted signal that carries no range information. Various techniques, discussed next, have been devised to deal with the range ambiguity. A 10

GHz radar module and 24 GHz radar module used for this investigation is shown in Figure 31 and Figure 32. For the phase compensation algorithm used in this study, the relative phase change due to platform motion is all that is necessary, so the phase ambiguity is not an issue.

Figure 31. Microwave Solutions MDU 1020 10 GHz radar module.

Features

- 24 GHz short range monopulse transceiver
- Dual receiver +/- 15° angle coverage
- Beam aperture 30°/ 12° @ -3dB
- 180MHz sweep FM input
- High sensitivity, integrated RF/IF amplifier
- Buffered I/Q IF outputs for both channels
- Temperature compensated oscillator
- RSW Rapid Sleep Wakeup for power saving
- Extremely compact: 78x98x7mm^3 construction

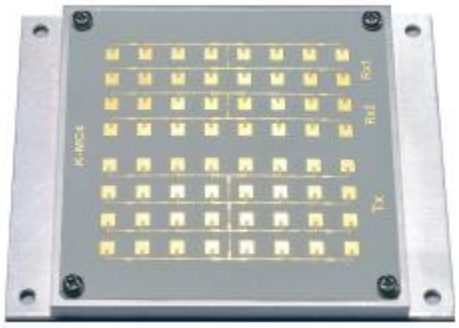

Figure 32. RFBeam Microwave K-MC4 24 Ghz radar module.

14.2.2 Frequency Modulated Continuous Wave (FMCW) Radar

Frequency Modulated Continuous Wave (FMCW) provides unambiguous range measurements by using a swept frequency for the transceiver LO. This swept frequency is referred to a chirp signal. The transmitted waveform at a given time t_1 transmits a waveform at LO frequency f_1. When the reflected signal is received at t_2, the LO frequency is at f_2. The resulting receiver beat frequency $f_B = f_2 - f_1$ corresponds to the time delay, Δt, between the transmission and reception and allows the range to be determined using the following equations.

The delay τ is equal to the round-trip transit time:

$$T = 2R/c \tag{16}$$

where R is the target range and c is the free-space speed of light. The beat frequency generated by mixing the received signal with the LO is:

$$f_B = B_s/T_s * T \tag{17}$$

where B_s is the total frequency deviation of the chirp signal and Ts is the period of the chirp signal. The ratio B_s/T_s is equivalent to the slope of the swept LO. See Figure 33. FMCW chirp waveform and range determination.The target range is thus found from the following equation:

$$R = c\, f_B\, T_s / B_s \tag{18}$$

The issue with FMCW is the range resolution is limited by the receiver bandwidth. For the following parameters which are representative for the RFBeam Microwave K-MC4 radar module:

$$f_B = 450 \text{ Hz},\ T_s = 14 \text{ mS},\ B_s = 160 \text{ MHz},$$

the range resolution is 0.8 m. This is not sufficient for phase motion compensation.

If the target is moving, then the Doppler shift can be measured and provide the range and velocity per the following equations:

$$R = \frac{c\, T_s}{4\, B_s} (f_{bd} + f_{bu}) \tag{19}$$

$$V_r = \lambda_0 (f_{bd} - f_{bu})/4 \tag{20}$$

where f_{bd} is the Doppler shift during the down ramp interval and f_{bu} is the Doppler shift during the up ramp interval. Refer to Figure 33.

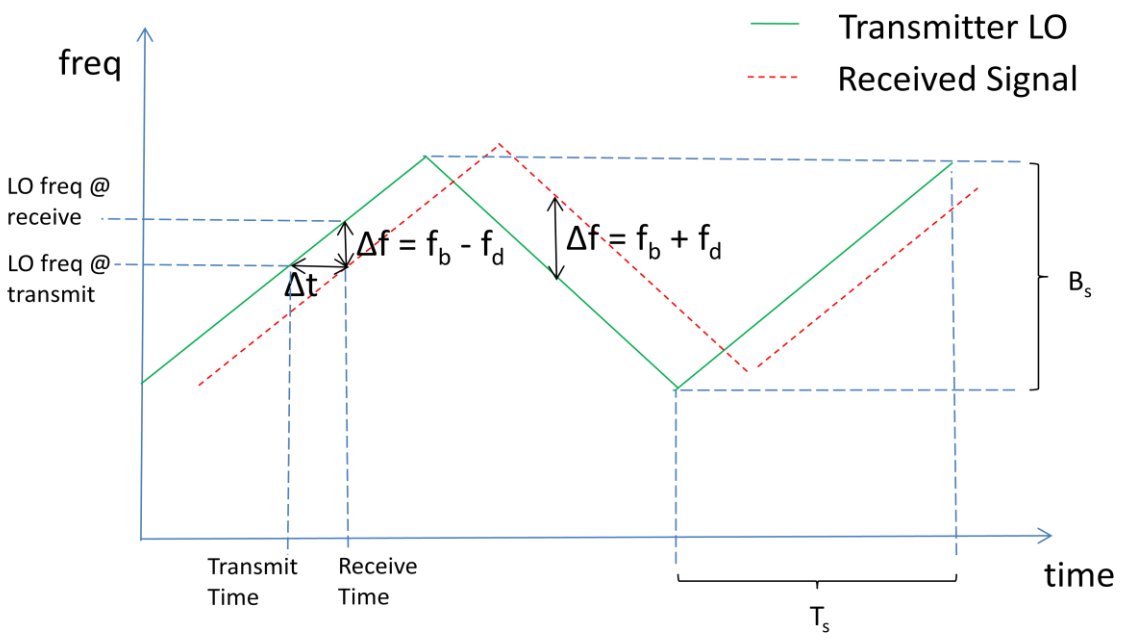

Figure 33. FMCW chirp waveform and range determination.

14.2.3 Frequency Shift Keyed (FSK) Radar

Frequency Shift Keyed Doppler radar is similar to FMCW except that two frequencies, f_a and f_b are used instead of a swept LO as shown in Figure 34. The range is determined by the phase difference of the received signals and the FSK frequencies:

$$R = \frac{\mathbf{c}\,\Delta\boldsymbol{\phi}}{\mathbf{4}\,\boldsymbol{\pi}(\mathbf{fa}-\mathbf{fb})} \qquad (21)$$

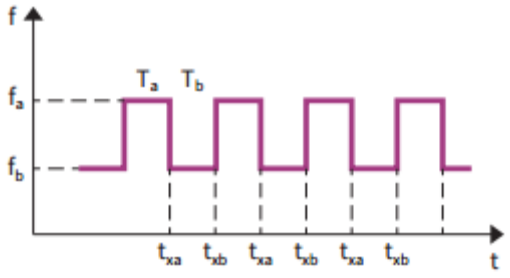

Figure 34. FSK radar transmitter two tone frequency modulation.

14.2.4 Pulse Doppler Radar

Pulse Doppler Radar uses the Pulse Repetition Interval (PRI), Δt, between a transmitted and received pulse to determine the target velocity [17].

$$S = A \sin\left[\frac{4\pi(x_o + v\Delta t}{\lambda}\right] = A \sin(\theta + \Delta\emptyset) \tag{22}$$

$$x_o = \text{range to target}$$

$$\lambda = \text{radar wavelength}$$

$$\Delta t = \text{pulse repetition interval}$$

From the second term,

$$\Delta\emptyset = \frac{4\pi(x_o + v\Delta t)}{\lambda} \tag{23}$$

The target velocity is thus

$$v = -\frac{\Delta\emptyset\,\lambda}{4\pi\Delta t} \tag{24}$$

As with any pulsed radar system, the Time of Flight is used to determine range. At short ranges, this is problematic, as a large bandwidth is required to resolve the time of arrival of the return pulse.

14.2.5 Frequency Multiplier Tags

Several papers that describe the use of passive tags that generate harmonics of the incident radar frequency that allow the isolation of a stationary reference have been published [18] [19]. With this approach, the sensor motion can be extracted from the composite signal containing the desired signal by removing the range as measured by the tag's harmonic frequency.

For a vital signs radar using a frequency multiplier tag, the desired respiration signal was recovered to within a few mm of displacement as measured by a reference piezoelectric chest strap compared with an adaptively filtered 2.4 GHz Doppler radar [19].

This technique has the required accuracy for use in phase compensation algorithms, however, the requirement to place the reference tag in close proximity to the target increases the operational complexity.

The use of RFID tags for position location has been the subject of research in academia and industry because of the relevance for manufacturing and inventory tracking and is well documented in the literature [28-44].

14.2.6 Lidar Ranging

Lidar ranging was also considered for this investigation. The COTS lidar module shown in Figure 35 has a range accuracy specification of 1 cm. Figure 36 illustrates that the range resolution is determined by the lidar pulse width, τ_L, for a system that is not sample rate limited. The lidar range resolution is

$$\Delta R = c\,\tau_L/2. \tag{25}$$

The performance as a mechanical compensation and motion compensation sensor would be subpar to that of the radar sensor. Given this limitation and hardware issues with the COTS lidar module we chose not to evaluate the lidar sensor option.

Figure 35. COTS LIDAR-Lite module.

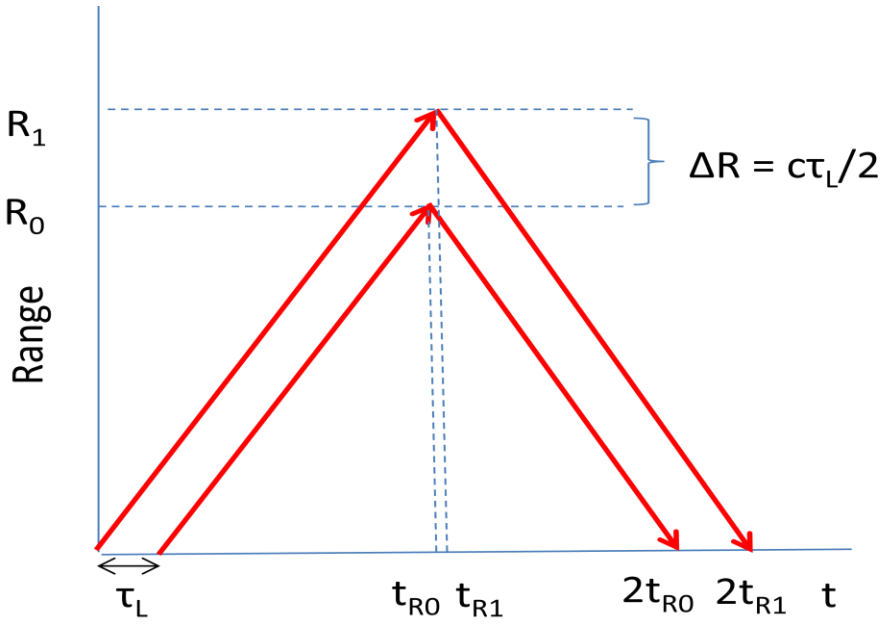

Figure 36. Lidar resolution.

The laser pulse width determines the range resolution for sample rates where $f_s < 1/\tau_L$

14.2.7 Ultrasonic Ranging

Ultrasonic sensors are used in many applications, including as a range sensor in autonomous vehicles. These sensors have the advantage of a low propagation velocity (340 m/s for sound versus 3x10^8 m/s for RF signals) allowing time of flight measurements at short ranges.

The principle of operation is based on measuring the round trip propagation time from the transducer to the object of interest using an acoustic signal in the 40 KHz range. The transducer aperture determines the beam width of the acoustic beam.

COTS ultrasonic sensors are available for less than $5, have low size, weight and power (SWaP) requirements and thus are ideal for mobile platforms. Their downside is susceptibility to acoustic and electrical noise that can contribute as much as 1 cm of error. This can be mitigated by using a moving average filter. We measured the range to a target mounted on a linear actuator that was programmed to move with a sinusoidal

motion. The temporal waveform and spectrum for the ultrasonic sensor measuring a 0.5 Hz sinusoidal signal is shown in Figure 37.

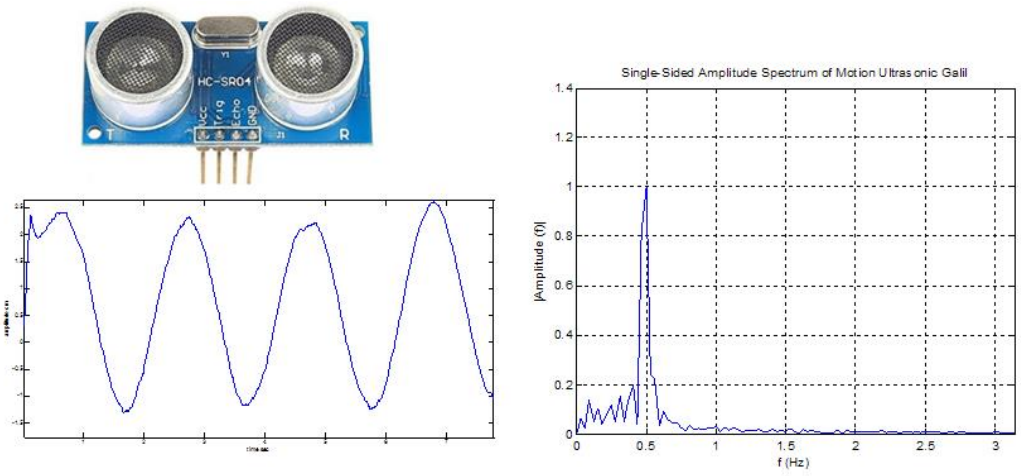

Figure 37. HC-SR04 Ultrasonic sensor module and range measurement performance.

14.2.8 Image Pattern Recognition Navigation

The discussion to this point has focused on in-range motion stabilization and compensation. An additional requirement is to stabilize the cross-range motion of the radar platform. Maintaining cross-range alignment with the target ensures that the SNR is maintained by keeping the target within the radar beamwidth.

Cameras can be used to detect unwanted cross-range (lateral) motion by comparing frame-to-frame scene registration. A pattern recognition algorithm can then determine the pixel displacement for a reference object in the imagery. Since the cross-range motion is orthogonal to the in-range vector, the phase of the primary radar is not affected, unless there is a large cross-range displacement that increases the slant range leading to a range dependent phase shift.

Quadcopter navigation using imagery for object position tracking has been demonstrated by researchers at Ritsumeikan University in Japan [19]. A quadcopter was equipped with a camera that was used to detect the position of two light sources

that were alternately illuminated. The results show tracking to within less than 0.1 m. See Figure 38. Quadcopter navigation using image pattern recognition. Quadcopter altitude tracking of vertically displaced light sources. (b) Quadcopter navigation tracking light sources at .8 m and 1.3 m using camera based imagery for altitude navigationAlthough this experiment demonstrated for vertical target tracking, the same principle can be applied for horizontal cross-range tracking, as would be the case for the UAV platform with a downward pointing radar.

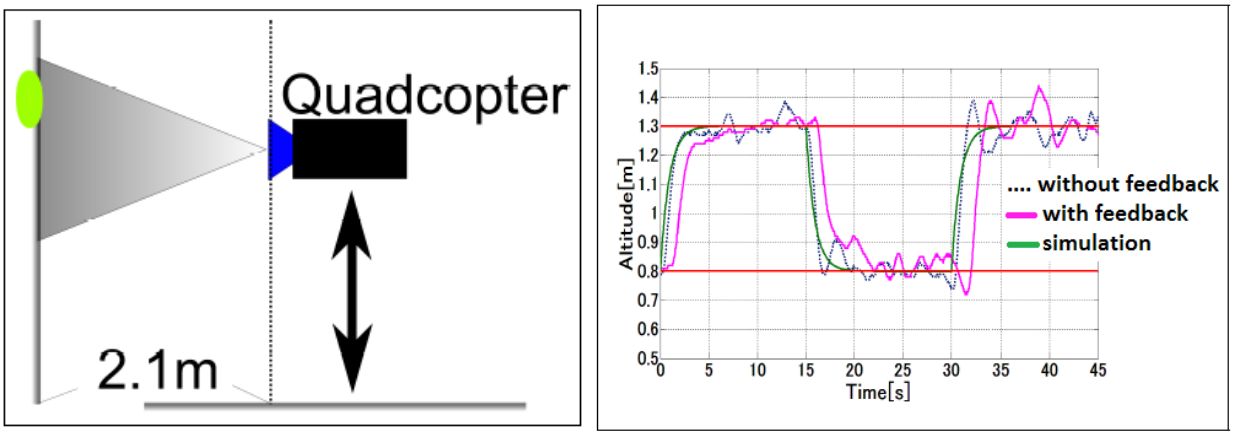

Figure 38. Quadcopter navigation using image pattern recognition.

Quadcopter altitude tracking of vertically displaced light sources. (b) Quadcopter navigation tracking light sources at .8 m and 1.3 m using camera based imagery for altitude navigation [19].

The sensors that were considered and tested for motion compensation are summarized in Figure 39. **Summary of available position and range sensors for motion compensation and platform stabilization.**The sensors are categorized into range sensors for phase motion compensation and for cross-range sensors that could be used to maintain the horizontal position of the platform. For the class of range sensing technologies, radar phase measurements provide the most accurate measurements that correspond to the phase measurement of the baseband radar phase. Many phase ranging techniques are described in the literature [30], [39-41].

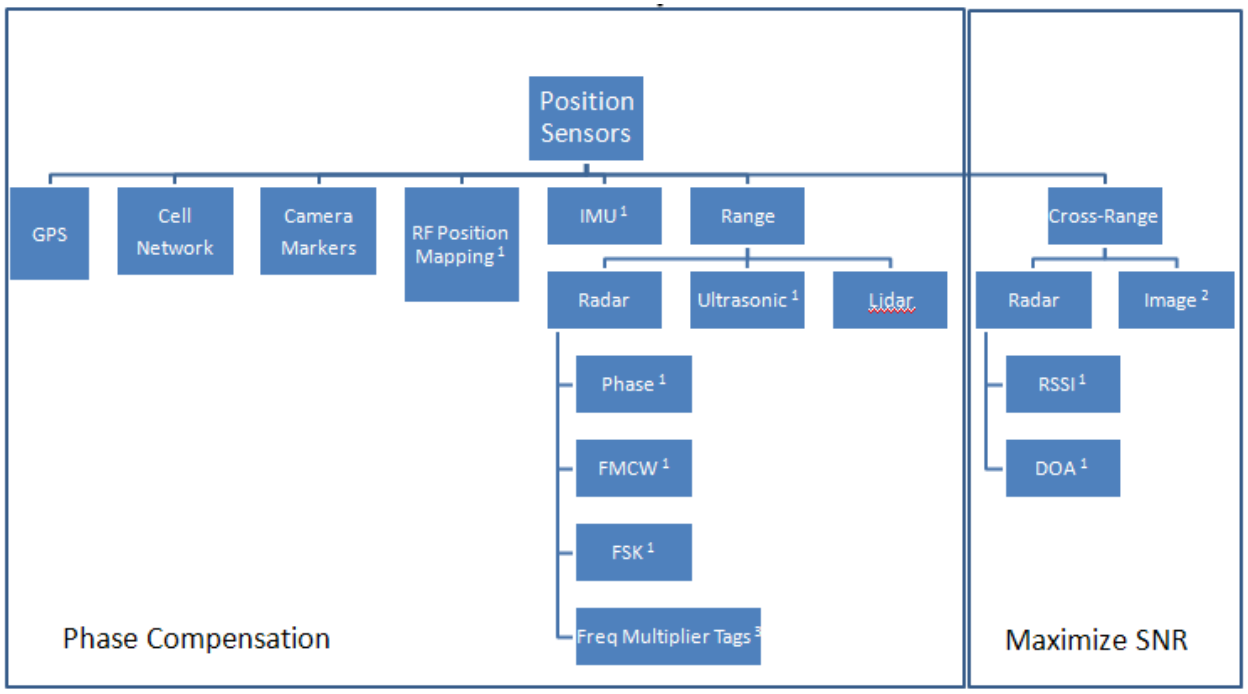

Figure 39. Summary of available position and range sensors for motion compensation and platform stabilization. [1]Tested, [2] [20] , [3] [18].

The pros and cons of each sensor type considered are summarized in Table 5. The performance capability of each sensor type is discussed in the context of sensor fusion in the next section.

Table 9. Sensor pros and cons.

Sensor Type	Pros	Cons
GPS	Commercially available low cost , small form factor, low power receivers	Outdoor coverage only: requires line-of-sight to 4 satellites
IMU	Commercially available low cost , small form factor, low power MEMS devices	Position drift and error accumulation
RF Position Mapping	Accurate position location at short range (7 cm @ 1.3 deg resolution, 3 m range)	Requires calibration and beacon
Radar Phase	Accurate in-range location (.35 mm range resolution, range independent); Commercially available low cost, small form factor, low power devices	Range ambiguity (range not required for phase compensation)
FMCW Radar	Commercially available low cost, small form factor, low power devices	Range resolution limited by receiver IBW
FSK Radar	Commercially available low cost, small form factor, low power devices	Range resolution limited by receiver IBW
Pulse Radar	3cm @ 2.5 GHz, 1 GHz BW, 730 pS pulsewidth, 20 MHz PRF	Requires wideband receiver for TOF measurements
Radar Tag	Provides reference to remove platform motion	Requires second receiver; operational complexity of placing tag adjacent to target
Ultrasonic	Commercially available low cost devices	Range resolution noise
Lidar	Accurate in-range location (.1 cm range resolution, range independent);	Narrow beam width has range errors on uneven terrain

15.0 Sensor Fusion

Sensor fusion is becoming prevalent in many autonomous systems that require control without human intervention. Unlike a single sensor system, the benefit of sensor fusion is that multiple sensor outputs can be combined to improve the overall measurement precision and accuracy leading to increased system reliability and robustness of decision algorithms that use the sensors to adjust the system behavior. See Figure 40 and Table 10. In the case of the wearable sensor described in Part I, the coverage is increased by using an IMU when the RF sensor coverage is occluded.

Many sensor fusion systems apply filtering techniques such as Kalman filters and particle filters to improve the decision outcomes in a noisy environment. These techniques are beyond the scope of this investigation and are not described here as there are numerous references on this topic [21] .

Sensor fusion is a topic of keen research interest with the recent introduction of self-driving vehicles from Tesla, Google, Uber and others [45] – [. Many of the sensors used for self-driving vehicles are applicable for motion capture and motion compensation.

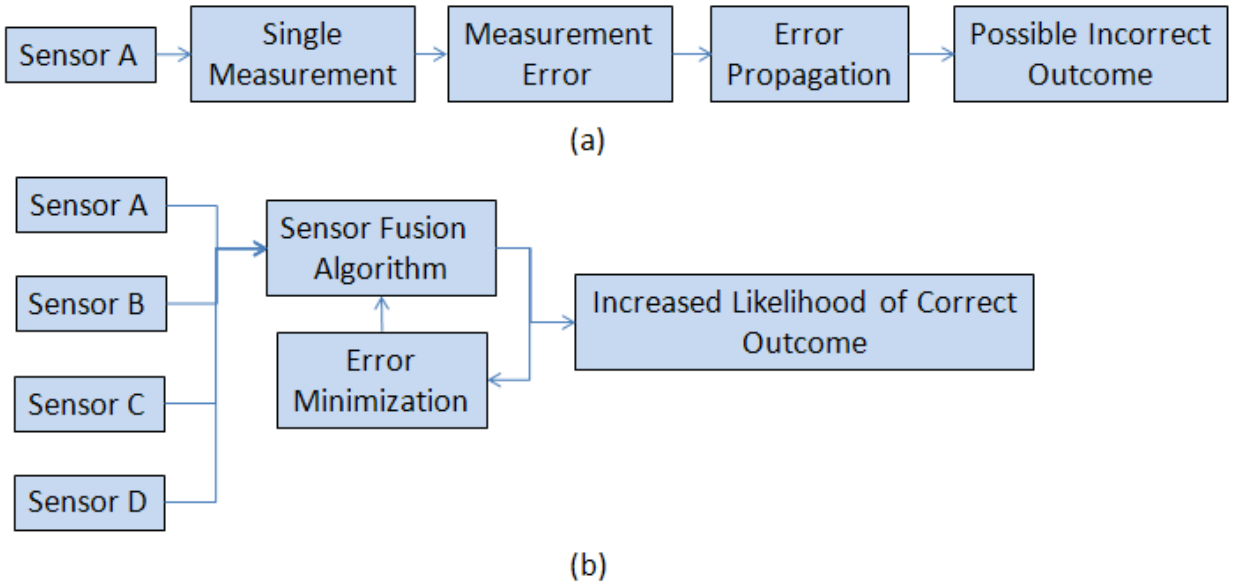

Figure 40. Sensor fusion combines multiple sensors such that the resulting information has less uncertainty than the individual sensor measurements.

Table 10. Sensor fusion performance benefits.

Sensors	Coverage	Precision	Accuracy	Robustness
Single Sensor	Limited	Single Measurement	Single Measurement	Single-Point Failure
Sensor Fusion	Expanded	Multiple Measurement Processing Gain	Multiple Measurement Processing Gain	Fault Tolerant

Considerations for sensor selection are illustrated in Figure 41. Parameters include hardware and algorithm complexity, sensor resolution, coverage, SWaP and cost.

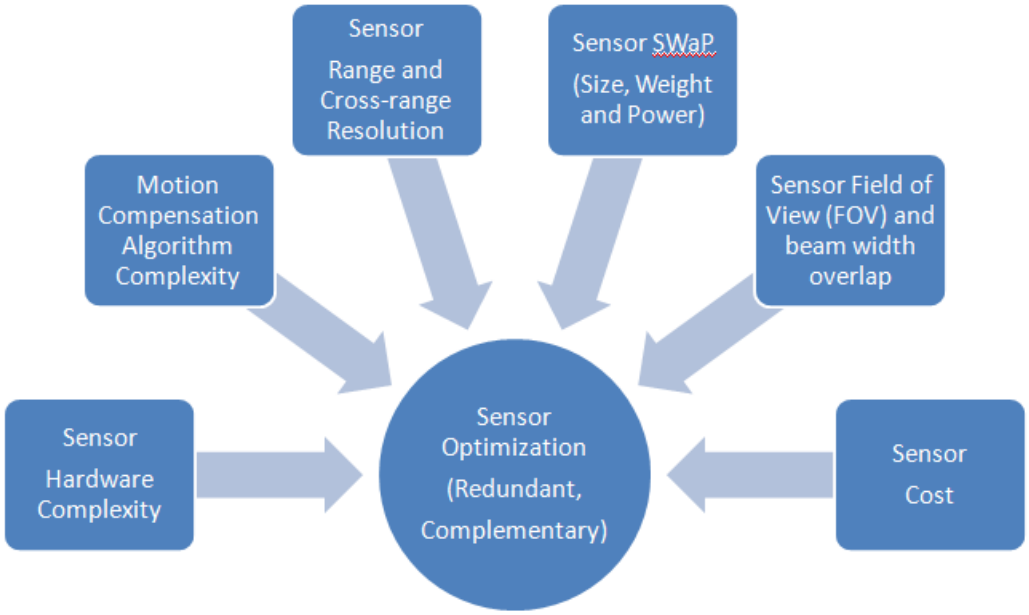

Figure 41. Sensor fusion optimization parameters to consider.

Additional consideration should also be given to redundant and complementary sensors. Redundancy is defined as an additional sensor that doesn't provide precision and accuracy beyond the first sensor. Complementary is defined as an additional sensor that enhances the overall system performance. For example, the wearable sensor RF mapping and IMU sensors are complementary by virtue of the IMU providing coverage when the RF is shadowed and the RF providing position updates for the IMU to minimize IMU drift and errors. Another example of complementary sensors is FMCW and ultrasonic or lidar sensors, since FMCW can't accurately resolve range at short distances, whereas the ultrasonic or lidar sensor is capable of ranging at short distances. See Table 11. Complementary and redundant sensors for motion compensation.

Table 11. Complementary and redundant sensors for motion compensation.

Sensor Type	GPS	IMU	RF Position Mapping	Radar Phase	FMCW Radar	FSK Radar	Radar Tag	Ultrasonic	Lidar
GPS	-	Comp	Comp	Comp	Comp	Comp	Comp	Comp	Comp
IMU		-	Comp	Comp	Comp	Comp	Comp	Comp	Comp
RF Position Mapping			-	Redundant	Redundant	Redundant	Comp	Comp	Comp
Radar Phase				-	Redundant	Redundant	Comp	Comp	Comp
FMCW Radar					-	Redundant	Comp	Comp	Comp
FSK Radar						-	Comp	Comp	Comp
Radar Tag							-	Redundant	Redundant
Ultrasonic								-	Redundant
Lidar									-

15.1 Sensor Parameters

A detailed summary of performance parameters is shown in All of these factors need to be considered when selecting a motion compensation sensor. Based on the requirement that the primary radar sensor needs a phase compensation accuracy of 5 degrees or less, the only motion compensation sensor candidates are a secondary radar sensor and an ultrasonic sensor. Although a CW Doppler radar has range ambiguity, since phase compensation only requires relative phase measurements, the CW radar sensor meets the selection criteria. See Table 8.

Table 12. Sensor tradeoff Matrix. Radar phase provides the highest resolution and the ultrasonic sensor provides an absolute range measurement capability.

Sensor Type	Resolution	Drift/Range Ambiguity	Algorithm Complexity	Hardware Complexity	Operational Complexity	Beamwidth	SWaP	Cost
GPS	Standard: 7 m Differential: 1 cm	Short term drift: High Long term drift: Low	High	Low: chipset	Medium: Outdoor coverage only	N/A	Medium: 15mW	Low: ~$25
IMU	.3 to 1.15% of total motion [1]	Drift: High	High: Enhanced Kalman Filter	Low: MEMS module	Low	N/A	Low	Low: ~$25
RF Position Mapping	7 cm @ 2.4 GHz, SD = 1.3 deg, range = 3 m	Requires Calibration	High: Mean Square Estimation	High: switched antenna array	High: Requires Calibration	~ 60 deg	Medium	High: > $100+
Radar Phase MDU 1020	**.84 mm** 10 GHz @ 10 deg phase noise	Ambiguous Range	Low	Low: COTS modules	Low	36 deg	Low: 200 mW	Low: ~ $20
FMCW Radar (K-MC4)	0.8 m 24 GHz	Medium to Long Range	Low	Low: COTS modules	Low	30 deg	Low: 700mW	Low: ~ $20
FSK Radar (K-MC4)	2.7 cm 24 GHz	Medium Range	Low	Low: COTS modules	Low	30 deg	Low: 700mW	Low: ~ $20
Radar Tag	.84 mm	Motion Extraction	Low	Low: RFID tag	Medium (tag req'd)	< 10 deg	Low	Low: ~ $10
Ultrasonic	**6 mm**	No Range Ambiguity	Low	Low: COTS modules	Low	6 deg	Low: 75 mW	Low: ~ $5
Lidar	1 cm	N/A	Medium	Medium	Low	.5 deg	Medium: 650mW	Med: $ 100

15.1.1 Resolution

Resolution is a key metric as it will determine the precision and accuracy of the overall platform stabilization and motion compensation capability. GPS resolution at 7 m to 10 m is too coarse for this application. FMCW with a 250MHz sweep bandwidth only permits 0.8 m of range resolution. IMU calculated positions will drift several meters within a few seconds unless external updates are provided. The only viable sensors with sufficient resolution are range sensors that can resolve the radar signal phase change at fractional wavelengths. For a 10 GHz radar, where the wavelength is 30 mm, 1 mm of resolution corresponds to 12 degrees of phase motion.

15.1.2 Drift and Range Ambiguity

IMU position measurement errors can accumulate rapidly (within a few seconds) to several meters. Zero Velocity Updates (ZUPT) can remove the drift errors by providing a calibration update when there's a known stationary surface that bounds the error [3]. ZUPT performance has been proven for locating persons that are walking by registering the zero velocity events that occur when the shoe impacts the floor surface. This technique, however, is not applicable to airborne platform motion compensation since there is no fixed surface to provide the zero velocity reference.

15.1.3 Hardware and Algorithm Complexity

Hardware complexity is an issue for a size, weight and power constrained sensor platform such as a UAV or battery powered handheld device.

Algorithm complexity increases the demands on the processor capability and translates to higher power requirements for high performance processors. This eliminates computationally intensive solutions such as RF position mapping.

15.1.4 Operational Complexity

Operational considerations should also be taken into account when selecting the sensor. Indoor operations preclude GPS/GNSS sensors. Systems that require pre-calibration may not be practical. RFID tags can provide a motion compensation reference, however, the RFID tag would need to be placed in close proximity to the target individual. This would require the tags to be deployed by the mobile platform onto the ground within the radar beamwidth to provide the ground reference and isolate the platform motion.

15.1.5 Sensor Beamwidth

For the case where a secondary radar or ultrasonic sensor is used to measure the platform motion, the secondary sensor beams must not overlap the target. If there is overlap, the target physiological motion will be detected by the secondary sensor and erroneously contribute to the platform motion error signal. This is illustrated in Figure 44.

15.1.6 Size, Weight and Power (SWaP)

Low SWaP is a key requirement for a quadcopter platform given the limited payload capacity and battery life limits. Small form factor, light weight and low power radar, ultrasonic and lidar modules are available as Commercial Off-the-Shelf (COTS) devices. These are available from multiple sources such as RFBeam Microwave, GmBH, Sparkfun and others. Power consumption ranges from 70 mW for an ultrasonic sensor, 200 mW for a 10 GHz radar module and 700 mW for a lidar module.

15.1.7 Cost

The X-band (10 GHz) and K-band (24 GHz) radar modules can be purchased for less than $100. The ultrasonic sensors are less than $5 and the lidar module is $150 at the time of this writing.

All of these factors need to be considered when selecting a motion compensation sensor. Based on the requirement that the primary radar sensor needs a phase compensation accuracy of 5 degrees or less, the only motion compensation sensor candidates are a secondary radar sensor and an ultrasonic sensor. Although a CW Doppler radar has range ambiguity, since phase compensation only requires relative phase measurements, the CW radar sensor meets the selection criteria. See Table 8.

16.0 Platform Stabilization and Motion Compensation Techniques

Platform stabilization can reduce the amount of undesired vertical and horizontal motion that corrupts the radar sensor signal. This can be accomplished by sensing the platform motion and using a feedback control loop to drive an actuator or adjust the Electronic Speed Controller, in the case of a quadcopter, to compensate for the motion. Even if the platform motion isn't completely removed, the reduction in motion amplitude will reduce the phase distortion to a level that the baseband motion compensation can be effective.

Motion compensation can be implemented in the demodulated baseband radar signal to remove the unwanted phase modulation induced by the platform motion.

An analogy for platform stabilization and motion compensation are the image de-blurring techniques used in digital cameras. Nikon uses a vibration reduction method that employs voice coil motors that physically moves the optics in proportion to the unwanted yaw and pitch motion that occurs when the shutter button is depressed. See Figure 42

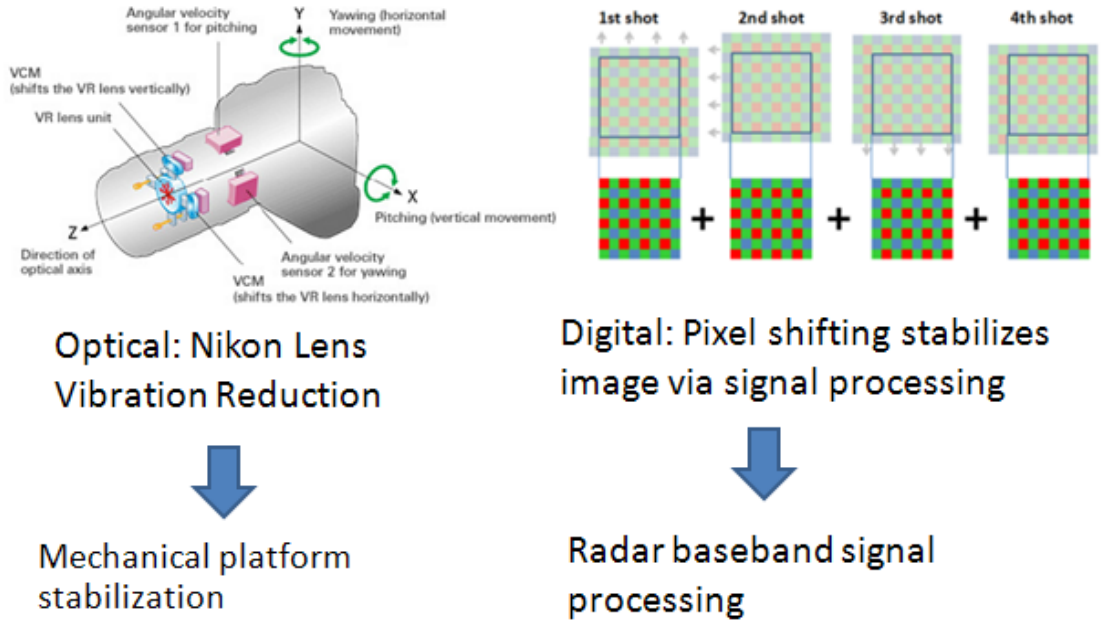

Figure 42. Camera De-blurring.

Mechanical and digital motion compensation techniques for cameras: (a) mechanical stabilization removes camera shake use 2 axis Voice Coil Motors to de-blur the image (b) signal processing shifts pixels to compensate for motion.

Algorithms and experiments for both the platform stabilization and motion compensation are described in the following sections. First, a review of the radar equation for physiological monitoring is described.

17.0 Radar Systems for Physiological Monitoring

Applications of Doppler radar systems range from military target tracking to civilian systems such as air traffic control, weather tracking or police speed radars. Measurement of physiological vital signs has been well established and reported in the literature since the 1970s [7], [8].

The radar equation describes the signal transmission and reception when the transmitted waveform is reflected from a target object with a given Radar Cross Section (RCS).

Doppler radar measures target motion via the return signal phase. The Doppler effect and range to target are described by

$$\Delta f = \frac{2\,f\,v(t)}{c} = \frac{2\,v(t)}{\lambda} \quad \text{and} \quad R = \frac{c\,T}{2} \tag{26}$$

Where Δf is the receiver frequency shift, f is the transmitter frequency, v(t) is the target velocity, c is the speed of light, λ is the RF wavelength and T is the measured transit time between transmission and reception.

The radar transmits the waveform

$$T(t) = \cos(2\pi f_t t + \phi(t)) \tag{27}$$

and the received waveform is

$$R(t) = \cos(2\pi f_t t + \theta + p(t) + \phi(t - 2R/c)) \tag{28}$$

where f_t is the transmitter frequency, $\phi(t)$ is the transmitter phase offset, θ is the receiver phase offset, p(t) is the phase modulation from the respiration motion and $\phi(t - 2R/c)$ is the phase delay due to the roundtrip signal propagation.

A coherent receiver downconverts the received signal by mixing the received signal with a quadrature mixer. The quadrature mixer uses a phase shifter to generate a quadrature component that is shifted by 90 degrees. This allows the received signal to be deconstructed into two components that are 90 degrees apart, thus ensuring that when the in-phase component is at a null, the quadrature component is at a peak.

Quadrature decomposition also mathematically allows any complex signal to be represented by its orthogonal components with appropriate amplitude and phase scaling. See Figure 43.

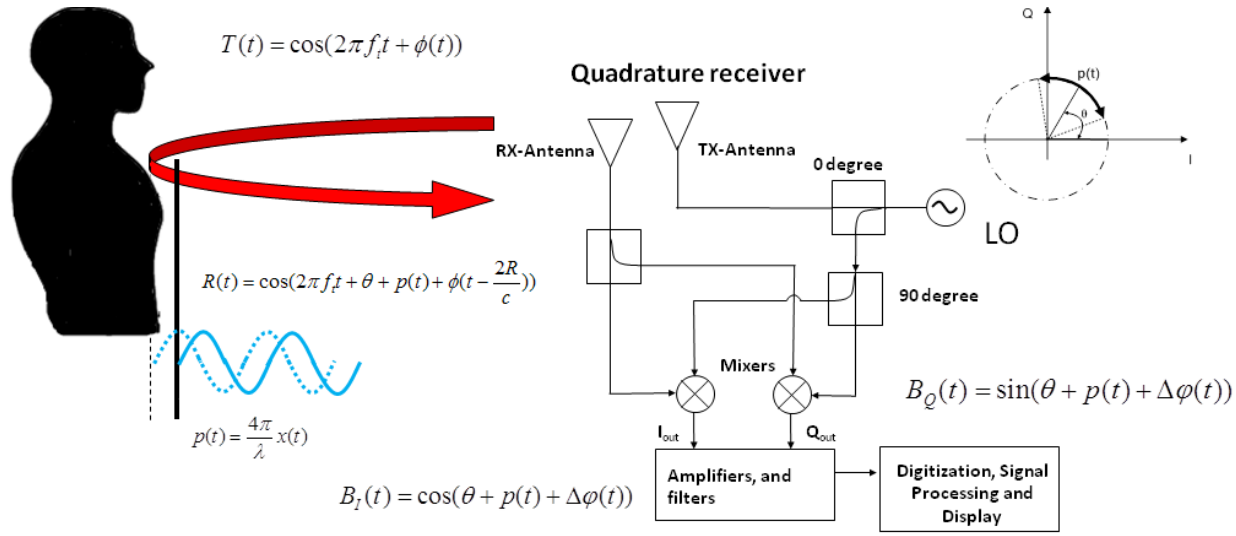

f_t : RF frequency

θ : Constant phase shift

Figure 43. Radar transceiver block diagram and signal components for physiological monitoring.

Radar transceiver architecture with transmitted and received waveform equations showing phase modulation from the respiration motion [courtesy of Xiaomeng Gao]

Since the received signal is multiplied by the same Local Oscillator (LO) as the transmitter LO, the transmitted and received signals are said to be coherent. Multiplying the received signal by the LO downconverts the RF signal to baseband. Since the receiver LO is a replica of the transmitter LO, any phase noise or frequency drift is also removed in the downconversion process.

The two receiver channels are referred to as a in-phase (I) channel and quadrature phase (Q) channel. The I and Q channels are represented as

$$B_I(t) = \cos[\theta + p(t) + \Delta\phi(t)] \quad \text{and} \quad B_Q(t) = \sin[\theta + p(t) + \Delta\phi(t)] \tag{29}$$

where p(t) is the phase modulated signal of interest that is corrupted by the platform motion that manifests as a phase term, Δϕ(t).

Note that the chest displacement x(t) will contribute to the magnitude of the reflected signal. Thus the Signal to Noise Ratio (SNR) will vary with the magnitude of the respiration motion with the overall SNR determined by the antenna gain, transmitter power, receiver gain, receiver noise figure, range and background clutter.

Let the physiological motion of the thorax expanding and contracting be defined as $\mathrm{x(t)}$.The resulting phase modulation component from the variable range to the thorax detected by the radar is

$$p(t) = \frac{4\pi}{\lambda}\mathrm{x(t)} \tag{30}$$

The average respiration motion is 4 to 12 mm and the average adult respiration rate is 12 to 15 Breaths per Minute (BPM) [5]. The typical chest wall displacement from cardiac pumping is .5 mm to 1.5 mm thorax displacement [22].

Detecting the respiration signal p(t) in the presence of platform motion requires suppression of the Δϕ(t) term. The remaining sections of this dissertation describe techniques to recover the signal using sensor fusion to stabilize the platform and signal processing to compensate for the platform motion.

18.0 Two Stage Platform Stabilization and Motion Compensation

Platform stabilization and motion compensation techniques can be applied to remove the signal distortion introduced by platform motion. The ideal secondary sensors that generate the in-range error signals generated by the platform motion are radar and ultrasonic sensors, as summarized in the previous section. This sensor geometry is shown in Figure 44 below. The cross-range motion sensor is discussed in a later section.

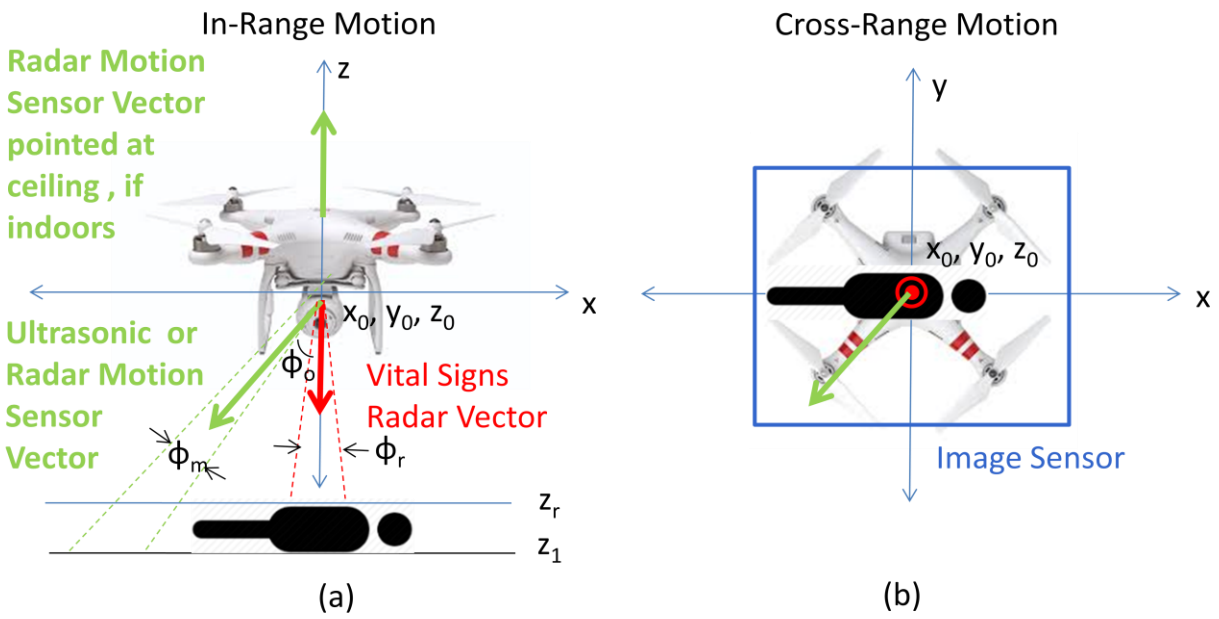

Figure 44. UAV radar remote sensing platform sensor geometries.

(a) Position sensor (e.g. GPS, IMU) measures x_0 (t), y_0 (t), z_0 (t) within resolution and drift constraints. Range sensor (e.g. radar) measures z0 (t) - z1 (t)
(b) Cross range sensor (radar RSSI, image) measures x0 (t) - x (t) and y0 (t) - y (t). Care must be exercised such that (Φm/2 + Φr/2) < Φo to avoid range sensor and vital sign sensor overlap; Φo = 30 deg

Similar to the camera stabilization analogy described earlier, we evaluated a mechanical stabilization feedback loop to reduce the overall motion and a post-detection baseband motion compensation algorithm. See Figure 45. The mechanical stabilization uses an ultrasonic or radar sensor derived error signal to physically cancel the platform motion. Perfect cancellation is not expected due to sensor errors and feedback loop gain mismatches and loop delays.

PID feedback loops, shown in Figure 46, were also evaluated to optimize the mechanical compensation feedback control. PID controllers apply proportional gain (P), integration (I) and derivative (D) components of the motion error signal to the feedback control signal.

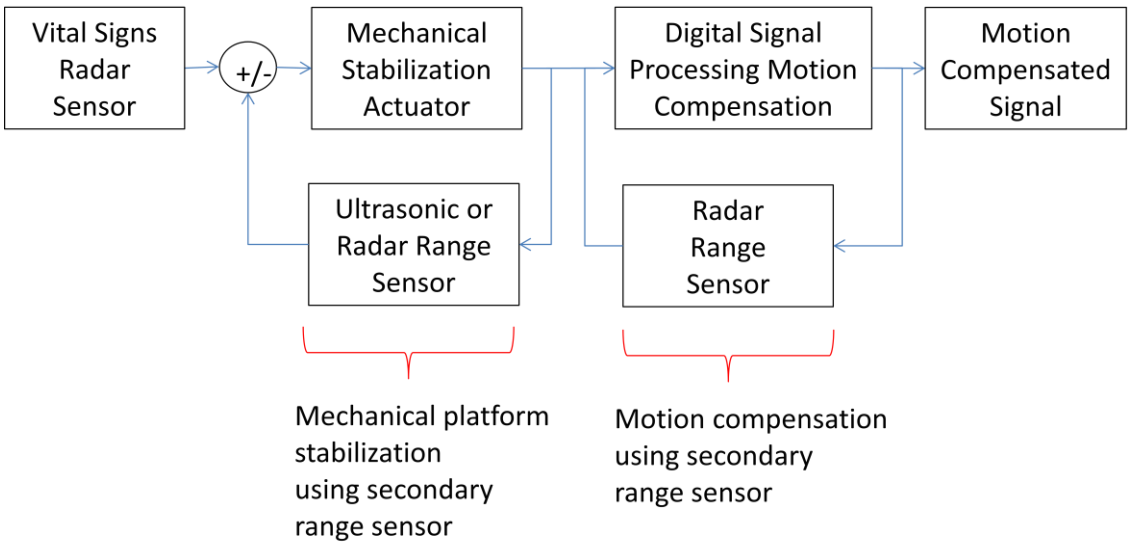

Figure 45. Two stage platform stabilization and motion compensation.

Mechanical platform stabilization uses an ultrasonic or radar sensor to drive a mechanical actuator to cancel the platform motion. DSP motion compensation uses the secondary radar sensor phase to apply phase compensation to the received signal.

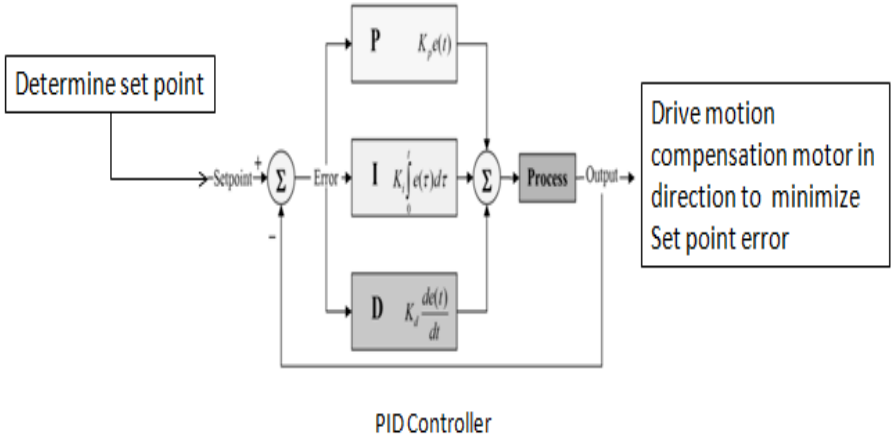

Figure 46. PID controller in the platform stabilization feedback loop.

The second stage processes the baseband signal with a motion compensation algorithm using the secondary radar range sensor. This is described in detail in the following section.

19.0 Motion Compensation Analysis and Simulation

The effect of platform motion on the primary radar sensor signal is described and analyzed in this section. The system is modeled and simulated using MATLAB and the results are analyzed to predict the system behavior and later compared with experimental measurements to confirm the simulations.

The time domain representations for the vital sign signal of interest (modeled as a sinusoid for simplicity but applicable to complex signals because of superposition) and platform motion components are:

$$\text{respiration signal:} \quad x_1(t) = A \sin(\omega_1 t) \tag{31}$$

$$\text{platform motion:} \quad x_2(t) = B \sin(\omega_2 t) \tag{32}$$

where $\omega_1 = 2\pi f_1$ and $\omega_2 = 2\pi f_2$ are the angular frequencies for the respiration signal to be recovered and the undesirable platform motion, respectively. Substituting Equation 31 and Equation 32 into Equation 30, the respiration baseband radar signal is

$$S_{Resp}(t) = \cos\left[\frac{4\pi}{\lambda} A\sin(\omega 1t)\right] \tag{33}$$

and the platform motion radar signal is

$$S_{Plat}(t) = \cos\left[\frac{4\pi}{\lambda} B\sin(\omega 2t)\right] \tag{34}$$

The combined composite motion detected by the primary radar sensor is

$$S_{Composite}(t) = \cos\left[\frac{\mathbf{4\pi}}{\boldsymbol{\lambda}} A\sin(\omega_1 t) + \frac{\mathbf{4\pi}}{\boldsymbol{\lambda}} B\sin(\omega_2 t)\right]. \tag{35}$$

Using the cosine angle sum identity:

$$\cos(a+b)=\cos(a)\cos(b)-\sin(a)\sin(b) \tag{36}$$

the composite motion detected by the radar is

$$\begin{aligned} S_{Comp}(t) &= \cos\left\{\frac{4\pi}{\lambda}[A\sin(\omega 1t)] + \frac{4\pi}{\lambda}[B\sin(\omega 2t)]\right\} \\ &= \cos\left\{\frac{4\pi}{\lambda}[A\sin(\omega_1 t)]\cos[(B\sin(\omega_2 t)] - \frac{4\pi}{\lambda}\sin[A\sin(\omega_1 t)]\sin[(B\sin(\omega_2 t)]\right. \end{aligned} \tag{37}$$

The compensated waveform $x_4(t)$ is derived from removing the phase modulation induced by the undesired platform motion within the composite phase terms.

$$x_4(t) = \cos\{[A\sin(\omega_1 t) + B\sin(\omega_2 t)] - B\sin(\omega_2 t)\}$$

where the terms in the brackets represent the composite waveform measured by the primary radar. Therefore, the two ω_2 sinusoid terms cannot be merely subtracted in the cosine expression.

Using the cosine angle difference identity,

$$\cos[(a+b)-a] = \cos(a+b)\cos(a) + \sin(a+b)\sin(a) \quad (38)$$

$$S_{compensated}(t) = \cos\{\frac{4\pi}{\lambda}[A\sin(\omega_1 t) + B\sin(\omega_2 t)]\cos[B\sin(\omega_2 t)]\} + \sin\{\frac{4\pi}{\lambda}[A\sin(\omega_1 t) + B\sin(\omega_2 t)]\sin[B\sin(\omega_2 t)]\} \quad (39)$$

As an alternative, the motion compensation phase can be analyzed in the complex IQ (In-phase and Quadrature) domain as depicted in Figure 47. The primary vital signs radar detects the composite motion while the secondary radar detects the platform motion with respect to the ground (or ceiling if indoors). By removing the platform motion phasor rotation from the composite motion phasor, the remaining phasor rotation is due to the respiration motion. The arc length corresponds to the amount of motion. A phenomenon referred to as phase wrapping occurs when the motion exceeds a half wavelength.

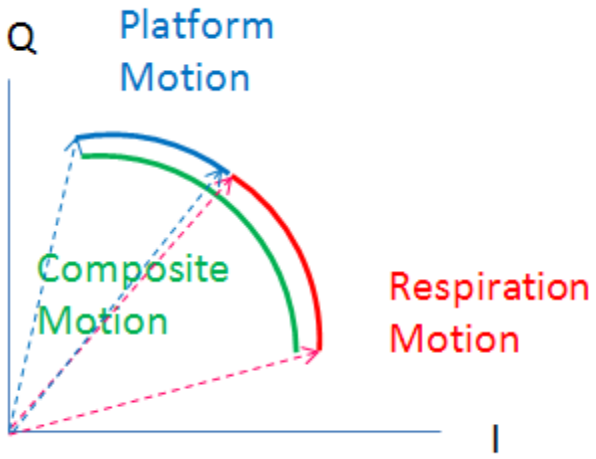

Figure 47. Phasor representation of the respiration motion, platform motion and combined motion.

The complex representations for each component are:

Respiration motion: respwav=A*real[exp(j*2*pi*respfreq*t)] (40)

Platform motion: platwav=B*real[exp(j*2*pi*platfreq*t)] (41)

composite = A*B* real[exp(j*4*pi/lambda*(respwav+platwav))] (42)

compensated =A*B*real[exp(j*4*pi/lambda*(composite-platwav))] (43)

The MATLAB code for the simulation is found in the appendix. The plots in Figure 48 below show the simulated platform motion and respiration motion, the radar baseband waveforms and the composite and compensated waveforms for the case with a sinusoidal platform motion with 17 mm amplitude at .75 Hz and a 3mm amplitude respiration waveform at .25 Hz. Since the amplitude of the platform motion exceeds one half of the radar wavelength, a phenomenon known as phase wrap occurs. This is evident in the top right subplot for the radar baseband signal and also occurs in the composite and compensated signals.

For motion amplitudes exceeding one half of the wavelength where phase wrapping occurs, the envelope of the compensated waveform corresponds to the respiration motion. This envelope can be extracted to recover the target waveform and rate.

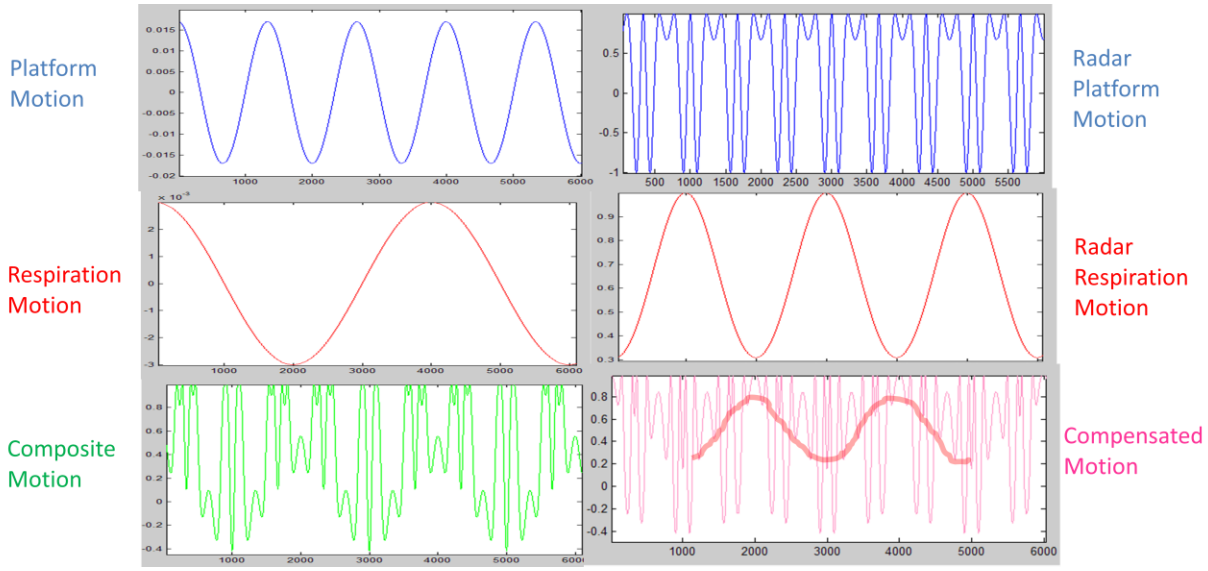

Figure 48. Time domain simulation of the platform and respiration radar waveforms for 17 mm platform amplitude and 3mm respiration amplitude. The platform motion exceeds ½ of the radar wavelength and results in phase wrapping in the platform, composite and compensated radar baseband waveforms.

20.0 Experiment Configuration

The motion compensation experiment block diagram is shown in Figure 49. Platform stabilization and motion compensation experiment test bed.The target signal of interest is created with the Mover 1 linear actuator representing respiration motion. The UAV platform motion is created with Mover 3 using a programmable linear actuator from Galil Motion Systems. The platform stabilization corrective motion is created with Mover 2. Mover 2 was implemented using a slide potentiometer linear actuator mounted on wheels to allow independent motion from the Mover 3 base platform. An Arduino UNO controller was programmed to control the position of Mover 2 in real time based on the ultrasonic sensor or secondary range value. If optimally implemented, Mover 2 will cancel the undesirable Mover 3 motion. The test platform hardware configuration is shown in Figure 49 to Figure 52.

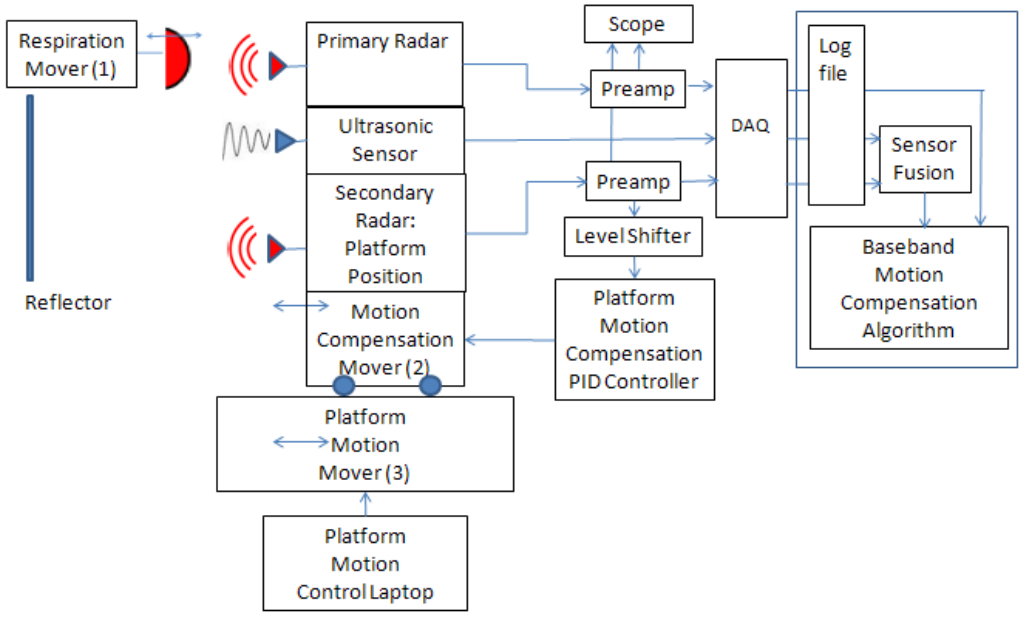

Figure 49. Platform stabilization and motion compensation experiment test bed.

Motion compensation experiment configuration block diagram. The respiration signal of interest (Mover 1) is detected by the primary radar that is mounted on the motion compensator (Mover 2) that is mounted on the base platform representing the unwanted motion from a UAV (Mover 3). Mover 2 is driven by either an ultrasonic sensor or a secondary radar sensor that detects the platform motion relative to a stationary reflector.

The primary radar output signal is amplified by a pre-amp with a passband from 0.3 Hz to 10 Hz and a gain of 20 dB. The preamp output is digitized by a National Instruments DAC set at a 1 KHz sampling rate. The data acquisition (DAQ) is configured with a LabView Graphical User Interface (GUI) and the data log files are saved as text files that are post-processed in MATLAB.

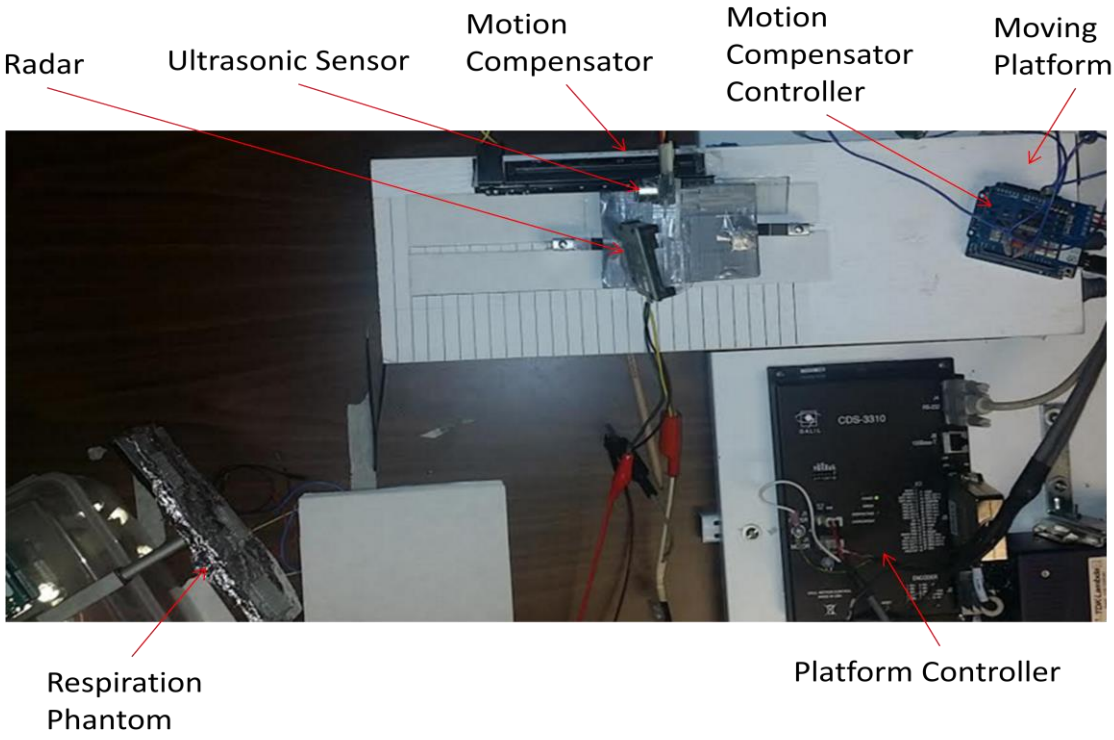

Figure 50. Experiment test bed.

Top view of motion compensation test bench components. Motion compensator (top center) is mounted on wheeled cart mounted on platform motion actuator (white plate). Ultrasonic sensor is pointed at flat plate to the left (not shown) representing the ground. Radar is pointed at respiration phantom (lower left).

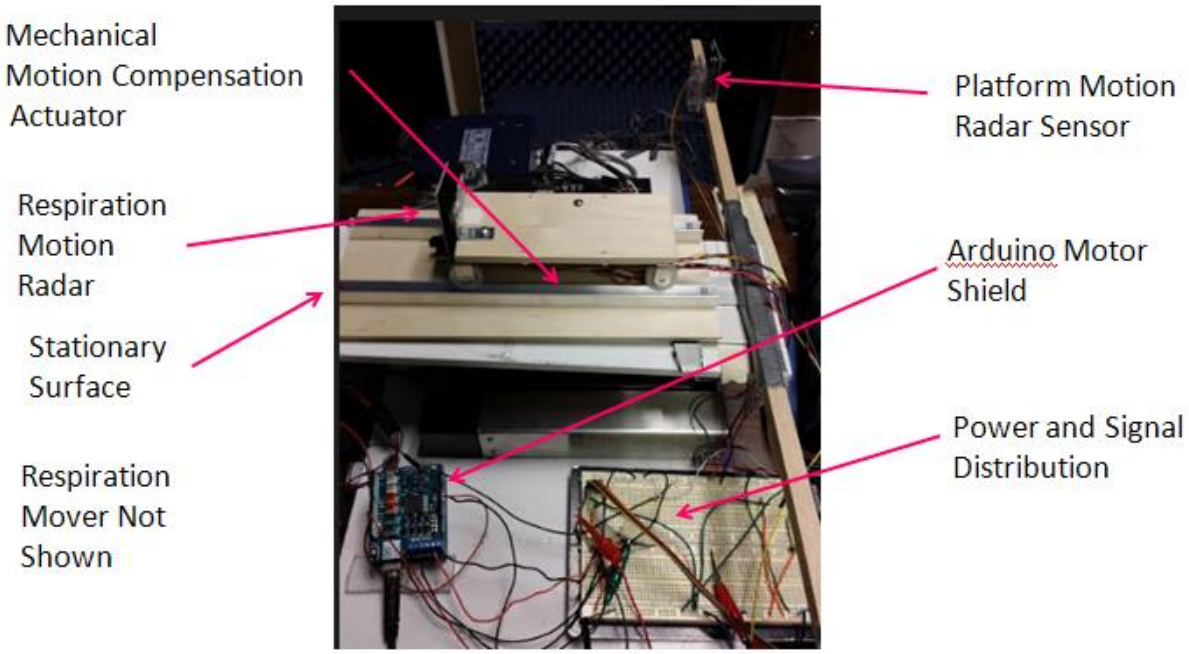

Figure 51. Second experiment test bed with platform motion radar sensor and improved motion compensation track.

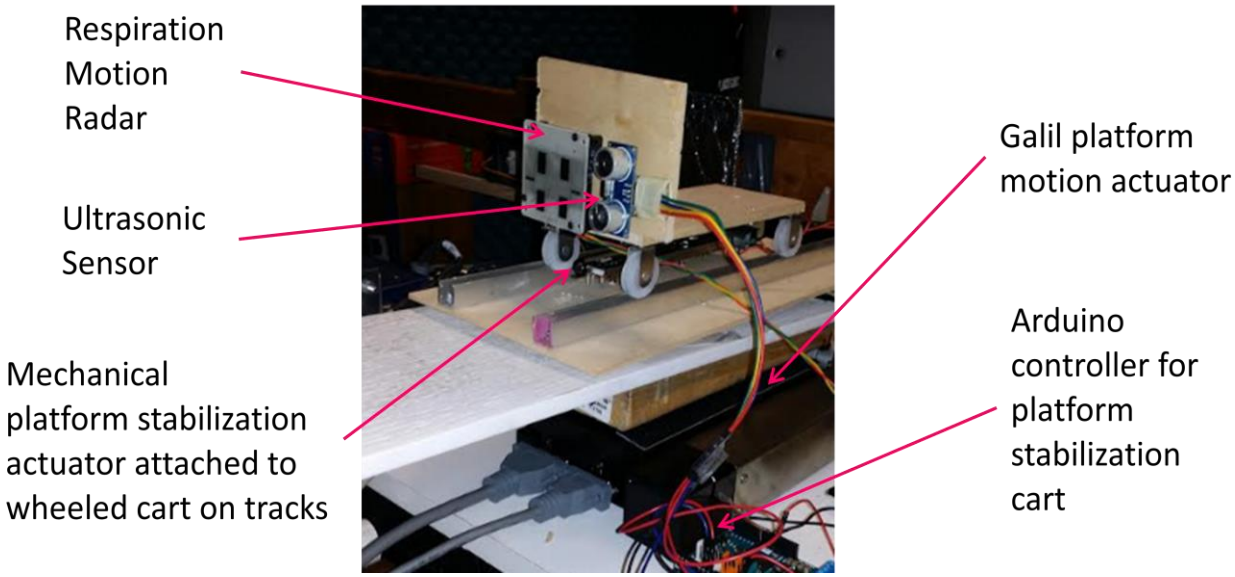

Figure 52. Platform stabilization cart with ultrasonic sensor and primary radar sensor.

21.0 Motion Compensation Experiments and Results

The following data analysis sections compare the following categories of test cases:

a. Motion compensation suppression with platform motion only
b. Motion compensation with platform motion and respiration motion combined showing SIR improvement and harmonics suppression
c. Platform stabilization using an ultrasonic sensor alone
d. Platform stabilization with ultrasonic sensor and motion compensation with secondary radar motion compensation
e. Platform stabilization using radar sensor alone
f. Platform stabilization with radar sensor and motion compensation with secondary radar motion compensation.

21.1 Motion Compensation Algorithm Performance with Platform Motion Only

Initial tests and measurements were made without mechanical platform stabilization. This was done to isolate the effect of motion compensation alone. The data was collected using the test bed shown in Figure 49 to Figure 52. The primary radar signal is amplified, band pass filtered and digitized using a National Instruments Analog to Digital Converter (ADC) at a 1 KHz sampling rate. The signal flow is highlighted in Figure 53.

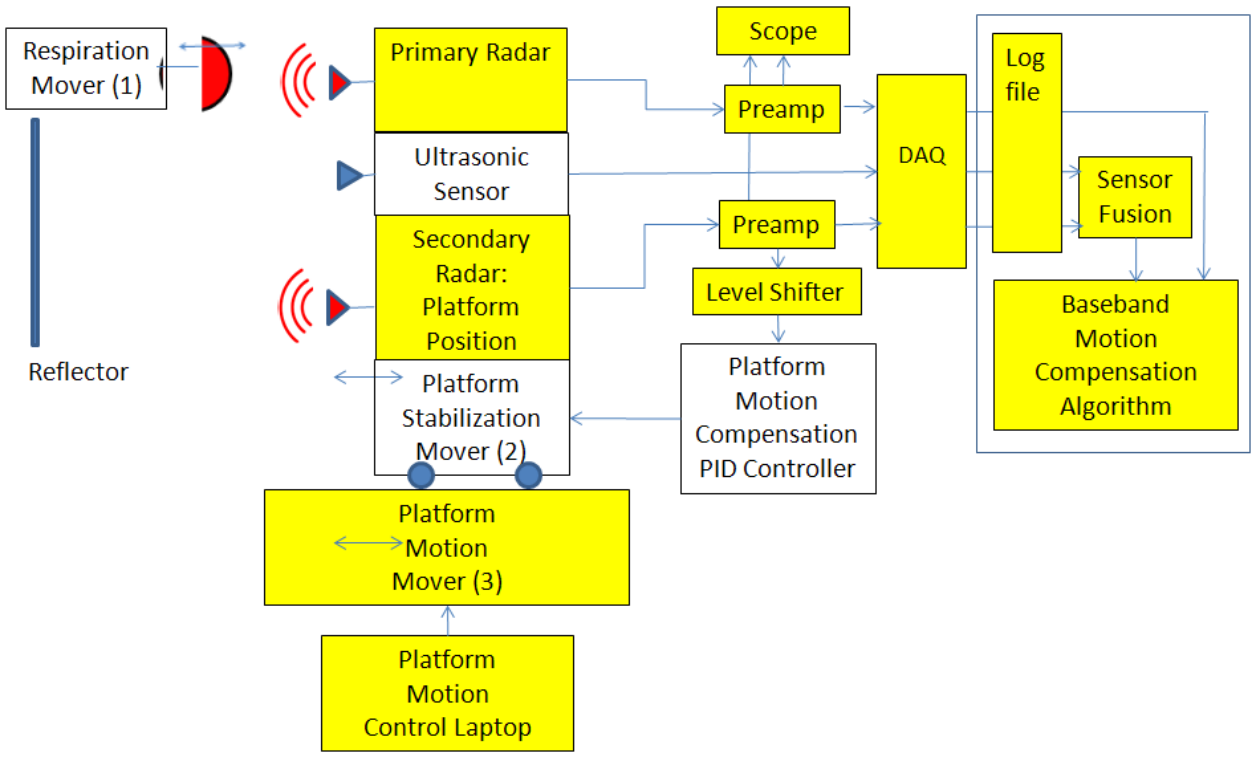

Figure 53. Motion compensation experiment with platform motion only. Components used for the experiment are highlighted.

A LabView Graphical User Interface (GUI) is used to configure the data collection and generate data log files. The .txt log files are then processed off-line using MATLAb code written to perform the phase compensation algorithm described earlier and time domain and frequency spectrum plots are generated. The MATLAB code is included in the Appendix. In each test case, the platform motion and respiration motion is specified to show the effectiveness of the motion compensation algorithm by comparing the Signal to Interference Ratio (SIR) before and after the baseband motion compensation.

Since the Signal to Noise (SNR) is a function of the receiver Noise Figure (NF) and the resulting noise equivalent bandwidth as determined by the receiver pass band that varies by receiver design, a convenient metric is to compare the SIR. Factors such as the receiver noise equivalent bandwidth and thermal noise are not relevant to the motion compensation gain and therefore the SIR is an appropriate benchmark to assess the motion compensation performance improvement.

The SIR is defined by

$$SIR = 10*\log[(V_{resp})^2/(V_{plat})^2] = 0\ dB \quad (44)$$

where Vresp is the voltage magnitude of the respiration signal and Vplat is the magnitude of the platform signal in the frequency domain. The SIR metric is illustrated in Figure 54 below.

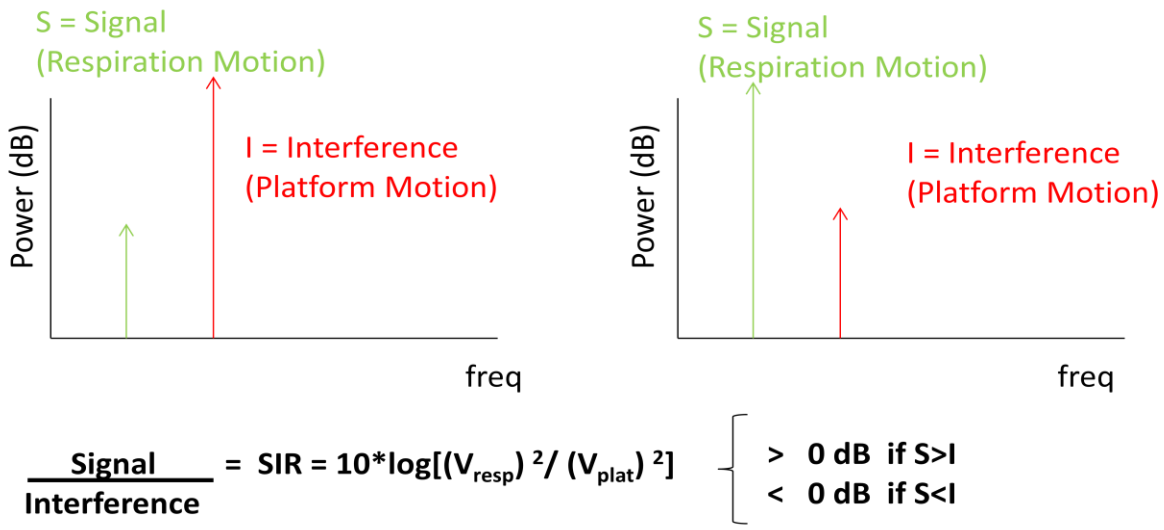

Figure 54. Signal to Interference Ratio definition.

The effectiveness of the motion compensation algorithm in removing the platform motion is shown in Figure 55 to Figure 59 for progressively larger displacements. If the platform motion is perfectly canceled, the compensated waveform should be a constant value. In each case, the compensated waveform shows a relatively flat line, as it should be, when the platform motion is removed. The harmonic content introduced by the phase wraparound is also suppressed by the motion compensation signal processing.

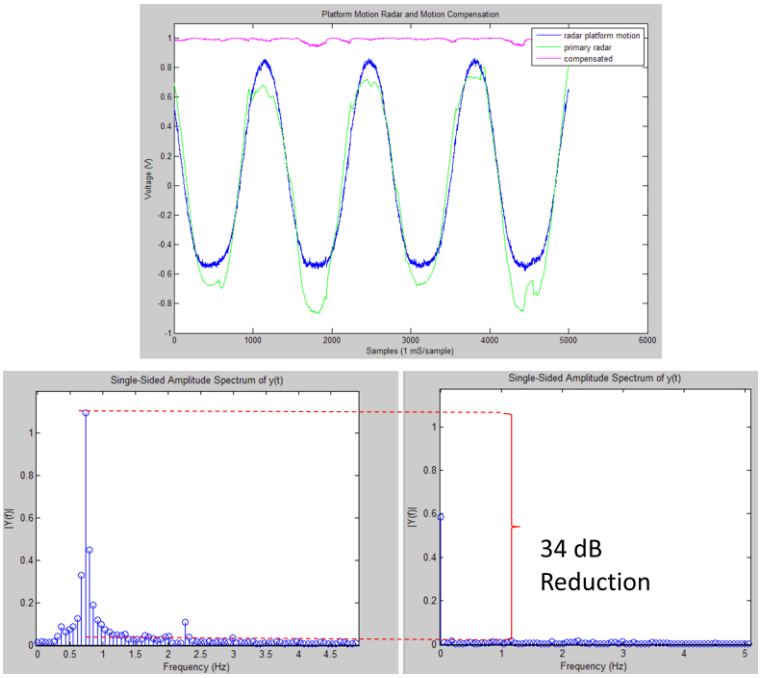

Figure 55. Motion Compensation Algorithm – Platform Motion Only Platform Motion: 6 mm, .75 Hz. (top): platform motion and composite waveform (bottom left): before motion compensation (bottom right): after motion compensation.

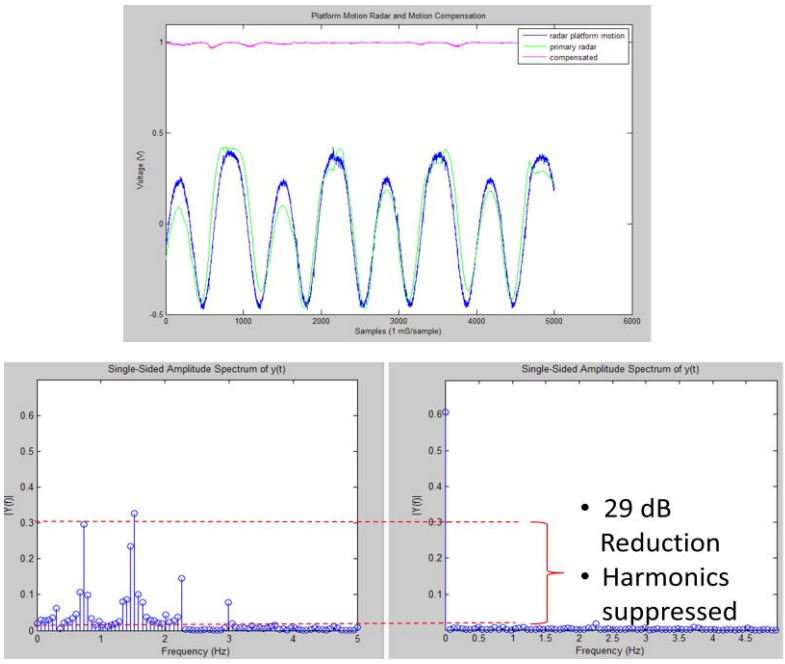

Figure 56. Motion Compensation Algorithm – Platform Motion Only Platform Motion: 12 mm, .75 Hz. (top): platform motion and composite waveform (bottom left): before motion compensation (bottom right): after motion compensation.

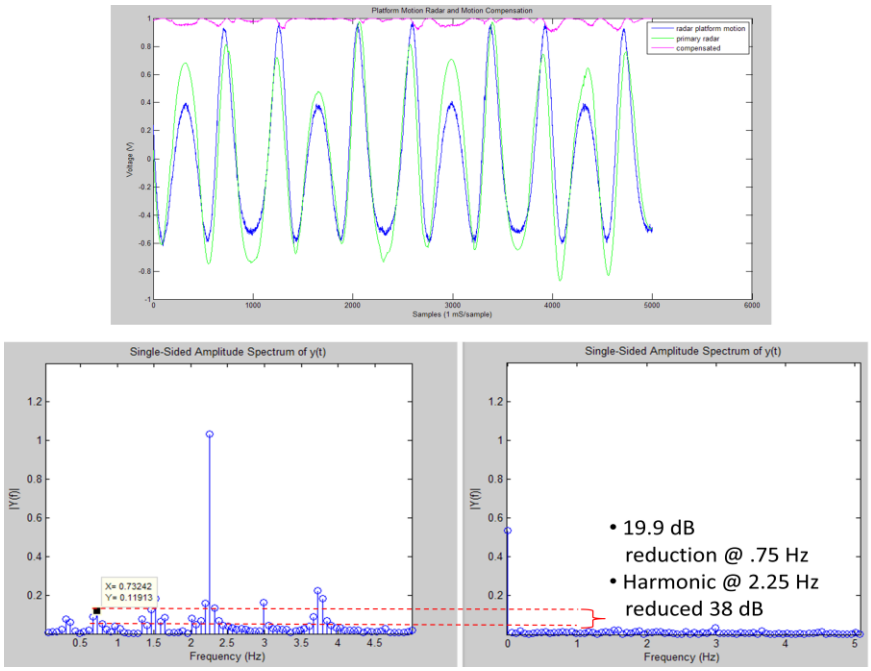

Figure 57. Motion Compensation Algorithm – Platform Motion Only Platform Motion: 18 mm, .75 Hz . (top): platform motion and composite waveform (bottom left): before motion compensation (bottom right): after motion compensation.

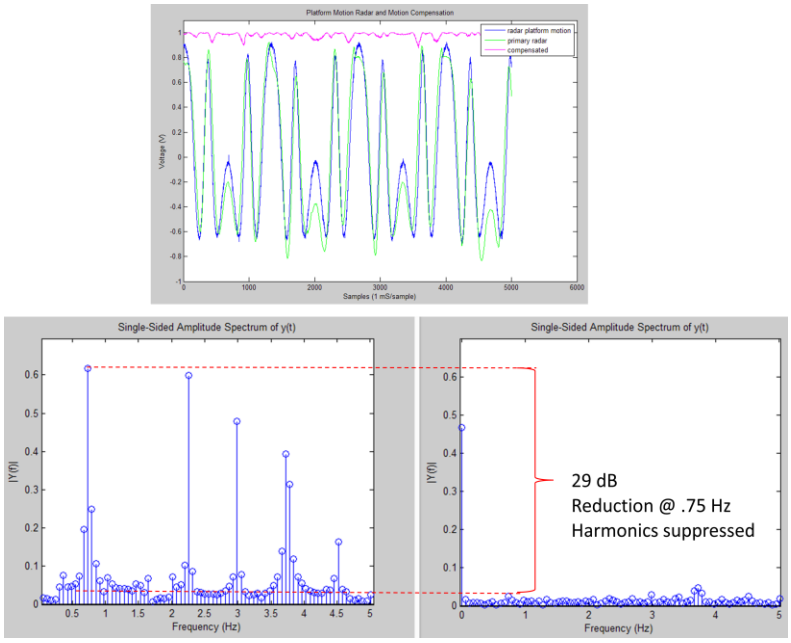

Figure 58. Motion Compensation Algorithm – Platform Motion Only Platform Motion: 22 mm, .75 Hz . (top): platform motion and composite waveform (bottom left): before motion compensation (bottom right): after motion compensation.

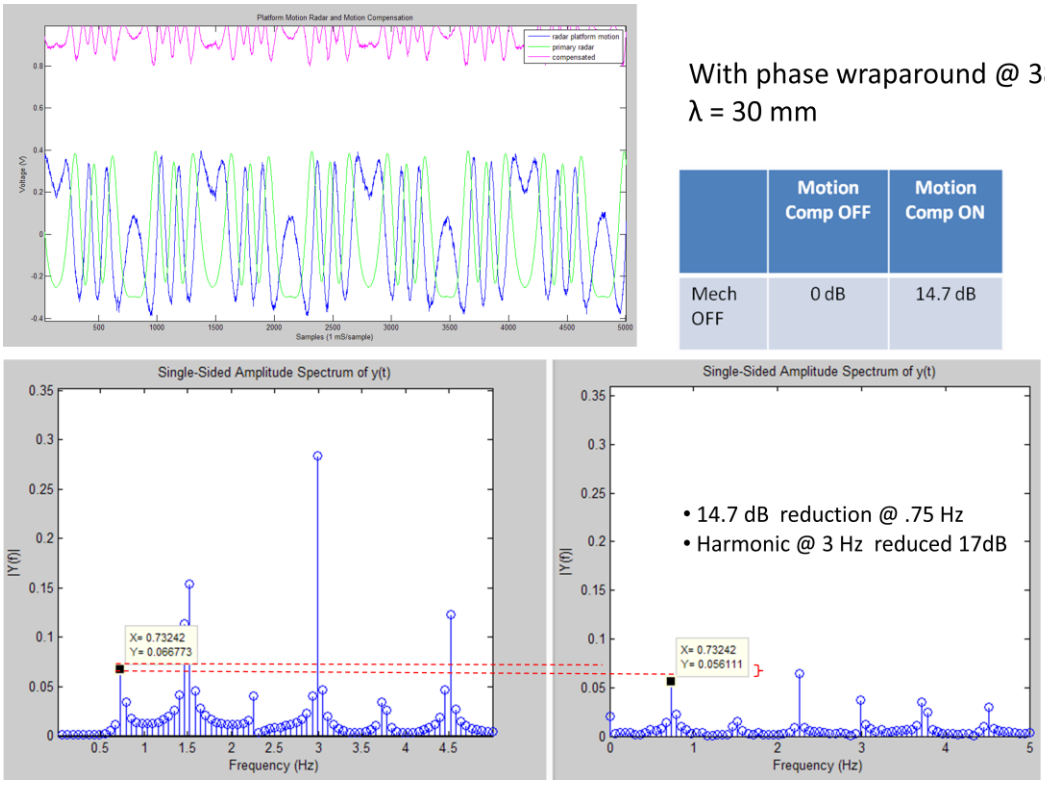

Figure 59. Motion compensation algorithm – Platform motion only.

Effect of motion compensation on platform motion at 0.75 Hz with 38 mm displacement that exceeds the 30 mm radar wavelength causing significant phase wraparound. Platform motion was reduced by only 1.4 dB.

Table 13 and Figure 60 summarize the motion compensation algorithm performance in reducing the magnitude of the platform motion. The amount of motion reduction diminishes with an increase in platform motion beyond the radar wavelength (30 mm at 10 GHz), as expected, due to the phase wrapping effects that occur with increased motion. Because there are significant harmonics, for this sequence of displacement tests, the contribution and suppression of the harmonics is included in the platform motion reduction value.

Table 13. Motion Compensation Platform Motion Reduction

Platform Motion	Platform Displacement	Mechanical Compensation	Motion Compensation	Signal to Interference Ratio (SIR)
0.75 Hz	6 mm	Off	On	41.9
0.75 Hz	12 mm	Off	On	35
0.75 Hz	18 mm	Off	On	40.9
0.75 Hz	22 mm	Off	On	41.5
0.75 Hz	38 mm	Off	On	15.8

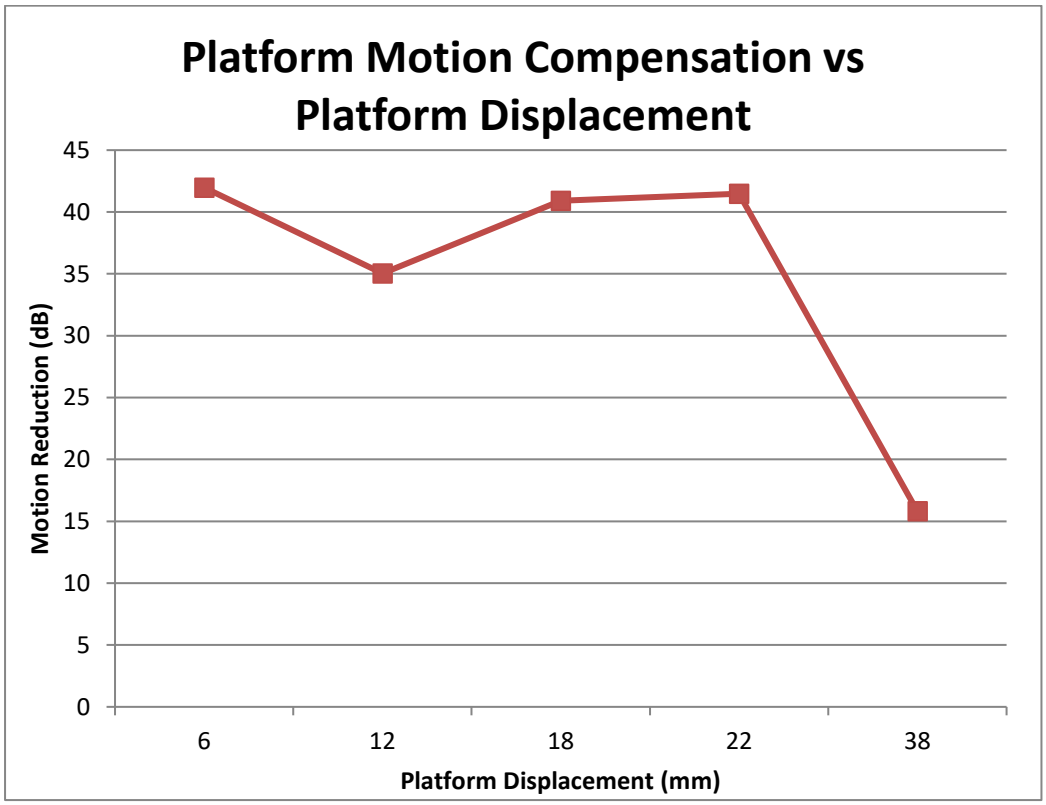

Figure 60. Motion compensation algorithm reduction in platform motion magnitude as a function of platform displacement.

21.2 Motion Compensation with Platform Motion and Respiration Motion (Without Platform Stabilization)

In this section, we evaluate the motion compensation algorithm performance for extracting the respiration signal in the presence of platform motion. The experiment configuration and signal flow are shown in Figure 61.

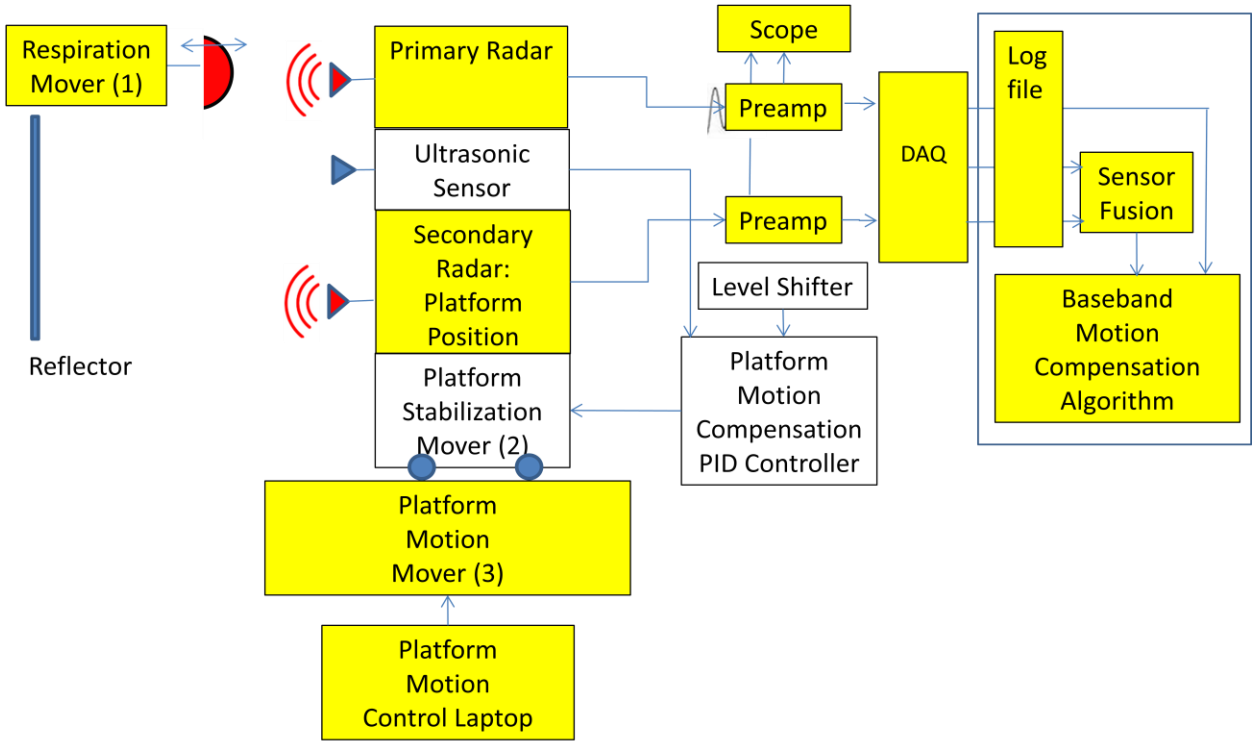

Figure 61. Motion compensation test signal flow with platform motion and respiration motion. Components used for the experiment are highlighted.

Data runs were collected and analyzed to evaluate the motion compensation algorithm performance. These are shown in the following sections for the following test cases:

- Sinusoidal platform motion in progressive displacements from 3 mm to 38 mm with simultaneous respiration motion with and without motion compensation.
- Sinusoidal platform motion and simultaneous respiration motion at various frequencies with and without motion compensation.
- Sinusoidal platform motion with the same frequency as respiration motion with and without motion compensation.

- Trapezoidal platform motion and simultaneous respiration motion with and without motion compensation.
- Step platform motion and respiration motion with and without motion compensation.

21.2.1 Motion Compensation Algorithm Performance as a Function of Platform Motion Displacement with Respiration Signal

In the following figures, the platform motion was progressively increased from 3 mm to 38 mm in the presence of a respiration motion signal to assess the performance of the motion compensation algorithm. Platform stabilization is disabled for these tests.

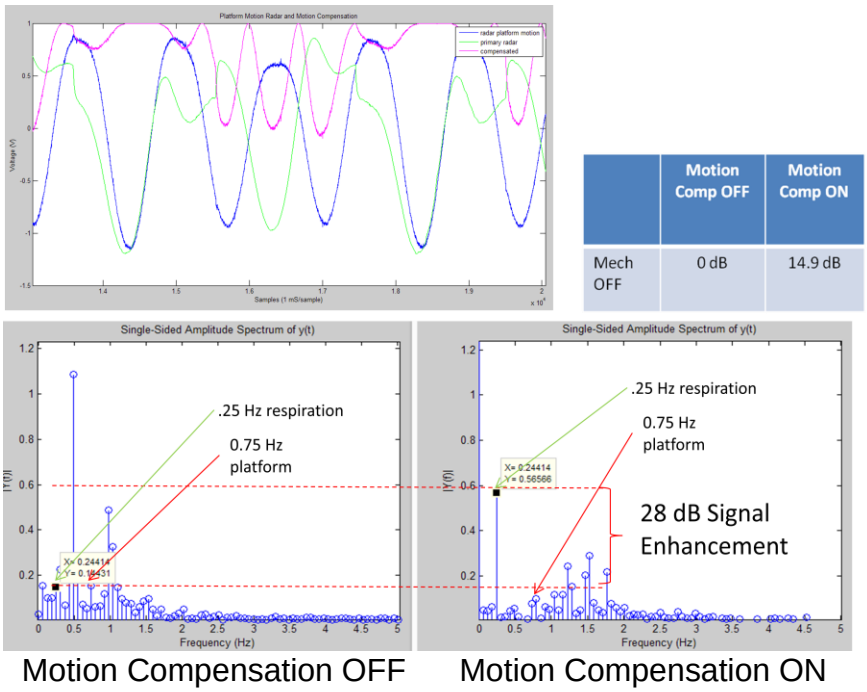

Figure 62. Motion compensation algorithm – Platform and respiration motion. 3 mm, .75 Hz Platform/3 mm, .25 Hz Respiration, mechanical compensation off

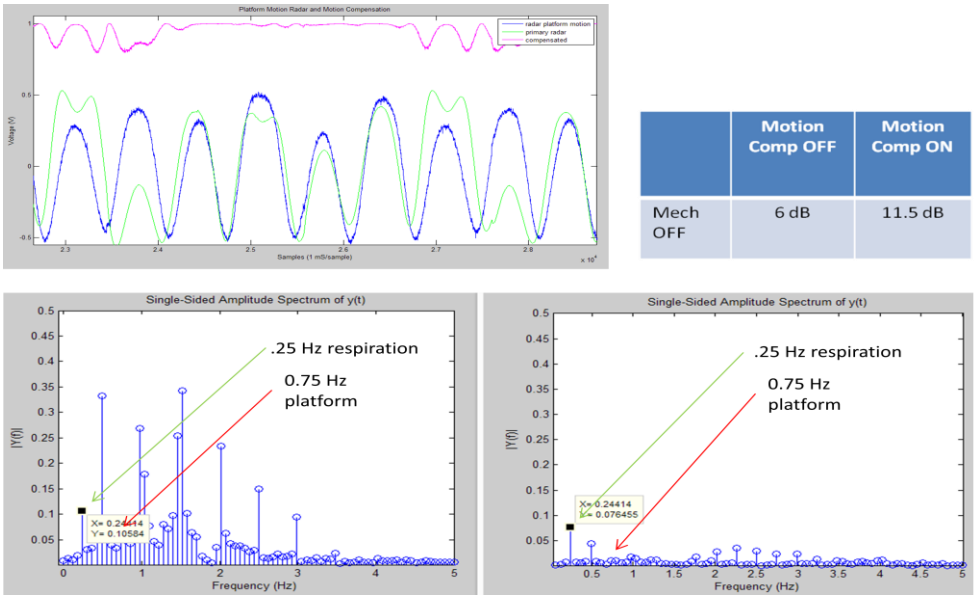

	Motion Comp OFF	Motion Comp ON
Mech OFF	6 dB	11.5 dB

Motion Compensation OFF Motion Compensation ON

Figure 63. Motion compensation algorithm – Platform and respiration motion. 12 mm, .75 Hz Platform/3mm, .25 Hz Respiration, mechanical compensation off The SIR amplitude ratio is 4:1 and introduces harmonics and sum and difference beat frequencies that are suppressed by the motion compensation algorithm.

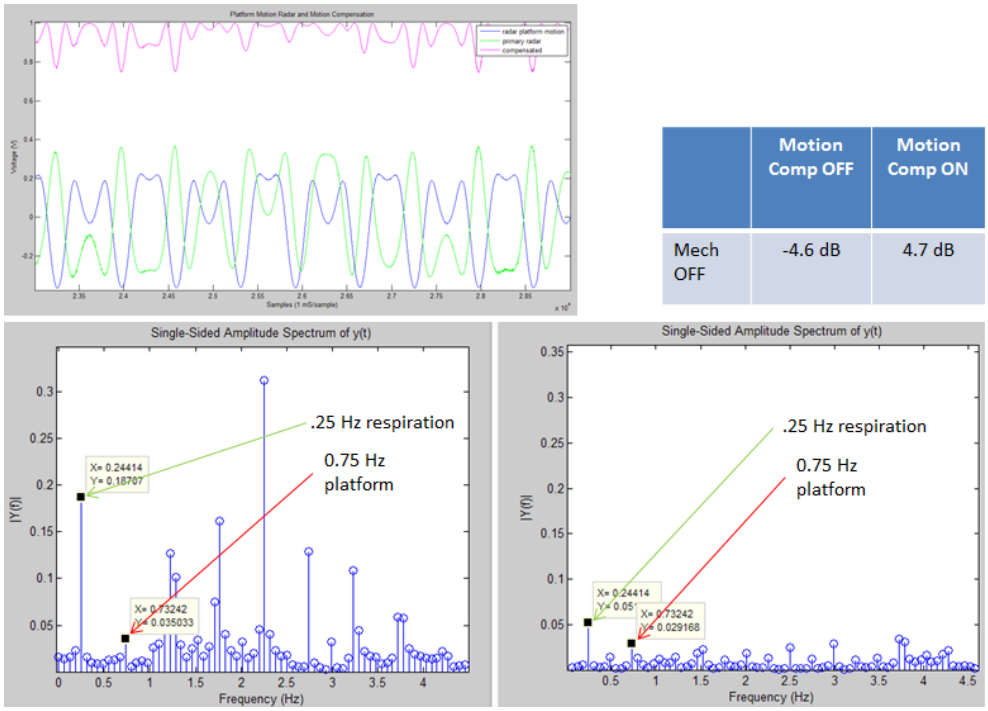

	Motion Comp OFF	Motion Comp ON
Mech OFF	-4.6 dB	4.7 dB

Motion Compensation OFF Motion Compensation ON

Figure 64. Motion Compensation Algorithm – Platform and Respiration Motion 17 mm, .75 Hz Platform/4.8 mm, .25 Hz Respiration

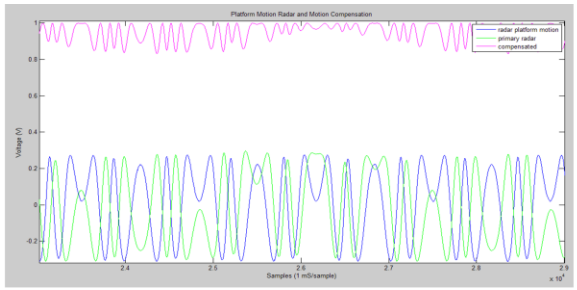

	Motion Comp OFF	Motion Comp ON
Mech OFF	-27 dB	6.5 dB

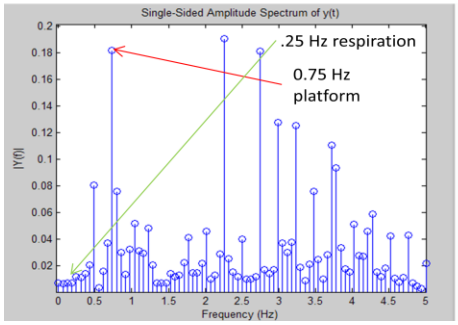

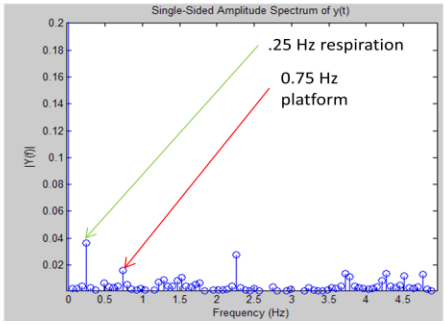

Motion Compensation OFF Motion Compensation ON

Figure 65. Motion Compensation Algorithm – Platform and Respiration Motion 23 mm, .75 Hz Platform/4.8 mm, .25 Hz Respiration

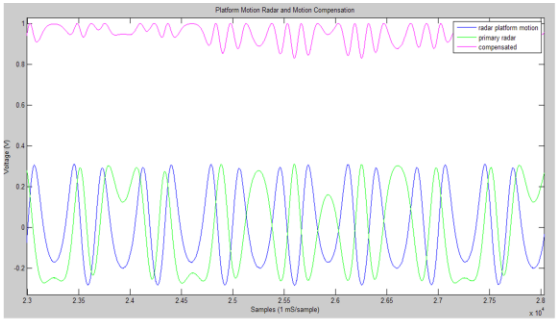

	Motion Comp OFF	Motion Comp ON
Mech OFF	3.5 dB	26.8 dB

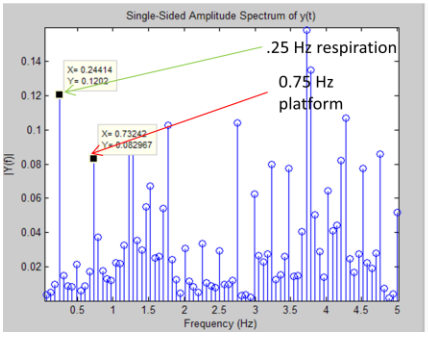

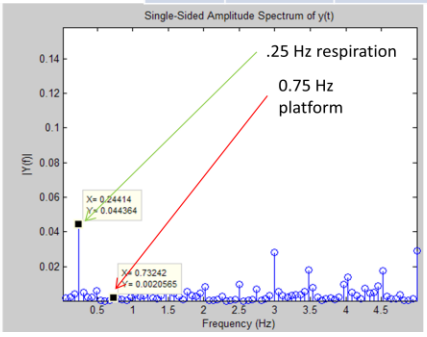

Motion Compensation OFF Motion Compensation ON

Figure 66. Motion Compensation Algorithm – Platform and Respiration Motion 27 mm, .75 Hz Platform/4.8 mm, .25 Hz Respiration

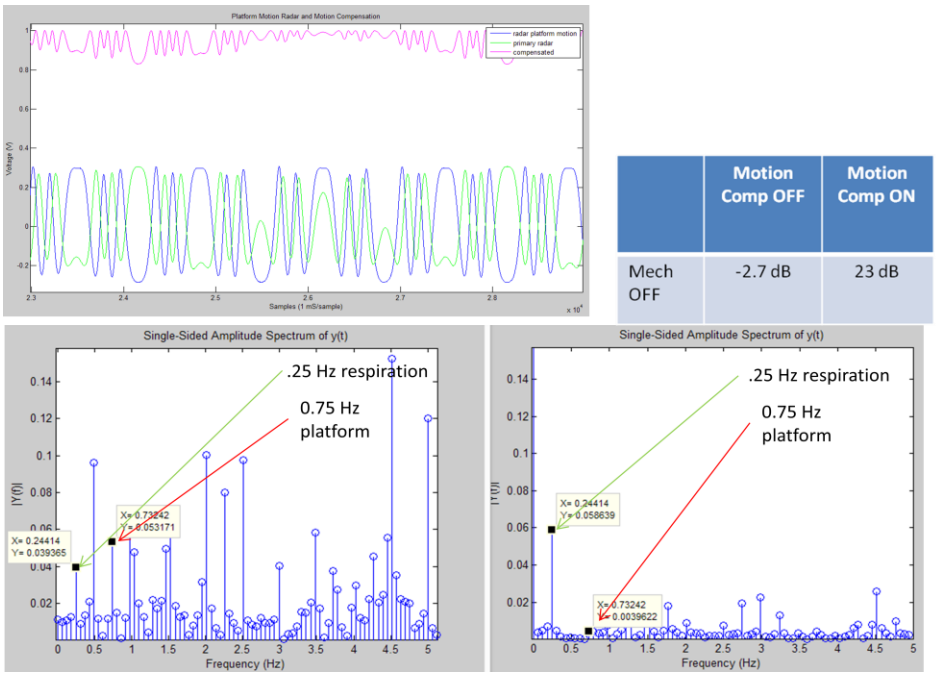

	Motion Comp OFF	Motion Comp ON
Mech OFF	-2.7 dB	23 dB

Motion Compensation OFF Motion Compensation ON

Figure 67. Motion Compensation Algorithm – Platform and Respiration Motion 33 mm, .75 Hz Platform/4.8 mm, .25 Hz Respiration

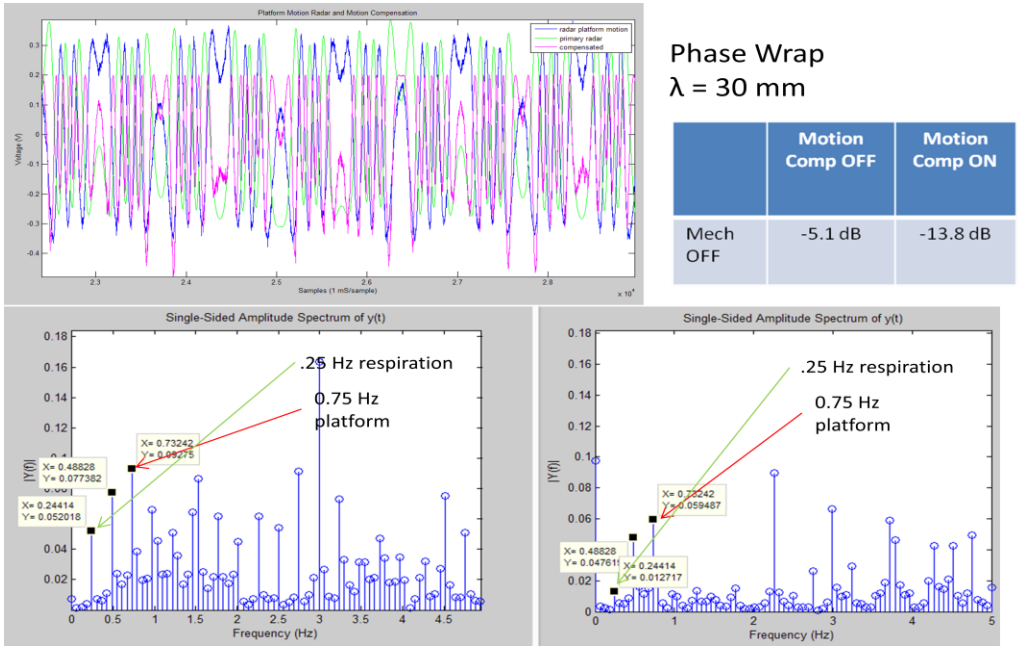

Phase Wrap
λ = 30 mm

	Motion Comp OFF	Motion Comp ON
Mech OFF	-5.1 dB	-13.8 dB

Motion Compensation OFF Motion Compensation ON

Figure 68. Motion Compensation Algorithm – Platform and Respiration Motion 38 mm, .75 Hz Platform/4.8 mm, .25 Hz Respiration with a significant amount of phase wrap occurring.

The test results for this parametric displacement test are summarized in Table 14 and Figure 69. The SIR improvements ranged from -9.9 dB to 33.5 dB. The effectiveness of the motion compensation algorithm is reduced as the platform motion displacement increases. When the platform motion magnitude at 38 mm exceeds the radar wavelength (wavelength = 30 mm at 10 GHz), the phase wrapping degrades the motion compensation to the point where the platform motion reduction is -8.7 dB.

For the displacement at 17 mm, the SIR improvement is not as pronounced because the uncompensated signal has SIR = 14.6 dB whereas the compensated signal has SIR = 4.7 dB. This appears to be a result of the constructive interference at this displacement, which is approximately one half wavelength (15 mm), that enhances the signal component even without motion compensation. Since the harmonic content is significant without motion compensation and suppressed with motion compensation, these additional spurs are included in the SIR calculation. See Figure 64.

Analysis of the results leads to the conclusion that platform stabilization is necessary for displacements exceeding a wavelength, where the platform stabilization reduces the displacement to less than a wavelength, so that the motion compensation algorithm can be effective.

Table 14. Motion Compensation SIR Performance

Platform Motion	Platform Displace-ment	Vital Sign Frequency	Respiration Displace-ment	Mechanical Compen-sation	Motion Compen-sation	Signal to Interference Ratio (SIR)	SIR Improve-ment
0.75 Hz	3 mm	.25 Hz	3 mm	Off	Off	0	
0.75 Hz	3 mm	.25 Hz	3 mm	Off	On	14.9	14.9
0.75 Hz	6 mm	.25 Hz	3 mm	Off	Off	-1.8	
0.75 Hz	6 mm	.25 Hz	3 mm	Off	On	8	9.8
0.75 Hz	12 mm	.25 Hz	3 mm	Off	Off	6	
0.75 Hz	12 mm	.25 Hz	3 mm	Off	On	11.5	5.5
0.75 Hz	17 mm	.25 Hz	3 mm	Off	Off	-4.6	
0.75 Hz	17 mm	.25 Hz	3 mm	Off	On	4.7	-9.9
0.75 Hz	23 mm	.25 Hz	3 mm	Off	Off	-27	
0.75 Hz	23 mm	.25 Hz	3 mm	Off	On	6.5	33.5
0.75 Hz	27 mm	.25 Hz	3 mm	Off	Off	3.5	
0.75 Hz	27 mm	.25 Hz	3 mm	Off	On	26	22.5
0.75 Hz	33 mm	.25 Hz	3 mm	Off	Off	-2.7	
0.75 Hz	33 mm	.25 Hz	3 mm	Off	On	23	25.7
0.75 Hz	38 mm	.25 Hz	4.8 mm	Off	Off	-5.1	
0.75 Hz	38 mm	.25 Hz	4.8 mm	Off	On	-13.8	-8.7

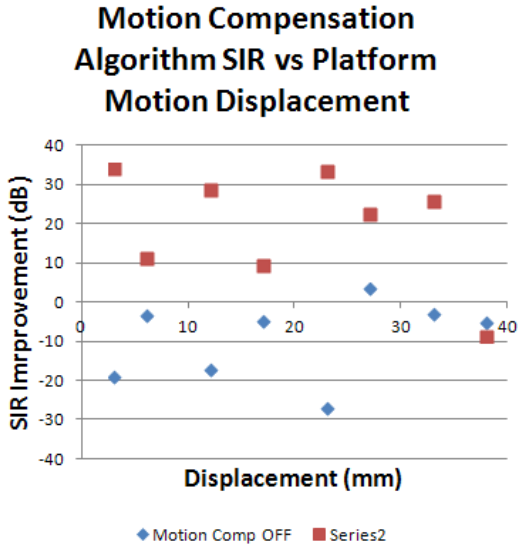

(a)

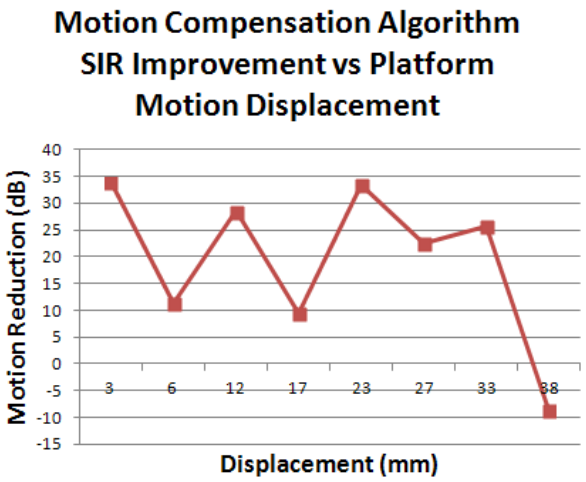

(b)

Figure 69. Motion compensation effectiveness as a function of platform displacement. (a) SIR before/after motion compensation (b) SIR improvement with motion compensation.

21.2.2 Motion Compensation Algorithm Performance for Various Platform Motion Frequencies and Waveforms

The following data plots show the motion compensation algorithm performance for recovering the respiration signal in the presence of platform motion. While the time domain waveforms are not fully recovered due to phase wrap, the frequency content is generally preserved, allowing the respiration rates to be recovered.

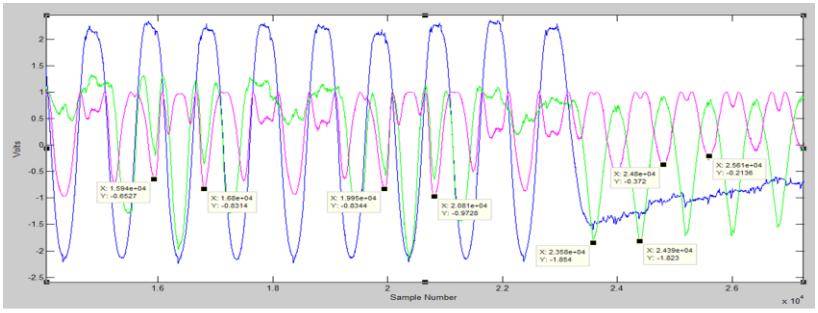

Blue = 1 Hz platform motion
Green (t > 24s) = 1.25 Hz respiration
Green (t < 24s) = composite platform and respiration motion
Magenta = phase compensated composite waveform

Figure 70. Motion compensation algorithm – Platform and respiration motion. Recorded waveform for superimposed platform motion (1 Hz blue), composite platform motion and respiration waveform (1.25 Hz green) and recovered waveform using motion compensation (magenta). For t >24 sec, the platform motion is stopped so that the composite waveform (green) is the respiration motion only.

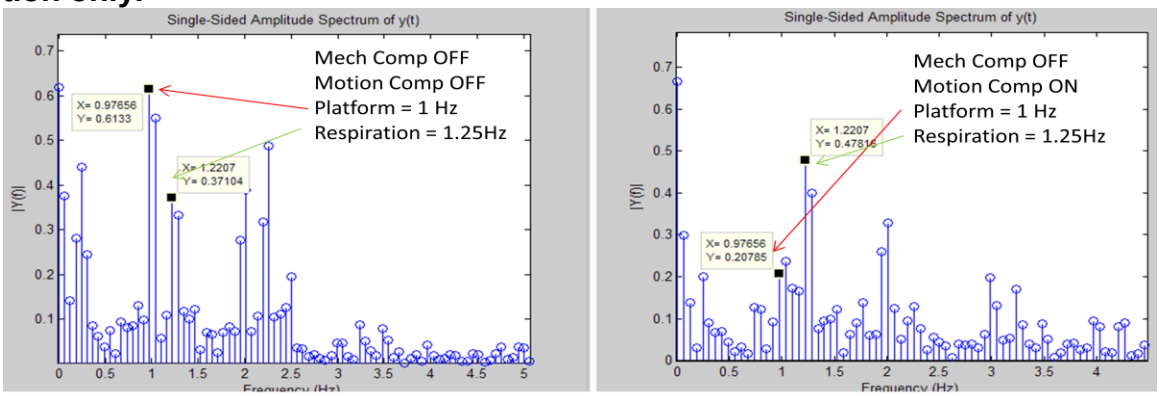

SIR = -4.3 dB

SIR = 7.3 dB

Figure 71. Motion compensation algorithm – Platform and respiration motion. Spectrum for composite motion waveform (a) without motion compensation (b) with motion compensation. SIR improvement is 11.6 dB.

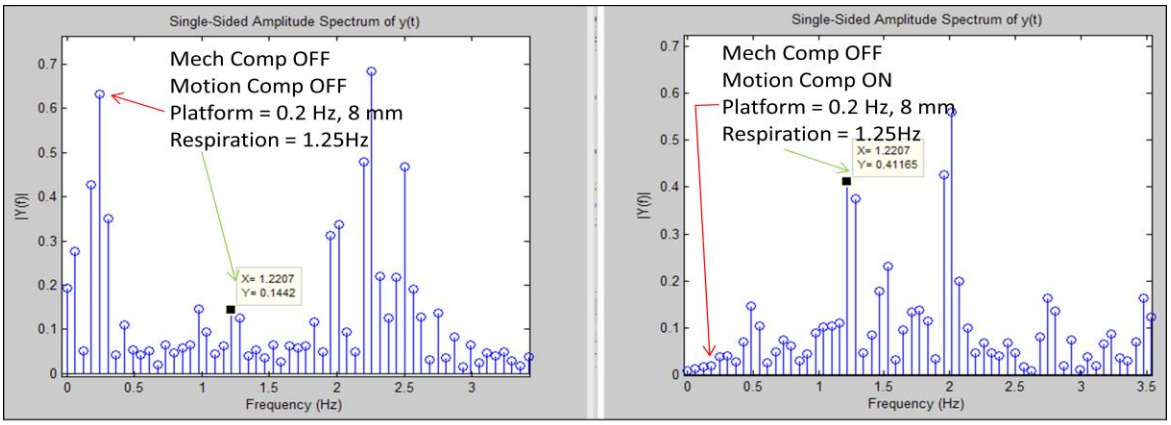

Figure 72. Motion compensation algorithm – Platform and respiration motion. Spectrum for composite motion waveform (a) without motion compensation (b) with motion compensation. SIR improvement is 27.5 dB.

21.2.3 Motion Compensation Algorithm Performance for Overlapping Frequencies

Phase compensation is superior to band pass filtering when the platform motion freq overlaps with the signal frequency. The advantage of the phase domain motion compensation is that, unlike traditional band pass filtering in the frequency domain, overlapping frequencies can be compensated in the phase domain without cancelling the signal of interest. This is shown in Figure 73 for the case where the platform motion and respiration signal are both at 1.25 Hz.

Since the motion compensation algorithm operates in the phase domain, the platform motion can be removed without affecting the respiration signal. This is a key differentiator from a traditional filter, where applying a stop band filter at the interference frequency would also filter out an overlapping signal frequency.

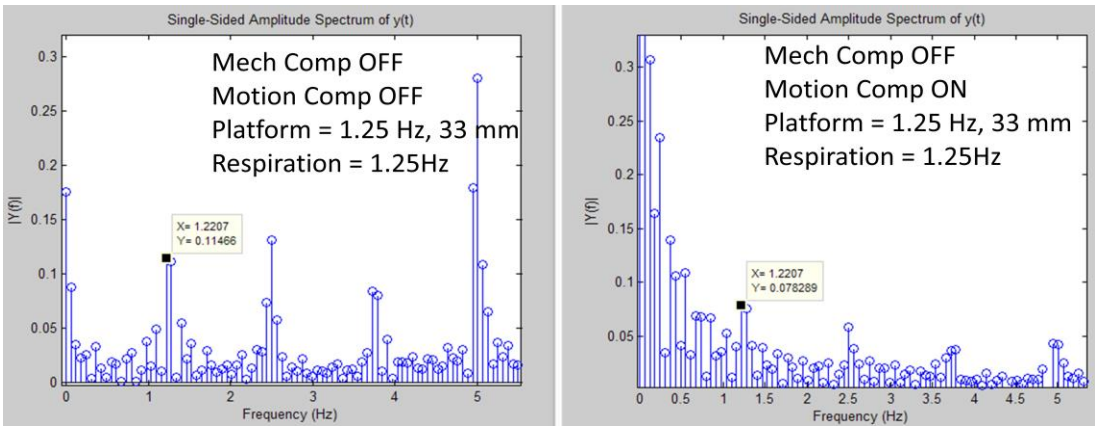

Figure 73. Motion compensation with overlapping platform motion and respiration frequency. Frequency spectrum with motion compensation off (left) and on (right) for overlapping platform and target frequencies (1.25 Hz). Harmonics are suppressed and lower frequency components are introduced.

21.2.4 Motion Compensation Performance with Non-sinusoidal Platform Motion

To test the case for non-sinusoidal platform motion, a trapezoidal and step waveform was used to introduce non-linearities in the platform motion. The effectiveness of the motion compensation is shown where the platform motion sideband peaks are suppressed in Figure 75 and Figure 77. The single tone interference SIR is not computed, because unlike the previous sinusoidal platform motion tests, the trapezoidal and step waveforms have many sideband interference tones. These sideband tones are strongly suppressed by the motion compensation algorithm and would result in a significant SNR improvement when considering the receiver pass band bandwidth.

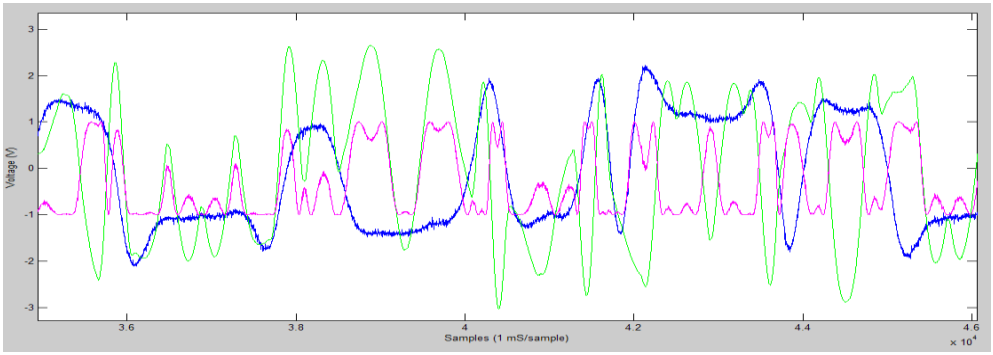

Figure 74. Motion compensation with trapezoidal waveform platform motion. Trapezoidal platform motion (23 mm peak-to-peak), respiration motion (10 mm at 1.25 Hz) and composite waveform showing the effect of motion compensation without mechanical stabilization.

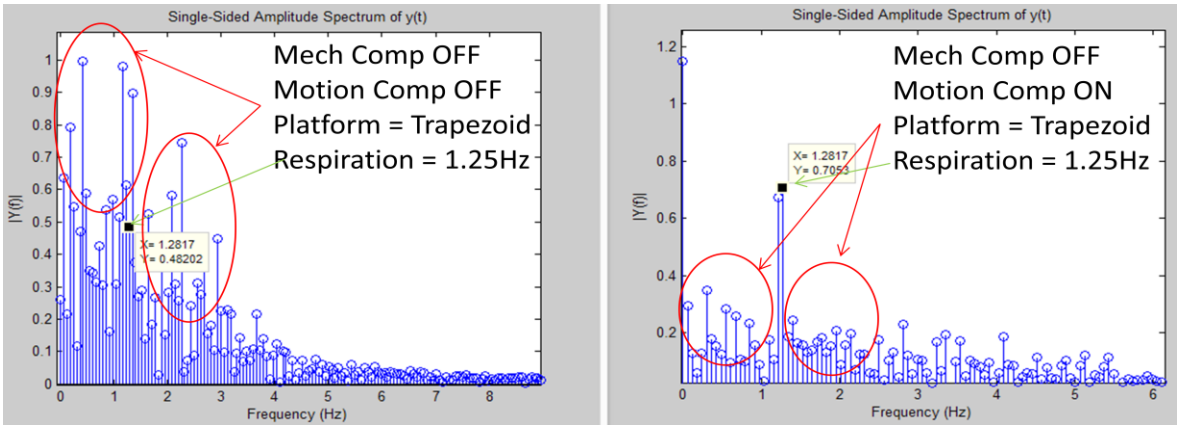

Figure 75. Motion compensation with trapezoidal platform motion. Spectrum showing harmonic content of trapezoidal waveform and motion compensation suppression of harmonics.

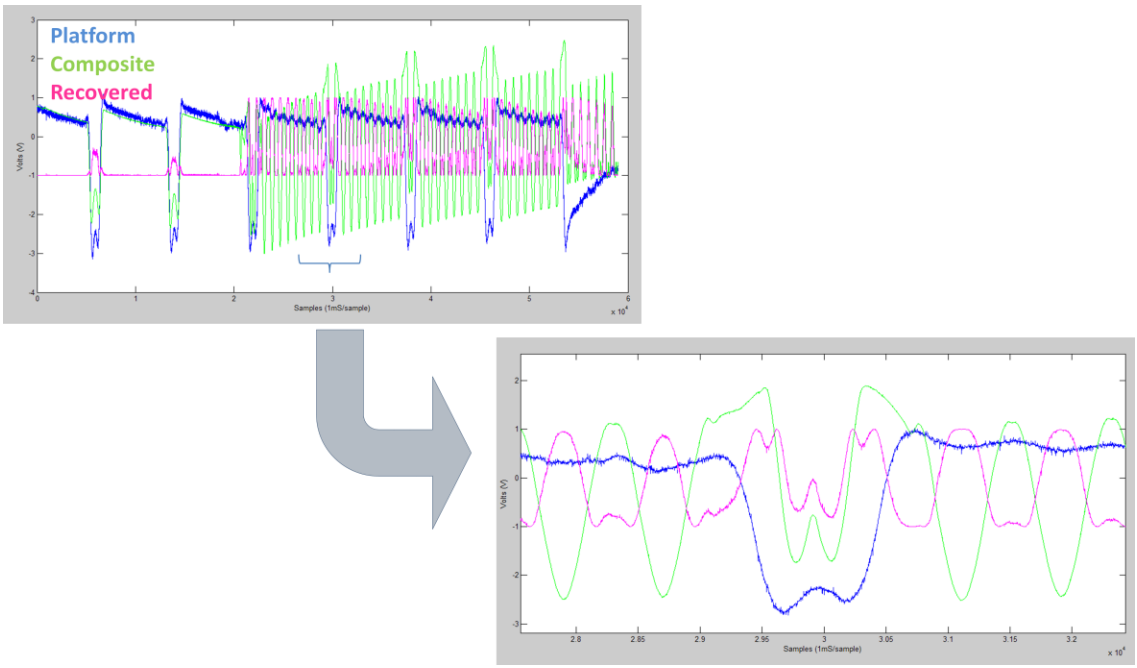

Figure 76. Step platform motion, respiration motion, composite waveform showing the effect of motion compensation without mechanical stabilization. Upper plot spans 6 sec; lower plot zoomed in to 0.5 sec span.

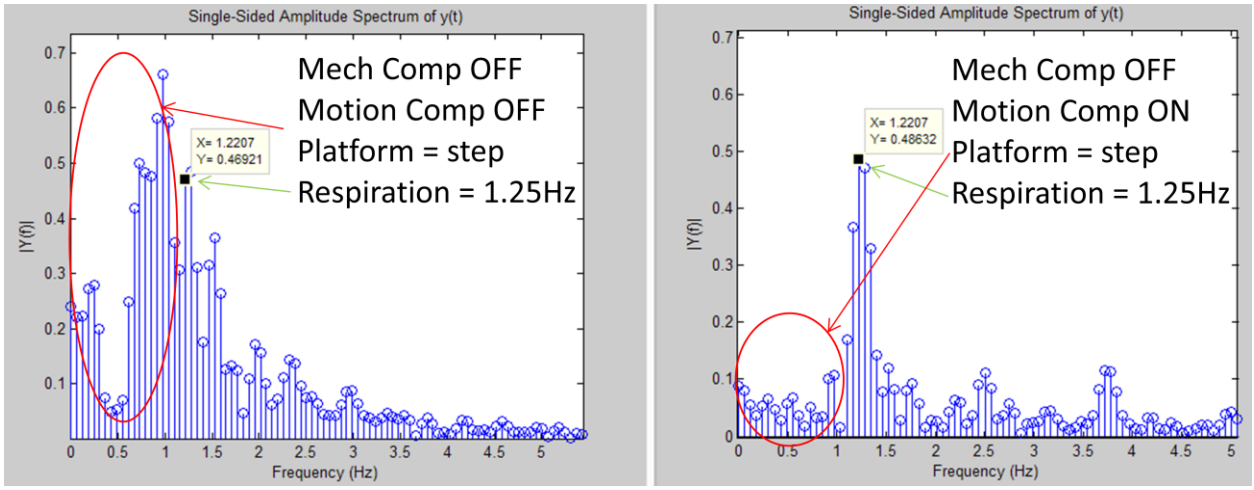

Figure 77. Step platform motion and 1.25 Hz respiration motion, composite spectrum without mechanical stabilization.

21.3 Platform Stabilization

Platform stabilization uses a mechanical actuator to move the radar sensor in anti-phase and at the same speed and magnitude with the underlying platform motion. The sub-platform stabilization actuator motion is driven by a secondary sensor that provides an input to a feedback loop that cancels the underlying platform motion. The platform stabilization was tested with either an ultrasonic sensor or with a secondary radar sensor pointed at a reflector (simulating the ground or ceiling). To isolate the effectiveness of the platform stabilization, the mechanical compensation was tested next without the baseband motion compensation algorithm. The graphs below are notated with mechanical motion ON/OFF to indicate whether platform stabilization is enabled/disabled.

21.3.1 Ultrasonic Sensor Platform Stabilization

An ultrasonic sensor was used to detect the platform motion and provide an error signal for motion compensation. Ultrasonic sensors operate by emitting high frequency pulses in the 40 KHz range that are then reflected by a target. After reflecting off the target, the echo is then received by the sensor and the time difference is measured. The distance to the target can be calculated by measuring the Time of Flight (ToF) and using the speed of sound.

The ultrasonic sensor is used to provide a range error signal to a feedback control loop that drives a belt driven slide potentiometer actuator. The feedback loop is executed by an Arduino UNO and Motor Shield that provides up to 2A of current at 10V to drive the slide potentiometer.

The Arduino code reads the output from the ultrasonic sensor and moves the motion compensation actuator relative to the difference between the received distance value and a reference distance value. A radar module was also mounted on the compensated platform and pointed at a respiration phantom. See test bed photo in Figure 52 and the experiment configuration and signal flow diagram in Figure 78.

A PID (Proportional, Integral, Derivative) stage was also implemented in the feedback algorithm.. The PID parameters allows for tuning of the feedback response to optimize the motion compensation. The optimal PID values were empirically derived as P = 68, I = 7.6 and D = 73. We also modeled the system transfer function using the Matlab System ID Toolbox to reduce the number of PID empirical permutations.

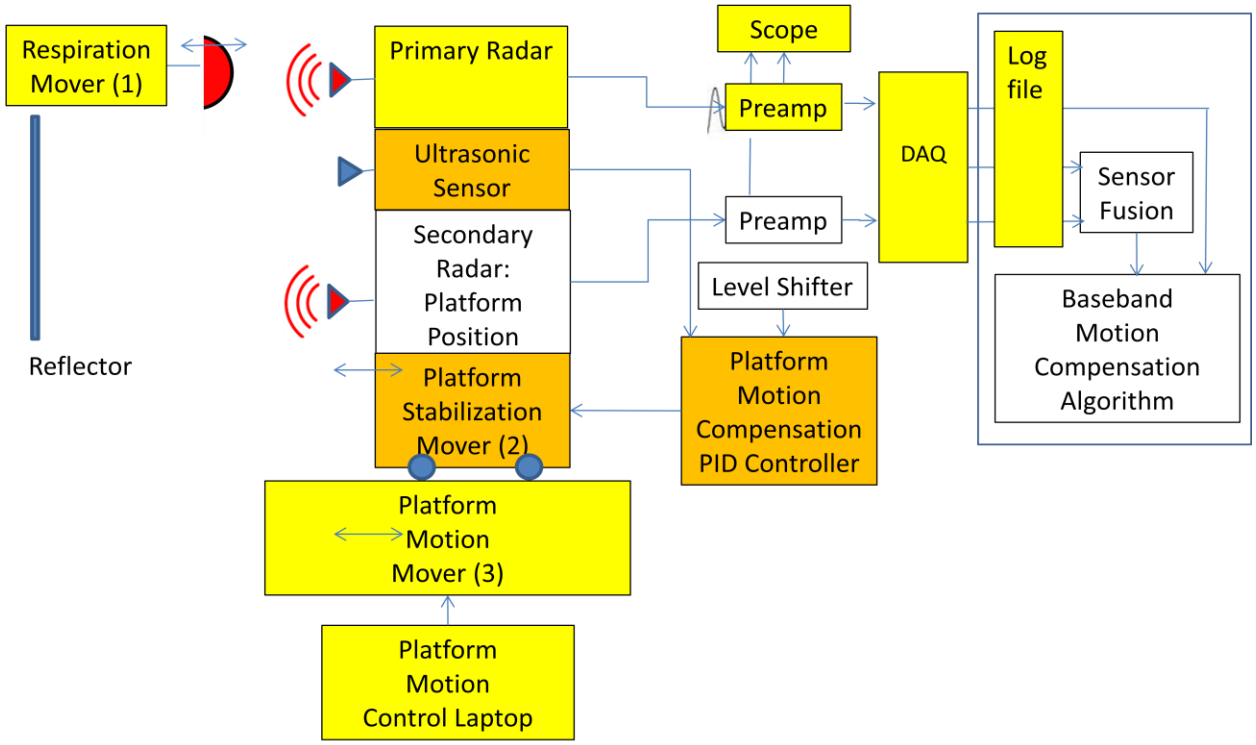

Figure 78. Platform stabilization using an ultrasonic sensor. Components used for the experiment are highlighted.

With the platform stabilization enabled, the platform motion was reduced from 46 mm to 11mm peak-to-peak for a 76% reduction in unwanted motion as shown in Figure 79. This result was based on a constant gain feedback signal. After tuning the PID loop, we were able to reduce the compensated peak-to-peak motion to 6 mm for a 86% reduction in unwanted motion.

We also attempted to improve the compensation response with a position dependent gain factor, where the gain was proportional to the error voltage, resulting in faster

convergence of the motion compensation. The result was not as significant as the PID result and was abandoned.

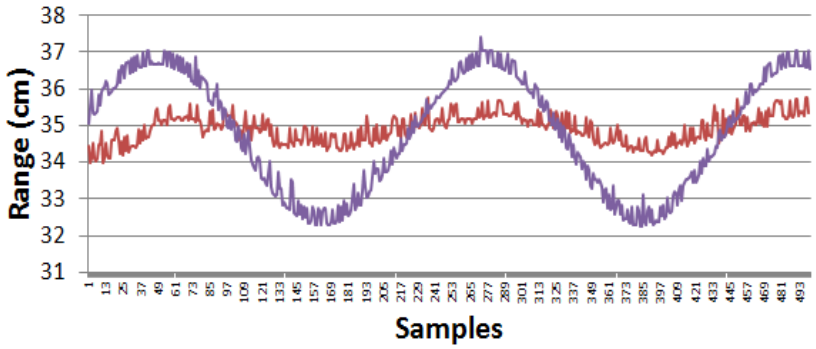

Figure 79. Platform motion reduction with ultrasonic sensor platform stabilization. Platform motion with 4.6 cm peak-to-peak sinusoidal waveform and 1.1 cm peak-to-peak compensated motion for a 76% reduction in unwanted platform motion amplitude using the constant gain feedback loop.

To assess the motion compensation system performance, we plotted the spectrum of the respiration signal alone, the platform motion spectrum and the platform stabilized simultaneous respiration and platform motion spectrum in Figure 80 . The spectra were obtained by performing a FFT in MatLab from the baseband radar signal. As shown in Figure 80 (a), the respiration signal is masked by the platform motion noise. In Figure 80 (c), the respiration signal is recovered after motion compensation is enabled.
The SNR for each case shown in Figure 80 is summarized in Table 15.

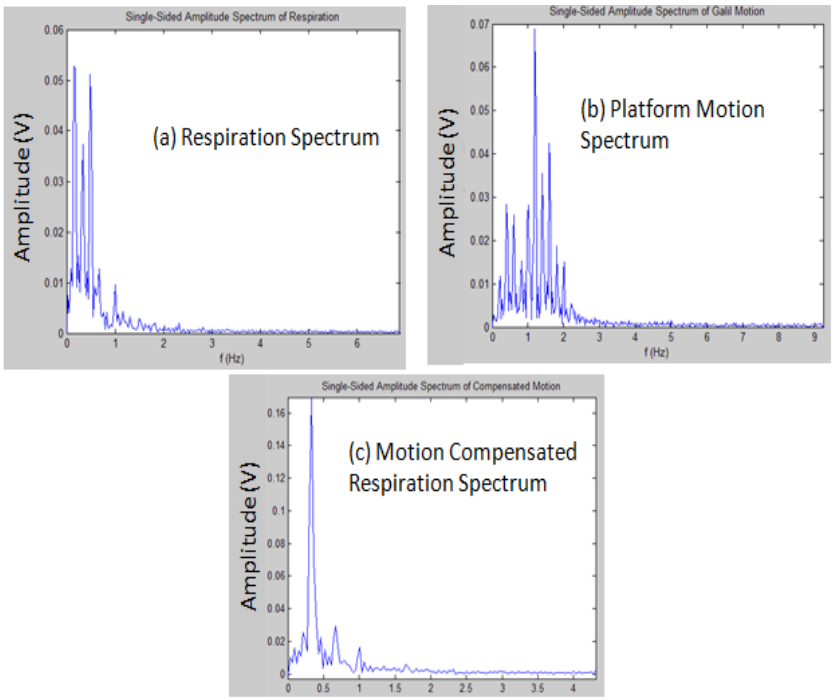

Figure 80. Platform stabilization with ultrasonic sensor. Baseband radar spectra for (a) respiration signal at 0.4 Hz, (b) platform motion at 1.1 Hz and (c) both respiration and platform motion with motion compensation enabled.

Table 15. SNR before and after ultrasonic sensor platform stabilization.

	voltage amplitude (V)		**power amplitude (V^2)**		**SIR (dB)**
	respiration motion	Platform motion	respiration motion	Platform motion	10 log(resp^2 /plat^2)
No compensation	0.028	0.07	0.0008	0.0049	-8.0
Ultrasonic Platform Stabilization	0.17	0.015	0.0289	0.0002	21.1
SIR improvement					29.1

21.3.2 Radar Sensor Platform Stabilization

A secondary radar (the primary radar is the vital signs radar) was also used as an alternative to the ultrasonic sensor for platform stabilization. This radar was attached to a boom and pointed away from the respiration target reflector to minimize cross-talk between the primary respiration radar. The fact that the secondary radar was pointed to a stationary reflector in the opposite direction is immaterial as the range motion is in anti-phase to the platform motion, i.e., when the platform is approaching the respiration reflector, the platform is receding from the reference reflector at the same frequency and amplitude as the primary radar. This orientation would also be relevant for an indoor drone scenario where the ceiling would function as the stationary reference to measure the platform motion. The experiment configuration and signal flow diagram for this experiment is shown in Figure 81.

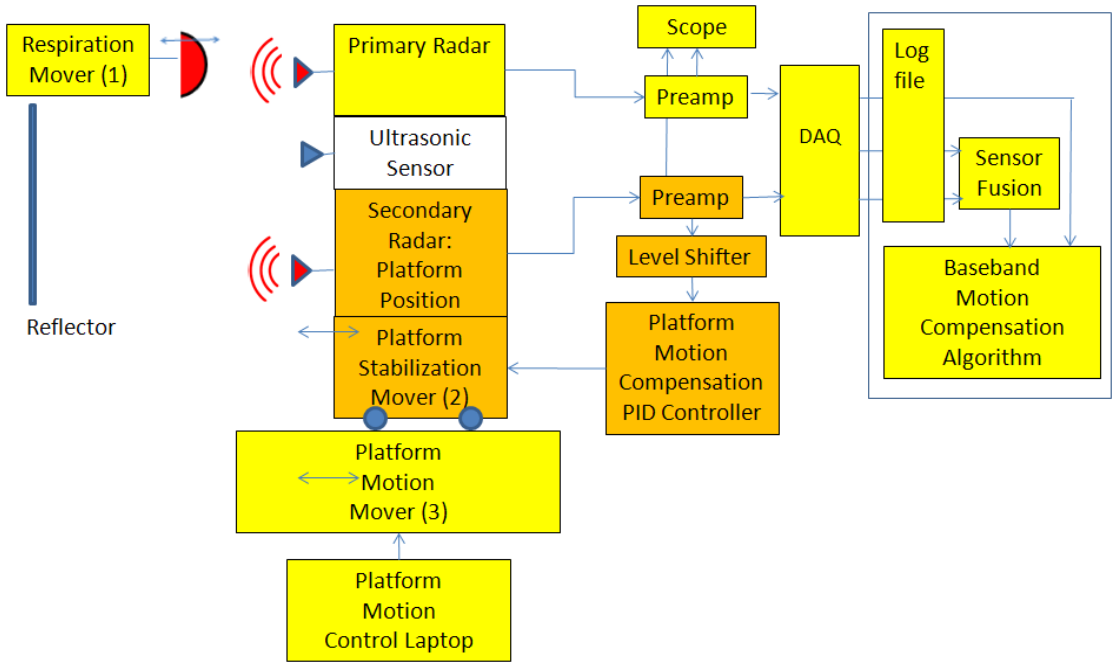

Figure 81. Platform stabilization using the secondary radar sensor. Components used for the experiment are highlighted.

The effectiveness of the platform stabilization with the secondary radar sensor is shown in Figure 82. The 18 mm of platform motion is suppressed by 6 dB. In Figure 83, 5 mm of platform motion is suppressed by 10 dB.

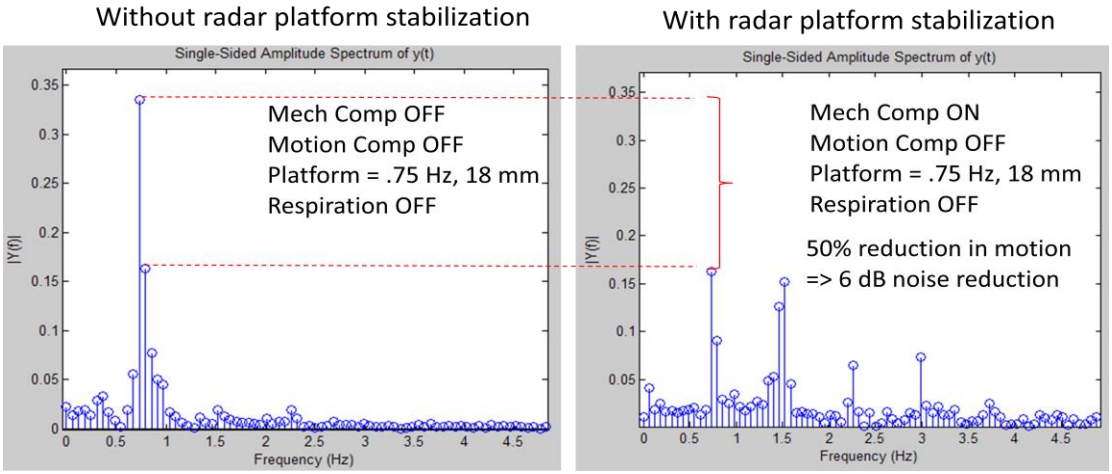

Figure 82. Radar sensor platform stabilization.
Platform stabilization where 0.75 Hz platform motion with 18 mm displacement is reduced 6 dB with secondary radar sensor used for mechanical motion compensation.

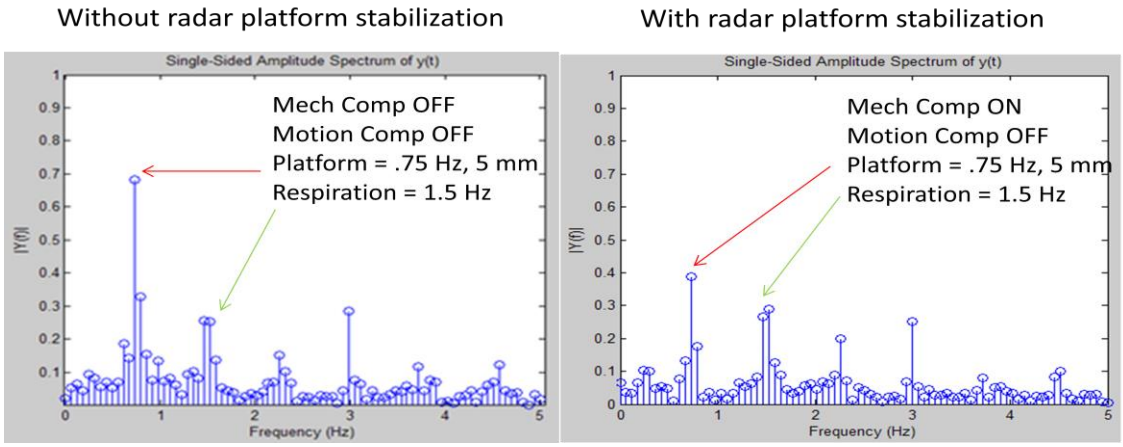

Radar Platform Stabilization OFF	RadarPlatform Stabilization ON
-12.6 dB	-2.5 dB

Figure 83. Radar sensor platform stabilization.
.75 Hz platform motion with 5 mm displacement is reduced by 10.1 dB with secondary radar sensor used for mechanical motion compensation.

21.4 Combined Platform Motion Compensation and Platform Stabilization

Next, both the motion compensation algorithm and platform stabilization are tested simultaneously. To facilitate data logging, a single data log file was created for sequential combinations of platform motion, composite motion (platform + respiration), platform stabilization and respiration motion. The sequence is summarized in

Table 16. Test sequence combinations for platform motion, respiration motion and platform stabilization data collection.

Table 16. Test sequence combinations for platform motion, respiration motion and platform stabilization data collection.

Respiration Radar Output	Platform Mover	Respiration Mover	Ultrasonic Motion Compensation	Platform Position Radar	Vital Signs Radar
UAV Platform Position readout	On	Off	Off	On	On
Composite Motion (Platform + Respiration)	On	On	Off	On	On
Mechanical Motion Compensation (Platform + Respiration)	On	On	On	On	On
Respiration Mover	Off	On	Off	On	On

The following data plots show the combined effect of platform motion compensation and platform stabilization using either the ultrasonic sensor or the secondary radar sensor.

In Figure 84. Ultrasonic sensor platform stabilization and motion compensation algorithm performance for 33 mm/.2 Hz platform motion and 5 mm/1.25 Hz respiration., the ultrasonic platform stabilization increases the SIR by 24.1 dB (13 dB + 11.1 dB) while the motion compensation algorithm increases the SIR by 42 dB (13 dB + 29 dB). However, when the ultrasonic platform stabilization is combined with the motion compensation signal processing, the SIR improvement is 15.1 dB (-13 dB + 2.1 dB).

This is because the platform motion interference component is affected by the imperfect cancellation of the platform stabilization that contributes low frequency components in the vicinity of 0.2 Hz.

As the platform motion displacement is increased to beyond a wavelength, the phase wrapping introduces higher frequency components. This is evident in the figure below and the motion compensation algorithm becomes less effective.

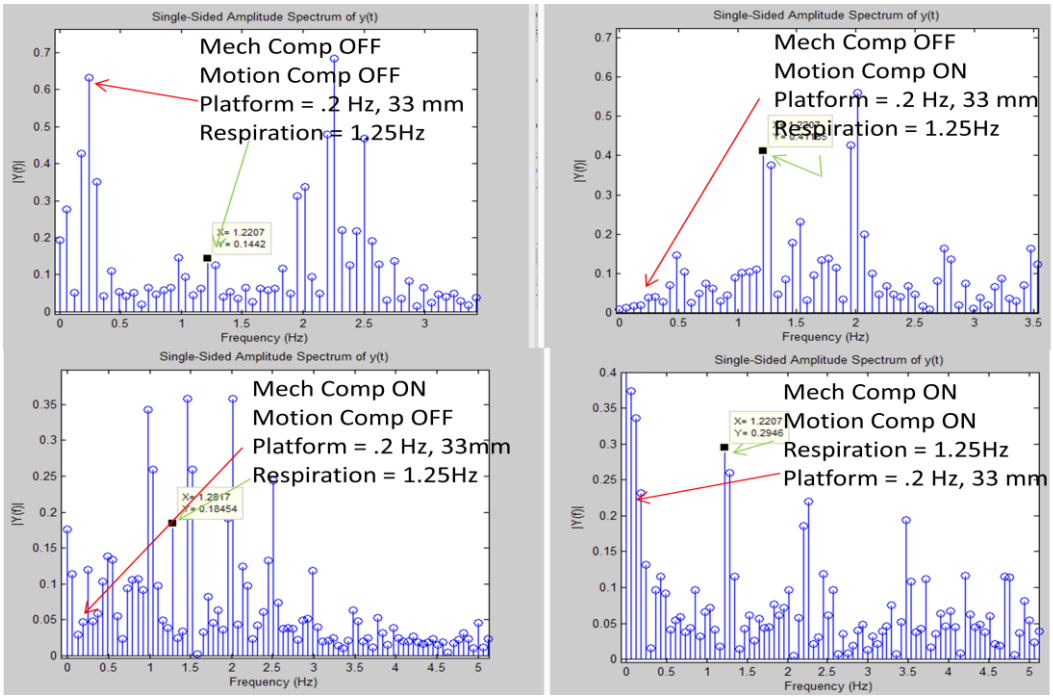

	Motion Comp OFF	Motion Comp ON
Ultrasonic Stabilization OFF	-13	29dB
Ultrasonic Stabilization ON	11.1 dB	2.1 dB

Figure 84. Ultrasonic sensor platform stabilization and motion compensation algorithm performance for 33 mm/.2 Hz platform motion and 5 mm/1.25 Hz respiration.

The effectiveness of the motion compensation in eliminating the platform stabilization noise introduced by the ultrasonic sensor driven stabilzation cart is shown in Figure 85. The feedback loop for the cart had a slight lag and instabilities that introduced mechanical jitter, resulting in the generation of harmonics evident in the spectrum. The baseband motion compensation was able to improve the SIR by 12.3 dB at the 1.25 Hz respiration frequency. Not included in the SIR is the suppression of the spurious platform noise introduced by the mechanical stabilization feedback loop so the effective SNR improvement would be even greater since the receiver passband would include the harmonics. See Figure 85.

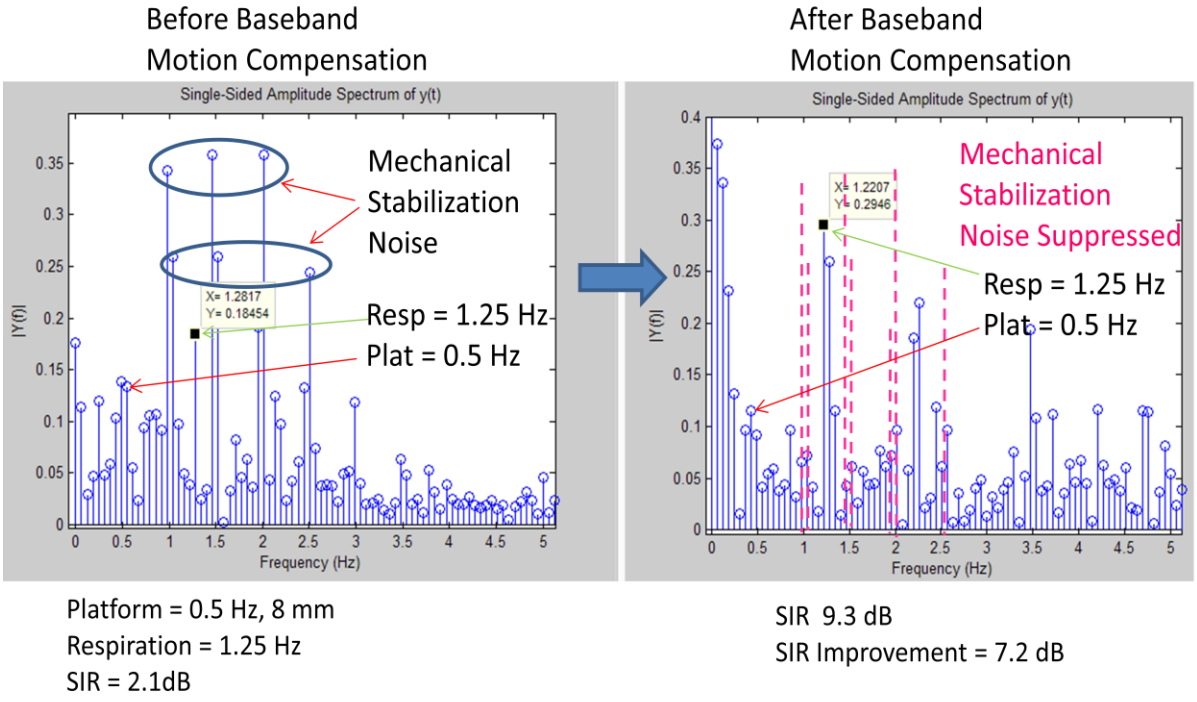

Figure 85. Motion compensation harmonic suppression.
Platform stabilization using an ultrasonic sensor introduces harmonics that are suppressed by the motion compensation algorithm. Respiration signal is also enhanced by the algorithm.

For the following test case, the target signal frequency was increased to 1.5 Hz or the equivalent of a 90 beat per minute heart rate with 5 mm displacement. The platform motion was at 0.75 Hz also with a 5 mm displacement.

The radar platform stabilization and motion compensation improved the SIR in all cases. The radar platform stabilization improved the SIR by 10.1 dB (-12.6 dB vs – 2.5 dB) with motion compensation disabled. Motion compensation improved both cases where the radar stabilization was disabled and enabled.

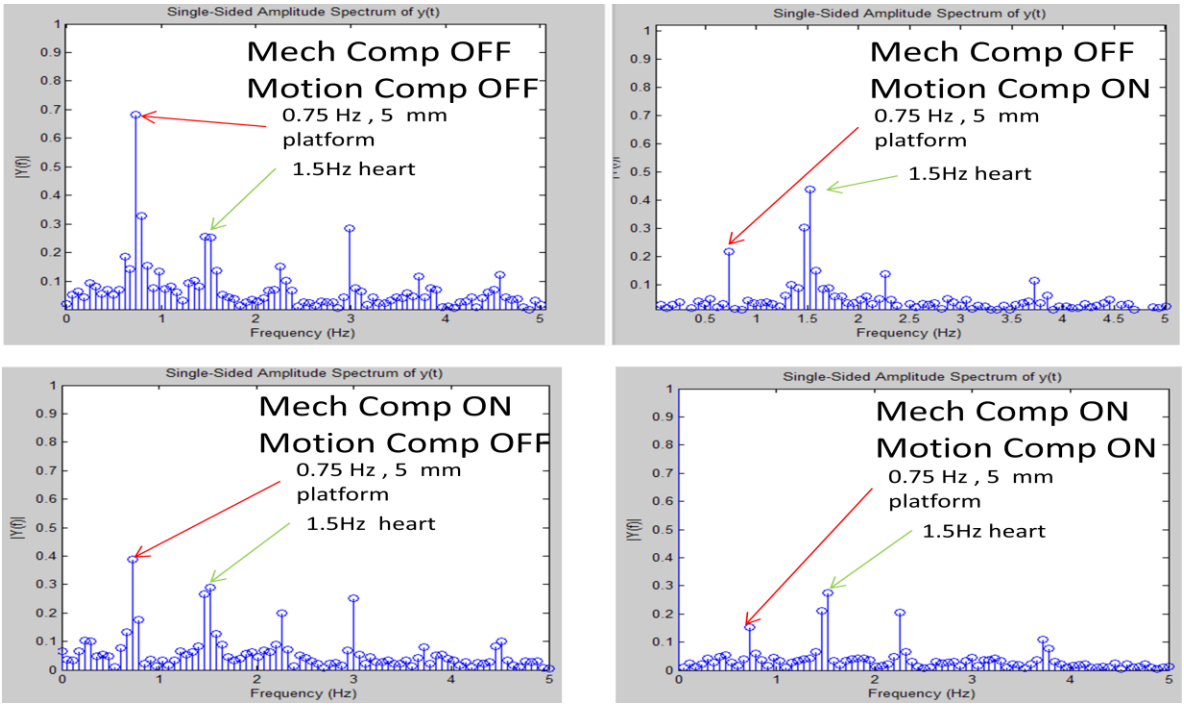

	Motion Comp OFF	Motion Comp ON
Radar Stabilization OFF	-12.6 dB	11.7 dB
Radar Stabilization ON	-2.5 dB	+5.1 dB

Figure 86. Radar platform stabilization and motion compensation performance. Platform motion with 0.75 Hz, 5 mm displacement and 1.5 Hz, 5 mm peak to peak respiration signal.

For the following test case, the target signal frequency was reduced to 0.25 Hz or the equivalent of 15 breaths per minute respiration rate with 5 mm displacement. The platform motion was at 1.25 Hz also with a 18 mm displacement.

The radar platform stabilization decreased the SIR by 3.2 dB. The decrease in SIR is attributable to the feedback loop latency and a slight mismatch in the sub-platform cart speed, leading to an imperfect cancellation of platform motion. Applying the motion compensation algorithm to both cases, with and without platform stabilization, recovered the signal with a positive SIR.

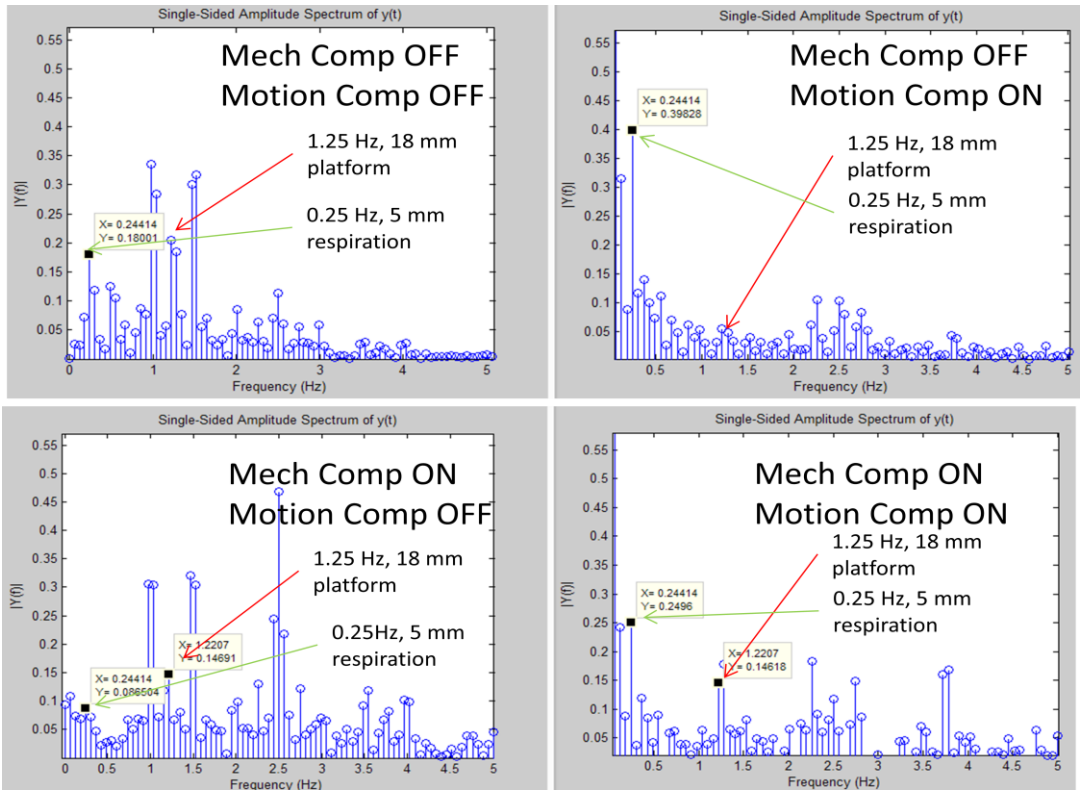

	Motion Comp OFF	Motion Comp ON
Radar Stabilization OFF	**-1.3 dB**	**18 dB**
Radar Stabilization ON	**-4.5 dB**	**4.6 dB**

Figure 87. Radar platform stabilization and motion compensation performance. Platform motion with 1.25 Hz, 18 mm displacement and .25 Hz, 5 mm peak to peak respiration signal.

21.5 Comparison with Alternative Filtering Techniques

21.5.1 FIR Filter

As a comparison, a conventional digital band pass filter was also applied to the data for 1 Hz platform motion with 1.25 Hz respiration motion. See Figure 88. The pass band was between 1.25 Hz to 1.5 Hz. The FIR filter SIR was 13.6 dB compared to 7.4 dB for the motion compensation algorithm. Although the SIR performance is better for the filter, the filter pass band must be known apriori and would not have the same performance over a wider range of respiration rates.

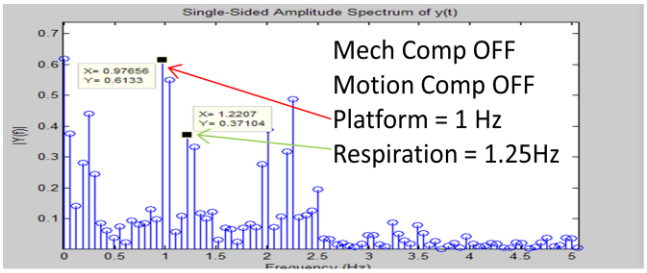

SIR = -4.3 dB

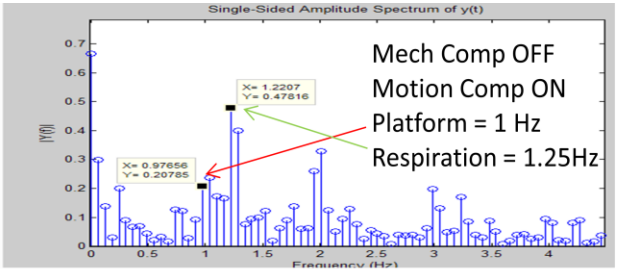

SIR = 7.4 dB

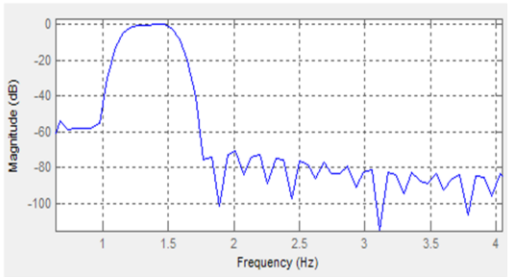

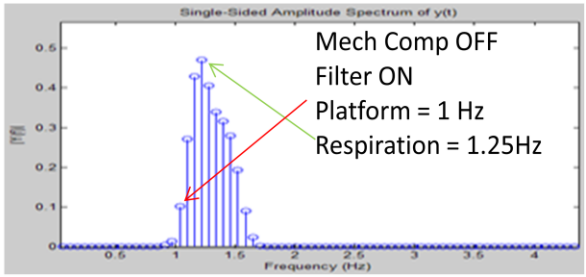

SIR = 13.6 dB

```
Fstop1 = 1;           % First Stopband Frequency
Fpass1 = 1.25;        % First Passband Frequency
Fpass2 = 1.5;         % Second Passband Frequency
Fstop2 = 1.75;        % Second Stopband Frequency
Dstop1 = 0.001;       % First Stopband Attenuation
Dpass  = 0.057501127785;  % Passband Ripple
Dstop2 = 0.0001;      % Second Stopband Attenuation
```

Figure 88. FIR filter with 1.25 Hz to 1.5 Hz passband filter applied to 1 Hz platform, 1.25 Hz respiration signal.

21.5.2 Adaptive LMS Filter

An adaptive filter approach was also implemented to compare with the phase compensation algorithm. An adaptive filter sets its filter coefficients iteratively based on the error signal e(k) that's generated from the desired signal d(k) minus the current adaptive filter output y(k). See Figure 89. The noise component, n(k), is assumed to be correlated such that it can be removed from the composite signal s(k) + n(k).

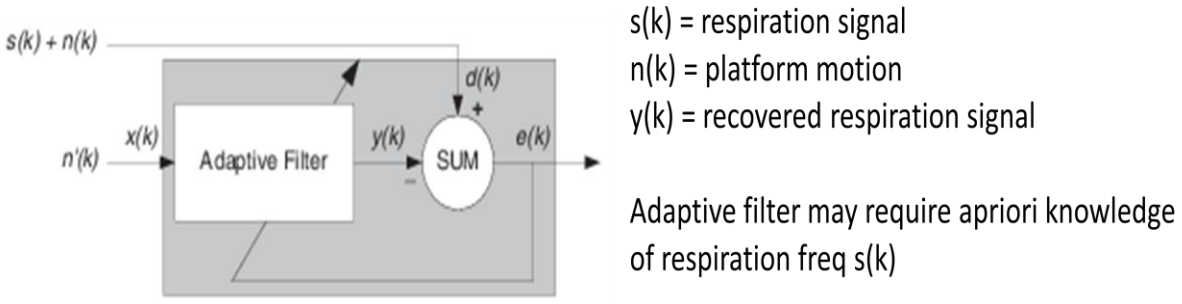

Figure 89. Adaptive LMS filter topology. See MATLAB code in the appendix.

In Figure 90, we processed s(k) = 1.25 Hz and n(k) = 1 Hz with the recovered signal shown in the bottom right plot. The adaptive filter performed slightly better than the phase compensation algorithm. However, adaptive filters may require apriori knowledge of the signal frequency if the signal and interferer are narrowband signals, as is the case here [24].

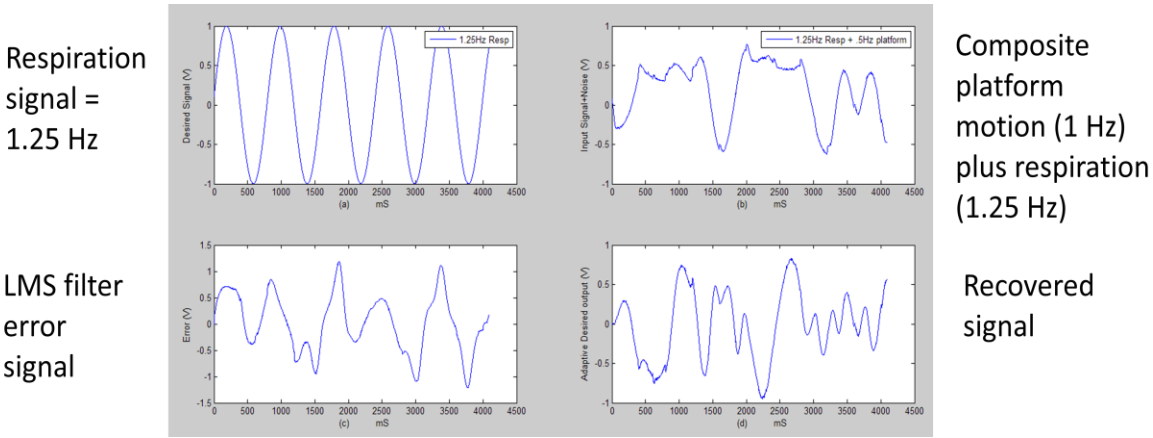

Figure 90. Adaptive LMS filter simulation.
1.25 Hz respiration signal and 1 Hz platform motion signal with resulting error signal and recovered signal.

In the following test case, the same data that was processed earlier with the motion compensation algorithm was processed with an adaptive LMS filter. The motion compensation algorithm SIR was 2.8 dB higher than the adaptive filter.

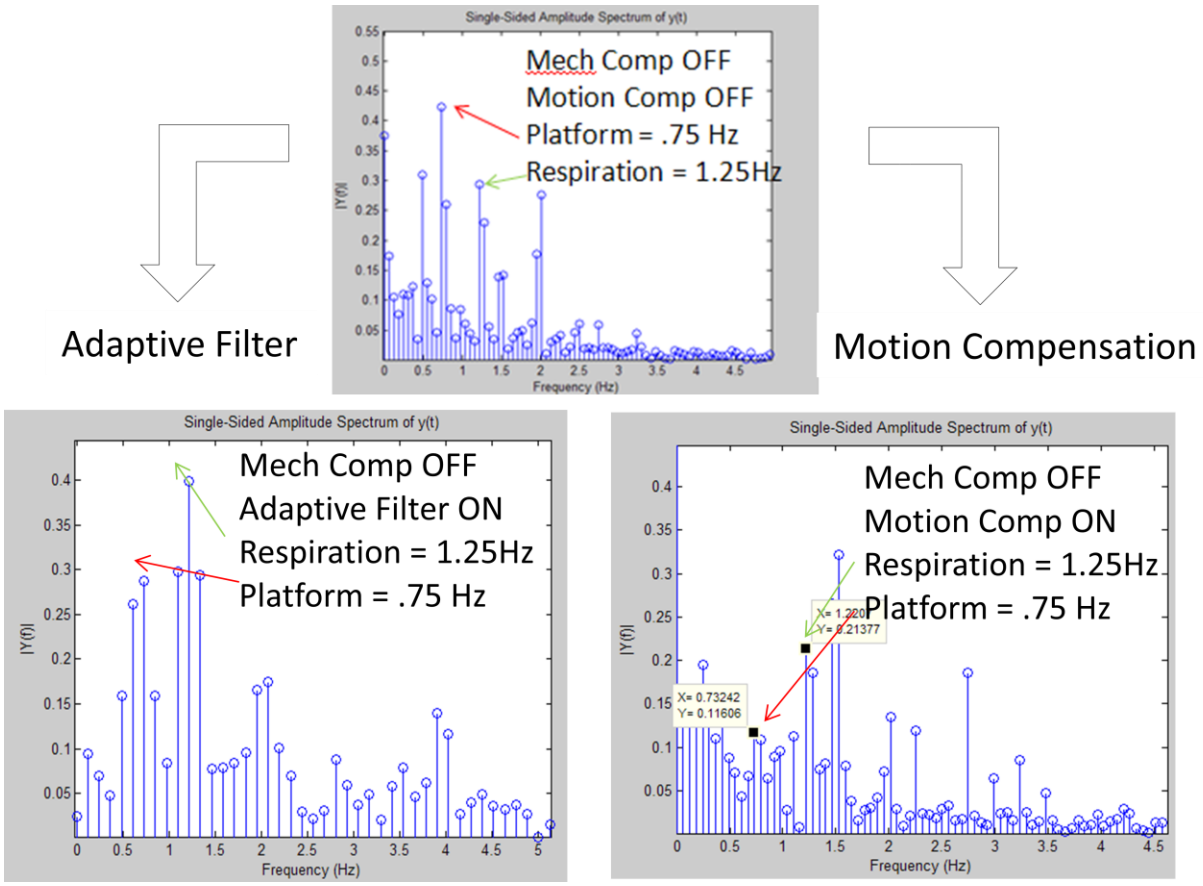

	Adaptive Filter	Motion Compensation
Signal to Interference Ratio	2.8 dB	5.6 dB

Figure 91. Motion compensation algorithm and adaptive filter performance comparison.

22.0 In-Range Motion Compensation and Platform Stabilization Data Summary and Analysis

A total of 71 test cases were analyzed to evaluate the platform stabilization and motion compensation algorithm. These are summarized in Table 13 and the scatter plots that follow.

Table 17. Data Summary

Platform Motion	Platform Displace-ment	Vital Sign Frequency	Respiration Displace-ment	Mechanical Compensation	Motion Compensation	Signal to Interference Ratio (SIR)
1 Hz	6 mm	1.25 Hz	10 mm	Off	Off	-3.4
1 Hz	6 mm	1.25 Hz	10 mm	Off	On	7.3
1 Hz	6 mm	1.25 Hz	10 mm	Off	filtered	15.3
1 Hz	6 mm	1.25 Hz	10 mm	Off	LMS adaptive	2.8
0.75 Hz	5 mm	1.25 Hz	10 mm	Off	Off	-3.4
0.75 Hz	5 mm	1.25 Hz	10 mm	Off	On	3.1
0.75 Hz	5 mm	1.25 Hz	10 mm	On (radar)	Off	-3.25
0.75 Hz	5 mm	1.25 Hz	10 mm	On (radar)	On	4.8
.2 Hz	8 mm	1.25 Hz	10 mm	Off	Off	-1.3
.2 Hz	8 mm	1.25 Hz	10 mm	Off	On	26
Trapezoidal	23 mm	1.25 Hz	10 mm	Off	Off	-14.2
Trapezoidal	23 mm	1.25 Hz	10 mm	Off	On	1.4
Step	10 mm	1.25 Hz	10 mm	Off	Off	-11.8
Step	10 mm	1.25 Hz	10 mm	Off	On	3.7
.5 Hz	8 mm	1.25 Hz	10 mm	Off	Off	-13
.5 Hz	8 mm	1.25 Hz	10 mm	On (ultra)	Off	2.1
.5 Hz	8 mm	1.25 Hz	10 mm	On (ultra)	On	7.6
.2 Hz	8 mm	1.25 Hz	10 mm	Off	Off	-13
.2 Hz	8 mm	1.25 Hz	10 mm	Off	On	29
.2 Hz	8 mm	1.25 Hz	10 mm	On (ultra)	Off	11.1
.2 Hz	8 mm	1.25 Hz	10 mm	On (ultra)	On	2.1
1.25 Hz	8 mm	1.25 Hz	10 mm	Off	Off	NA
1.25 Hz	8 mm	1.25 Hz	10 mm	Off	On	NA

Table 18. Data Summary (continued)

Platform Motion	Platform Displace-ment	Vital Sign Frequency	Respiration Displacement	Mechanical Compensation	Motion Compensation	Signal to Interference Ratio (SIR)
.75 Hz	5 mm	0 Hz	10 mm	Off	Off	6
.75 Hz	5 mm	0 Hz	10 mm	Off	On	24
.75 Hz	5 mm	0 Hz	10 mm	On (radar)	Off	3
.75 Hz	5 mm	0 Hz	10 mm	On (radar)	On	9.8
.75 Hz	5 mm	1.25 Hz	10 mm	Off	Off	-3.4
.75 Hz	5 mm	1.25 Hz	10 mm	Off	On	3.1
.75 Hz	5 mm	1.25 Hz	10 mm	On (ultra)	Off	-3.25
.75 Hz	5 mm	1.25 Hz	10 mm	On	On	4.8
.75 Hz	5 mm	.3 Hz	10 mm	Off	Off	-6
.75 Hz	5 mm	.3 Hz	10 mm	Off	On	4.3
.75 Hz	5 mm	.3 Hz	10 mm	On (radar)	Off	-12.6
.75 Hz	5 mm	.3 Hz	10 mm	On (radar)	On	11.7
.75 Hz	5 mm	1.5 Hz	5 mm	Off	Off	-12.6
.75 Hz	5 mm	1.5 Hz	5 mm	Off	On	11.7
.75 Hz	5 mm	1.5 Hz	5 mm	On (radar)	Off	-2.5
.75 Hz	5 mm	1.5 Hz	5 mm	On (radar)	On	5.1
1.25 Hz	18 mm	.25 Hz	5 mm	Off	Off	-1.3
1.25 Hz	18 mm	.25 Hz	5 mm	Off	On	18.0
1.25 Hz	18 mm	.25 Hz	5 mm	On (radar)	Off	-4.5
1.25 Hz	18 mm	.25 Hz	5 mm	On (radar)	On	4.6
.25 Hz	6 mm	.25 Hz	5 mm	Off	Off	-1.7
.25 Hz	6 mm	.25 Hz	5 mm	Off	On	16.8
.25 Hz	6 mm	.25 Hz	5 mm	On (ultra)	Off	-1.5
.25 Hz	6 mm	.25 Hz	5 mm	On (ultra)	On	18.7
.25 Hz	17 mm	.25 Hz	5 mm	Off	Off	-4.8
.25 Hz	17 mm	.25 Hz	5 mm	Off	On	15.0
.25 Hz	17 mm	.25 Hz	5 mm	On (ultra)	Off	-1.2
.25 Hz	17 mm	.25 Hz	5 mm	On (ultra)	On	15.5
.25 Hz	27 mm	.25 Hz	5 mm	Off	Off	3.5
.25 Hz	27 mm	.25 Hz	5 mm	Off	On	2.4
.25 Hz	27 mm	.25 Hz	5 mm	On (ultra)	Off	-8.6
.75 Hz	27 mm	.25 Hz	5 mm	On (ultra)	On	2.3
0.75 Hz	3 mm	.25 Hz	3 mm	Off	Off	0
0.75 Hz	3 mm	.25 Hz	3 mm	Off	On	14.9

Table 19. Data Summary (continued)

Platform Motion	Platform Displace-ment	Vital Sign Frequency	Respiration Displacement	Mechanical Compensation	Motion Compensation	Signal to Interference Ratio (SIR)
0.75 Hz	6 mm	.25 Hz	3 mm	Off	Off	-1.8
0.75 Hz	6 mm	.25 Hz	3 mm	Off	On	8
0.75 Hz	12 mm	.25 Hz	3 mm	Off	Off	6
0.75 Hz	12 mm	.25 Hz	3 mm	Off	On	11.5
0.75 Hz	17 mm	.25 Hz	3 mm	Off	Off	14.6
0.75 Hz	17 mm	.25 Hz	3 mm	Off	On	4.7
0.75 Hz	23 mm	.25 Hz	3 mm	Off	Off	-27
0.75 Hz	23 mm	.25 Hz	3 mm	Off	On	6.5
0.75 Hz	27 mm	.25 Hz	3 mm	Off	Off	3.5
0.75 Hz	27 mm	.25 Hz	3 mm	Off	On	26
0.75 Hz	33 mm	.25 Hz	3 mm	Off	Off	-2.7
0.75 Hz	33 mm	.25 Hz	3 mm	Off	On	23
0.75 Hz	38 mm	.25 Hz	4.8 mm	Off	Off	-5.1
0.75 Hz	38 mm	.25 Hz	4.8 mm	Off	On	-13.8

22.1 In-Range Motion Compensation vs Platform Stabilization Performance

22.1.1 Motion Compensation Algorithm SIR Performance

The motion compensation algorithm is very effective in improving the SIR with a range of improvement from 6 dB to 42 dB for 16 test cases with the mean SIR improvement of 19 dB. Without motion compensation enabled, the same test cases had SIR values between -29 dB to 6 dB with the mean SIR = -5.5 dB. The SIR scatter plot and SIR improvement are summarized below. All SIR improvement values in the scatter plot are with respect to the baseline measurements before motion compensation was applied (OFF/OFF refers to motion compensation OFF and platform stabilization OFF).

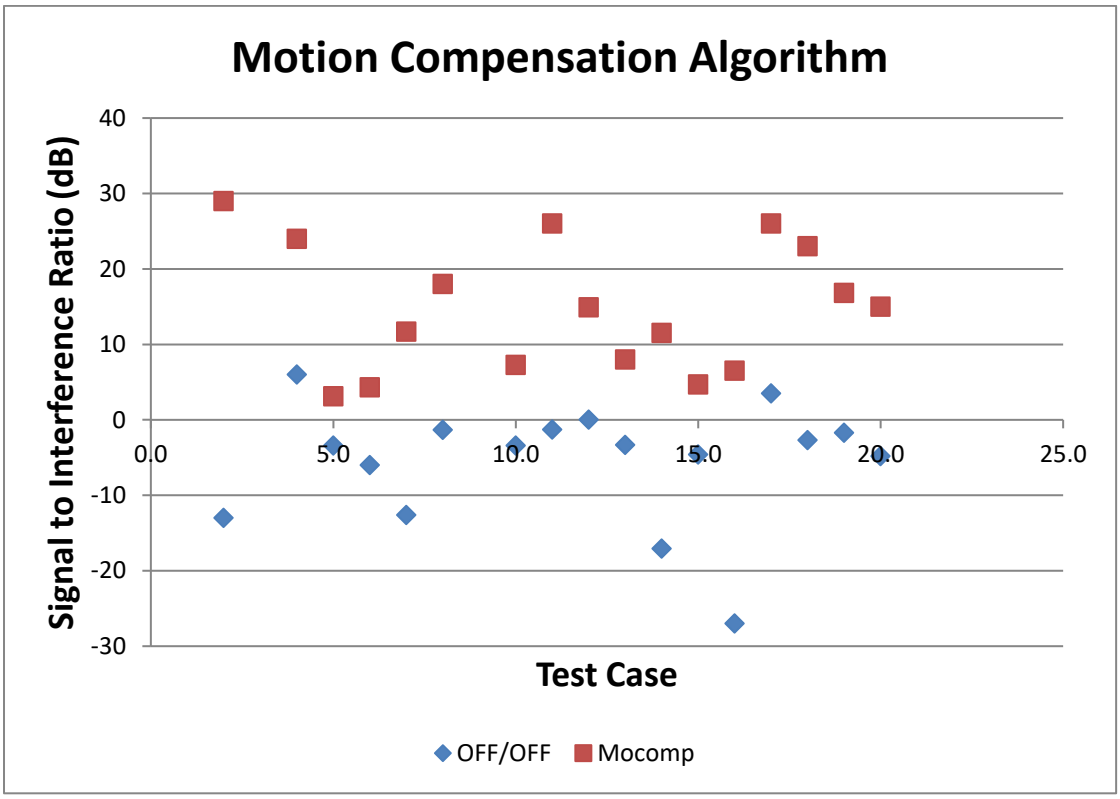

	Motion Comp OFF	Motion Comp ON
Mean (dB)	-5.5	14.7
Std Deviation	8.0	8.7

Figure 92. Motion compensation algorithm Signal to Interference Ratio.

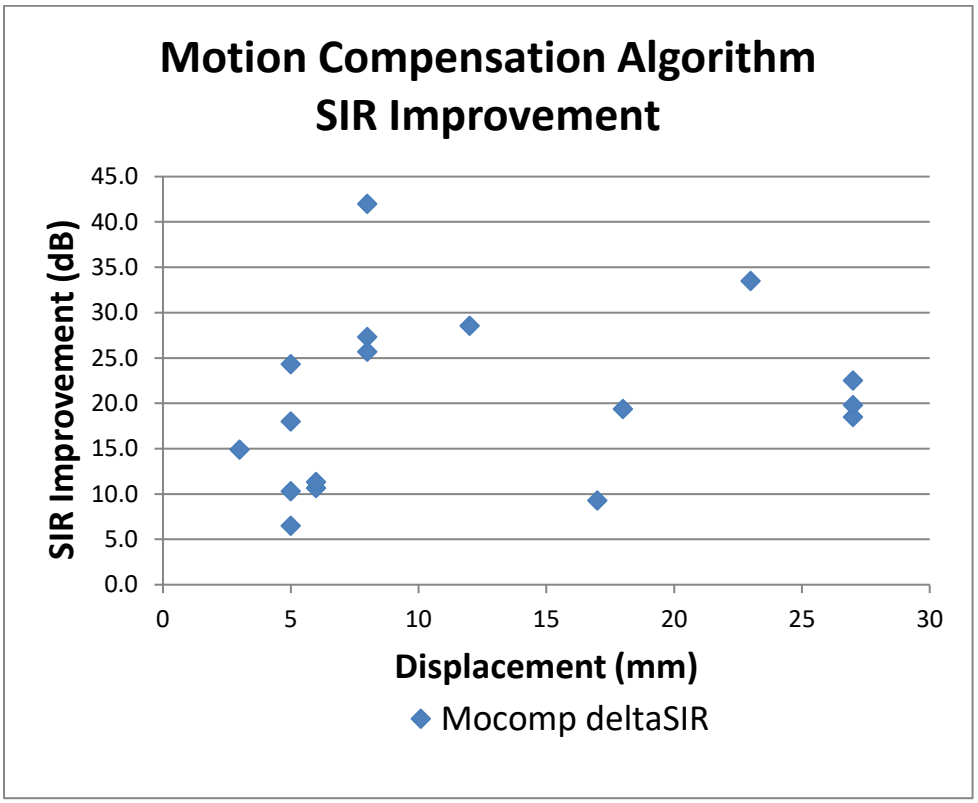

	Mean	Standard Deviation
SIR Improvement	19.0 dB	10.3 dB

Figure 93. Motion compensation algorithm performance.

22.1.2 Platform Stabilization Performance

The platform stabilization performance is summarized in this section. All SIR improvement values in the scatter plots are relative to baseline measurements made before any platform stabilization was applied. The radar sensor platform stabilization improved the SIR by an average of 6.2 dB, while the ultrasonic sensor platform stabilization improved the SIR by 5.2 dB. In some cases, the SIR was made worse by the platform stabilization. PID tuning and adjustments were made but obtaining a perfectly synchronized amplitude and speed between the stabilization sub-platform and the underlying platform was difficult. This is likely due to the Arduino Uno controller latency in processing the slope calculation that is used to determine the direction reversal of the stabilization sub-platform.

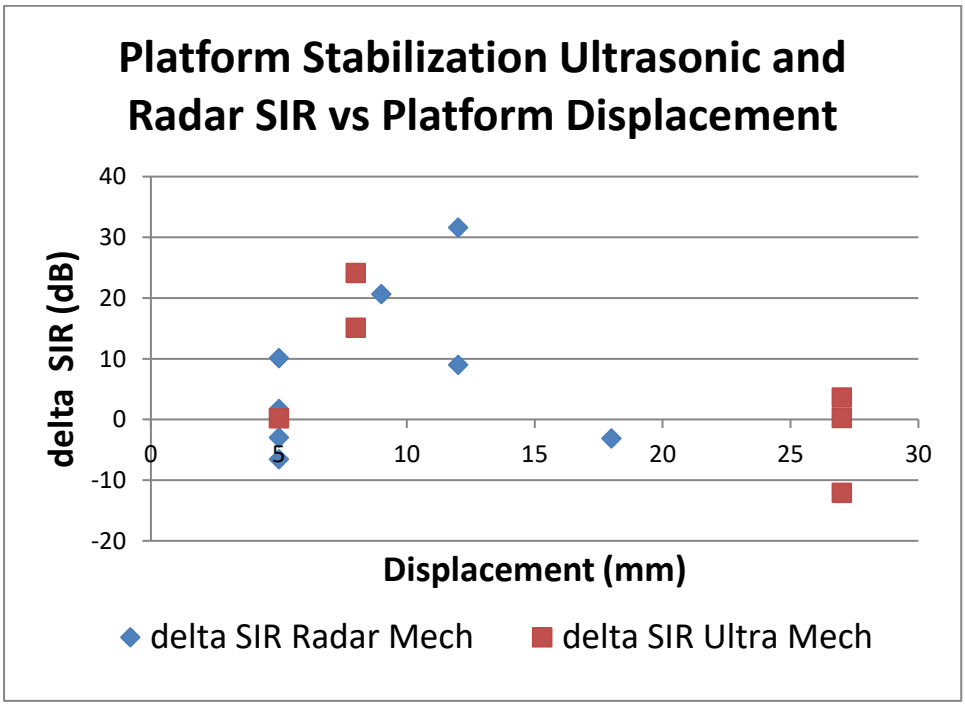

	Radar Platform Stabilization	Ultrasonic Platform Stabilization
Mean SIR Improvement	6.2	5.2
Std Deviation	12.0	12.7

Figure 94. Platform stabilization performance.

22.1.3 Combined Motion Compensation and Platform Stabilization Performance

The motion compensation algorithm performance is compared with the radar and ultrasonic platform stabilization performance in Figure 95 at platform displacements from 3 mm to 27 mm. The combination of both motion compensation and platform stabilization is compared as well. The SIR improvement is shown in Figure 96. For each displacement with measured results, the baseline SIR along with the SIR for motion compensation, platform stabilization and both motion compensation and platform stabilization are shown.

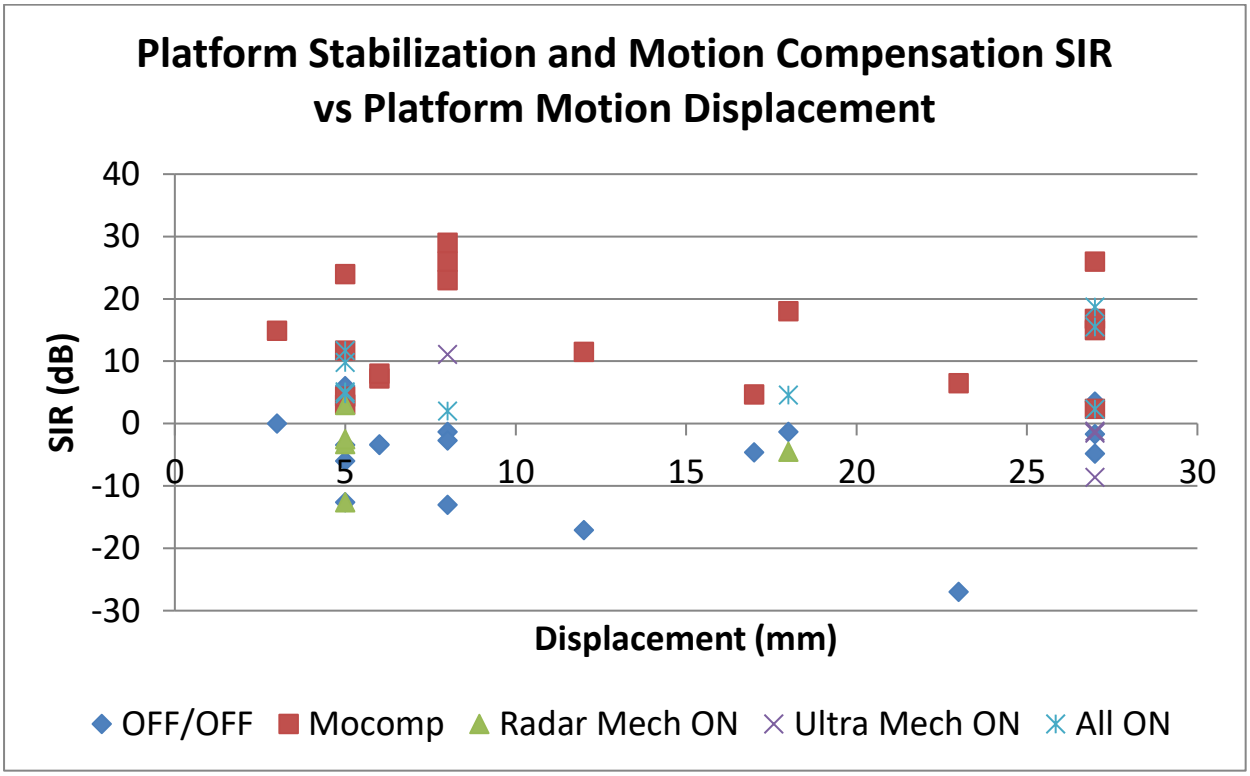

	OFF/OFF	Motion Compensation	Radar Mech ON	Ultra Mech ON	All ON
Mean SIR	-6.0	14.0	-0.5	0.0	8.3
Std Deviation	9.0	8.8	5.7	8.2	6.0

Figure 95. Motion compensation algorithm vs platform stabilization Signal to Interference Ratio as a function of platform motion displacement.

Motion compensation alone performs better (18 dB average SIR improvement) than motion compensation combined with either radar or ultrasonic platform stabilization (12.0 dB average SIR improvement).

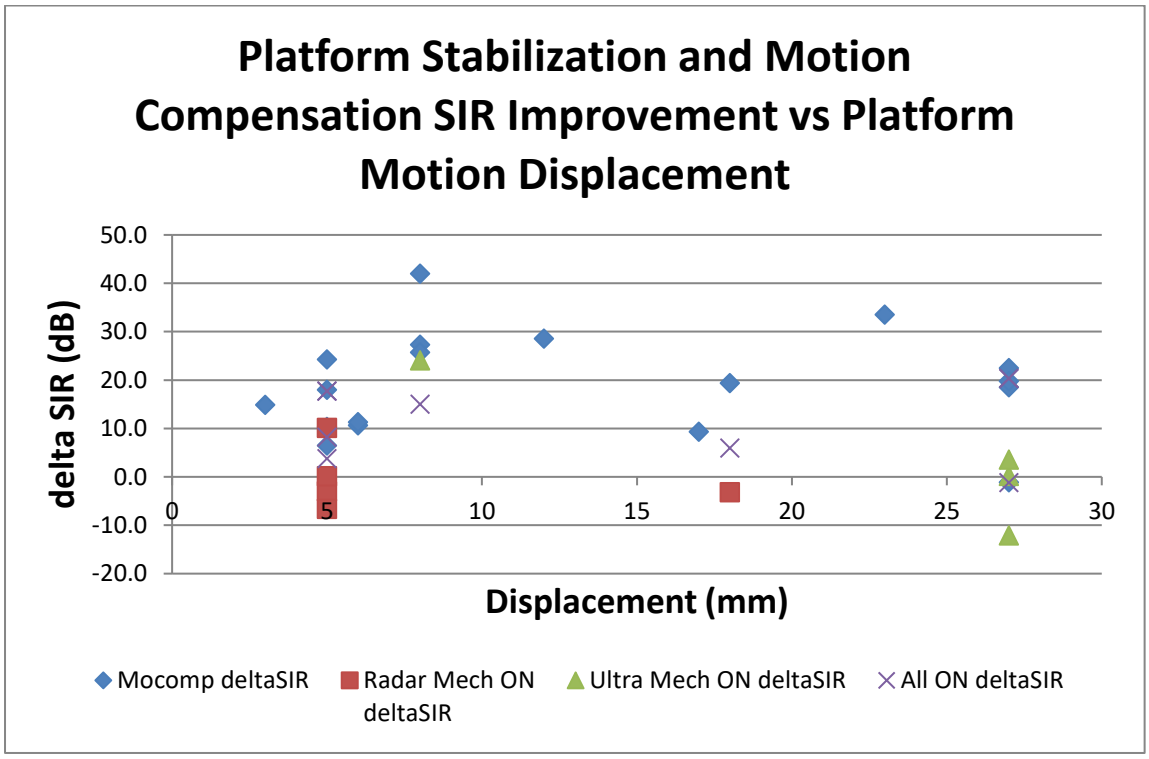

	Motion Compensation	Radar Mech ON	Ultra Mech ON	All ON
Mean SIR Improvement	18.0	6.2	4.0	12.0
Std Deviation	11.1	12.0	15.0	8.0

Figure 96. Motion compensation algorithm vs platform stabilization Signal to Interference Ratio improvement as a function of platform motion displacement.

For clarity, the 5 mm column in Figure 96 is expanded in Figure 97. Either motion compensation alone or motion compensation combined with platform stabilization gives the best performance.

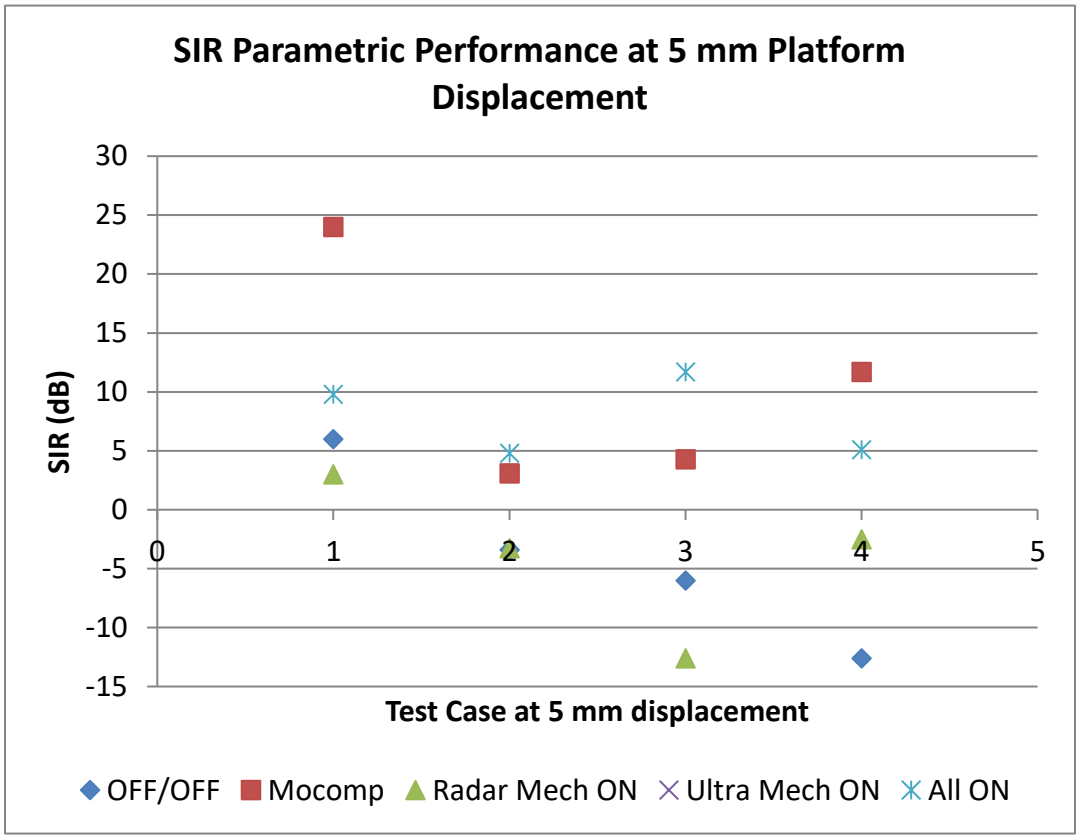

Figure 97. Motion compensation and platform stabilization parametric performance for 5 mm platform displacement.

While the expectation was that the platform stabilization would improve the combined motion compensation plus platform stabilization result (All ON in the plot), in the majority of the cases, motion compensation alone resulted in the best SIR performance. This can be attributed to the imperfect platform stabilization creating additional noise components. However, at platform motion amplitudes exceeding the radar wavelength, the platform stabilization is essential to reduce the overall motion to less than a wavelength. This dependency was shown in Figure 69.

23.0 Cross Range Motion Compensation Experiment

23.1.1 Radar RSSI Cross-Range Platform Stabilization

Cross-range experiments were also conducted to stabilize the platform in the direction orthogonal to the radar antenna boresight. This is necessary to ensure that the platform doesn't drift away from the target and to maintain adequate SNR. One approach is to monitor the Received Signal Strength Indicator (RSSI) of the respiration signal. RSSI is inversely proportional to range, thus the maximum RSSI should occur when the UAV is directly over the targeted signal of interest. Once the target is acquired, any reduction in RSSI while maintaining a fixed altitude, would be attributable to unwanted lateral motion

During signal acquisition and lock, the RSSI level can be used to generate an error signal to drive the motion feedback control system. For a quadcopter, the motion control can be implemented by real time inputs to the drone Electronic Speed Controller so that the platform position relative to the radar target boresight remains constant, thus maximizing the radar SNR and improving the probability of detection.

Multipath that could affect the RSSI would be more pronounced at grazing angles. Since the radar is pointed directly below the hovering platform, multipath effects are minimal.

The antenna beam pattern for the radar module used in the experiment is shown in Figure 98. Peak gain occurs at the antenna bore sight and falls off monotonically in the E and H planes until the sidelobes are present. The RSSI peak detection and tracking concept is illustrated in Figure 99.

K-LC1 Beam Pattern

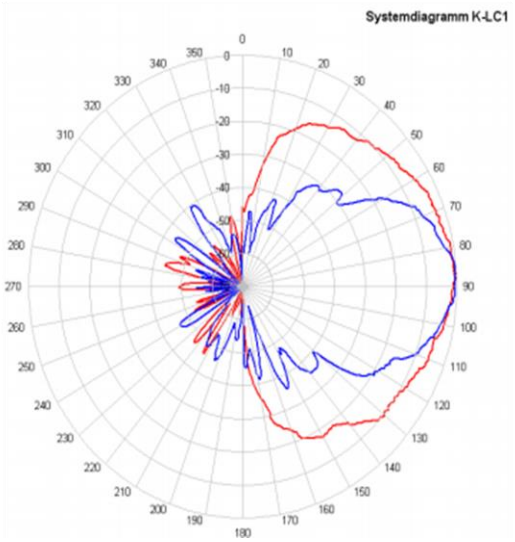

Figure 98. RFBeam Microwave K-LC1 radar module beam pattern used for RSSI measurements

Scan and Track Concept Using RSSI Peak Detection

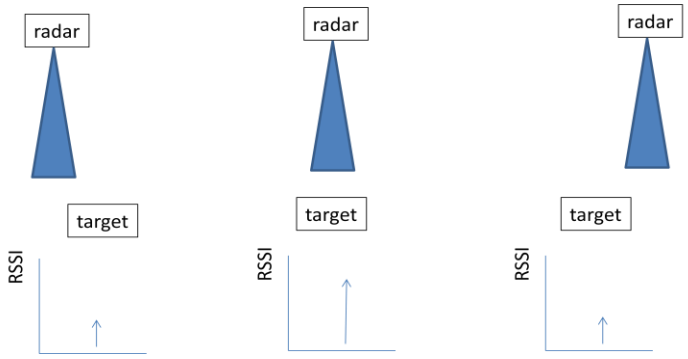

Figure 99. RSSI behavior as a function of cross-range position.

A Matlab Simulink simulation is shown in Figure 100. Note that the error signal in the bottom right plot is at a minimum when the RSSI is at a maximum.

Simulink RSSI Model

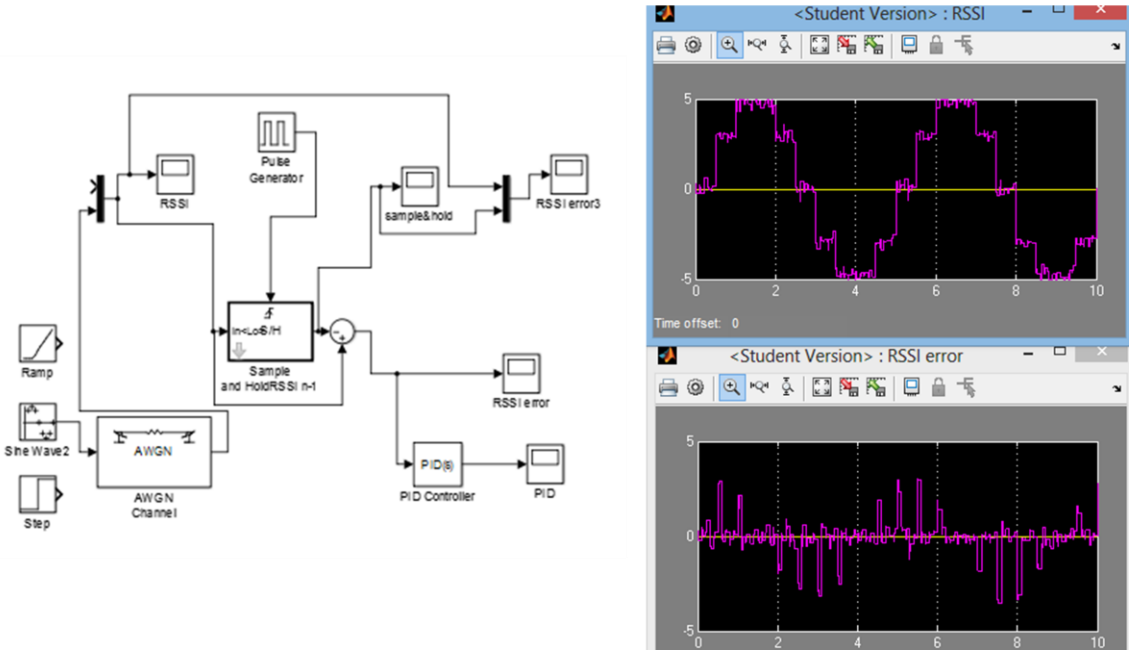

Figure 100. Simulink model for RSSI with random noise. The RSSI error signal is used to drive a PID feedback loop controller.

The RSSI level from the baseband signal of an IQ radar was analyzed, simulated and measured to derive motion compensation signals for a benchtop platform test bed. We performed cross-range RSSI stabilization experiments with the configuration as shown in Figure 101. A hemispherical reflector was setup on a linear translation stage with its motion perpendicular to the radar bore sight (cross-range).

The experimental test bed used to characterize the RSSI motion compensation is shown in Figure 4. A 24 GHz K-band I/Q radar transceiver, the RFBeam Microwave K-MC4 was used to measure the received power of a signal reflected from a hemispherical target mounted to the motion compensation mover. The motion compensation assembly was mounted to a Galil Motion Control platform mover that was programmed with a 0.4 Hz sinusoid with 1.75 inch displacement to simulate the quadcopter cross range movement. The motion compensator was controlled by an Arduino Uno microcontroller, which was programmed to read the I and Q channels of

the radar and compute the instantaneous power by calculating the square root of $I^2 + Q^2$.

Both the I and Q channels were conditioned by a pre-amplifier with a gain of 50 and pass band between 0.3Hz and 1 Hz. Since the pre-amp outputs are dual ended and the Arduino analog inputs require positive voltages, an op amp level shifter was used to shift the pre-amp output to a positive voltage range.

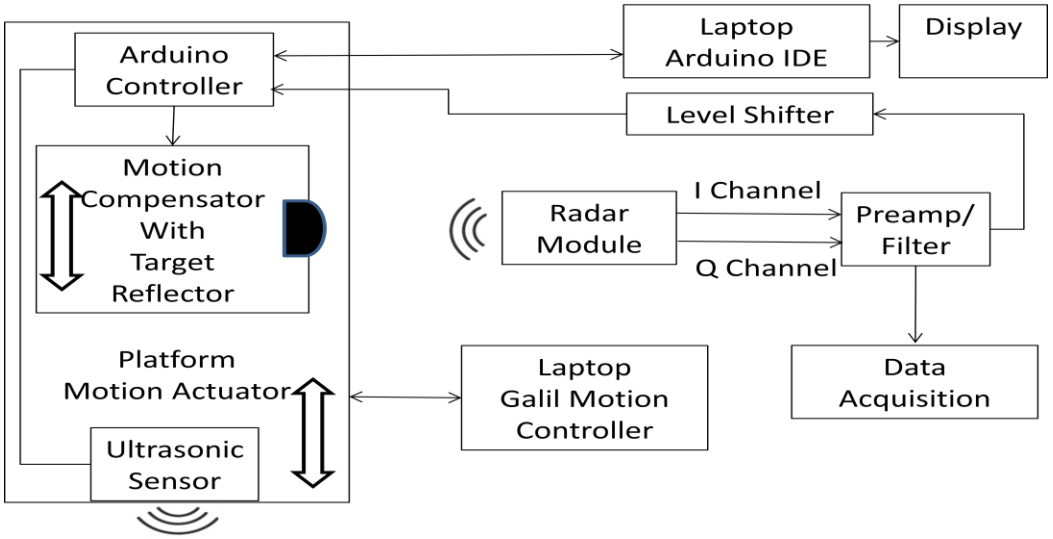

(a)

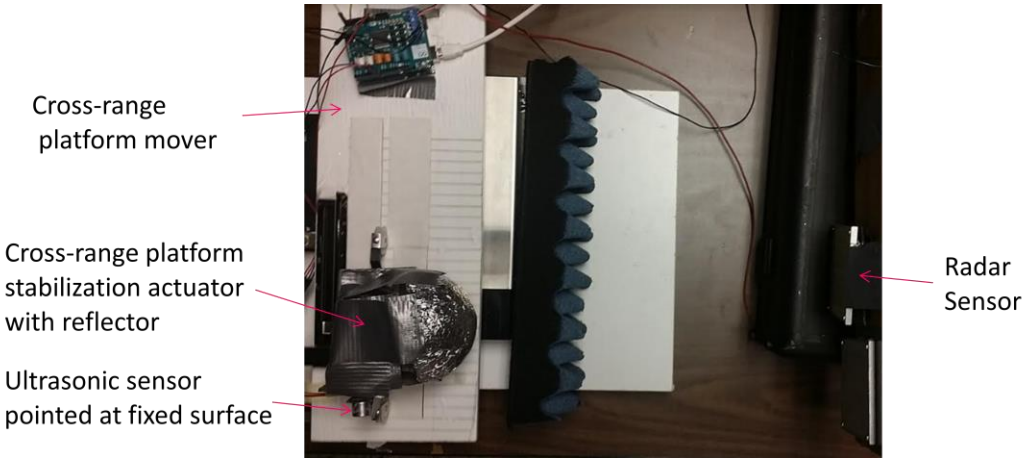

(b)

Figure 101. Cross range RSSI experiment.
(a) Block diagram of experiment to stabilize cross range motion using radar RSSI. (b) cross range experiment setup.

Figure 102 shows the RSSI power level as the movable platform traversed the radar cross range with a sinusoidal waveform with 1.75 inches amplitude and 0.4 Hz frequency (2.5 seconds period). The platform motion was set up such that the motion end points were beyond the radar beam width so that the RSSI would be at a minima at the endpoints. This means the RSSI peak occurs at the midpoint between the endpoints and the RSSI and range curves would be in anti-phase as is the case in Figure 102. An ultrasonic sensor was used to provide a real-time readout of the cross-range position and is superimposed on the RSSI plot. This confirmed that the peak power levels occurred when the Galil mover was at the center of its range of motion.

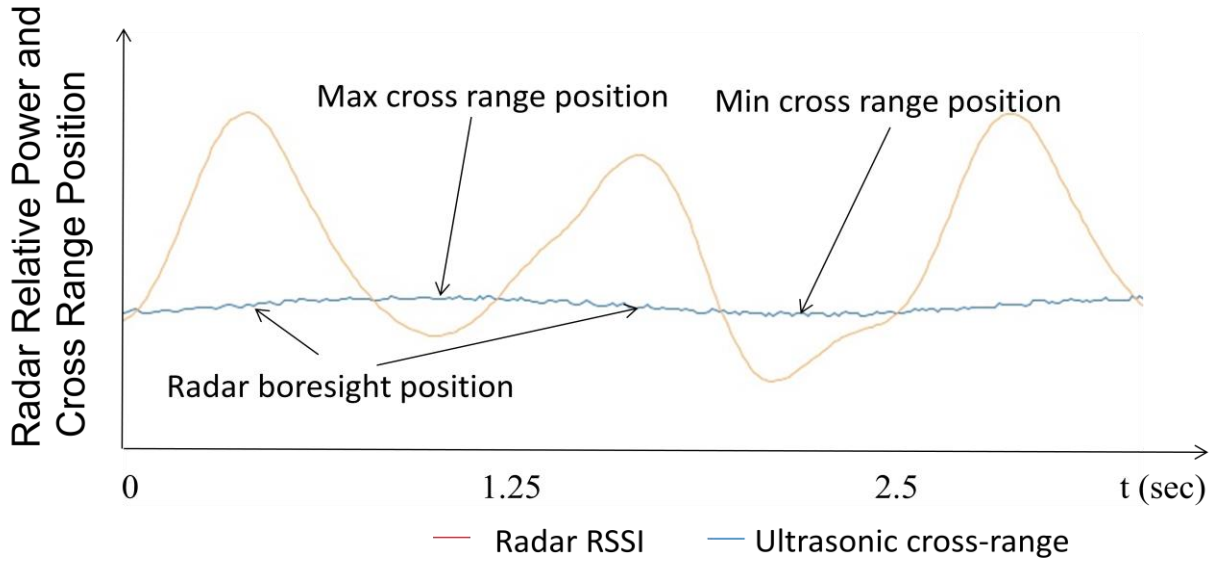

Figure 102. Cross range power measured by radar (red) versus cross range position measured by ultrasonic sensor (blue). Radar power variation as a function of cross-range position with a sinusoidal platform motion with 1.75 inches amplitude and 0.4 Hz frequency (period of 2.5 seconds). Lower amplitude plot shows the cross-range position, confirming that the RSSI peaks occur at the center of the range of motion.

We also implemented a PID feedback loop using the Arduino Uno controller to compensate for the cross-range platform motion. The error signal was based on the difference between the peak RSSI value and the RSSI value at the off-boresight position. We found, however, that the PID controller was not stable and introduced jitter into the motor driven motion compensation cart.

For the motion compensator algorithm, several parameters were used. These included the power and the rate of change of power for the slope parameter. Both the power and slope values are filtered in the algorithm to reduce the noise using a scaling factor. A threshold for the absolute value of the slope and the sign of the slope is used to determine when to reverse the direction of the motion compensator. The compensator speed was also weighted to increase its response when the signal power level dropped. When the compensator is near the desired position, corresponding to the RSSI peak, the compensator speed was reduced.

The main loop of the Arduino code is shown in the Appendix. The calculations for power, sampling filter scaling factor (sFactor) and compensation speed as a function of power are calculated. The algorithm was tuned by empirically optimizing the sFactor and compensator response speed. The loop delay parameter determined the duration for which the compensator was applied. A longer delay would drive the compensator in a given direction at the computed speed until the next loop cycle when the power is recomputed.

When the cross-range motion compensation is enabled, the dwell time of the radar on the target will increase, resulting in an increase in the mean power level. The baseband radar signal output power was measured with and without the motion compensation enabled. The mean power level was computed for both cases and is plotted in Figure 103. The mean power level was 1.5 dB higher with cross-range motion compensation.

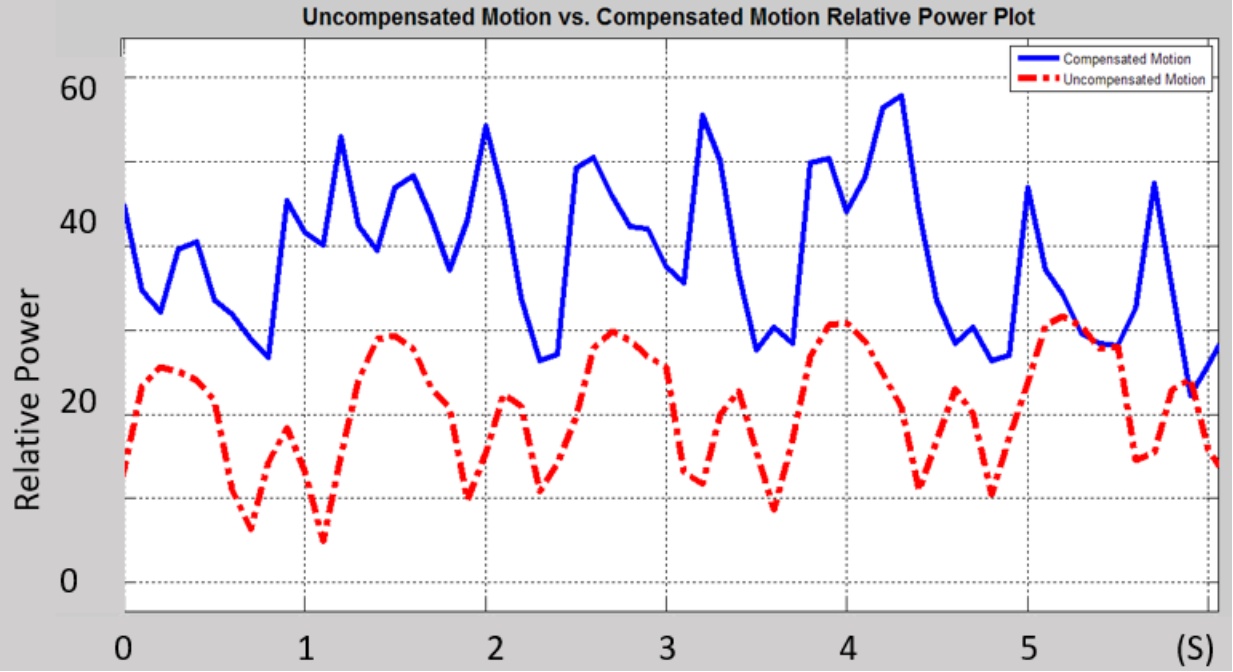

Figure 103. Mean radar signal power with and without motion compensation. The difference in mean power level was 1.5 dB.

23.1.2 Cross-Range RF DOA Measurements

A COTS K-MC4 radar transceiver from module RF Beam Microwave was evaluated for RF DOA accuracy. The module contains two coherent receivers, with each receiver providing an in-phase (I) and quadrature (Q) output channel. The receiver antenna array has two linear arrays separated by 13.7 mm, each with an independent receiver. See Figure 104.

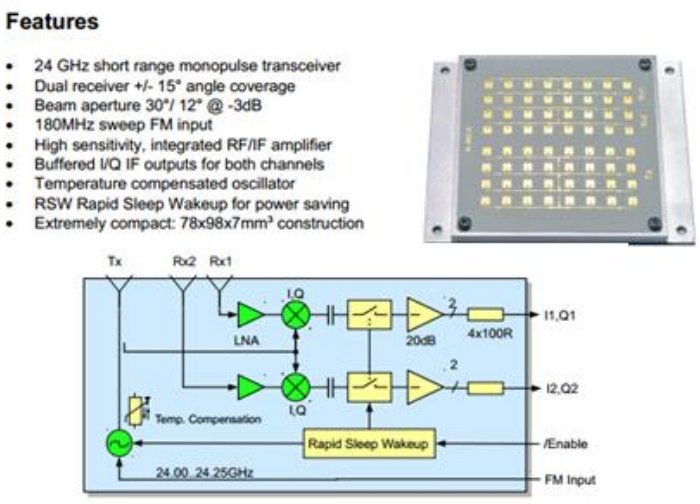

Figure 104. RFBeam Microwave radar transceiver with DOA capability.

By comparing the phase delay between the adjacent linear arrays, the angle of incidence of the received signal can be determined. The direction of arrival geometry is shown in Figure 105 (a).

The phase delay between adjacent elements is :

$$\varphi = k\, d \cos(\alpha)$$

$$\alpha = (I_2 - I_1)/k = \Delta\varphi/6.7$$

where φ is the phase shift between the signal received at Rx1 and Rx2 ($I_2 - I_1$), α is the angle of incidence and k = 6.7. Using these equations, the angle of arrival is calculated and compared with the measured angles. See Figure 105(b).

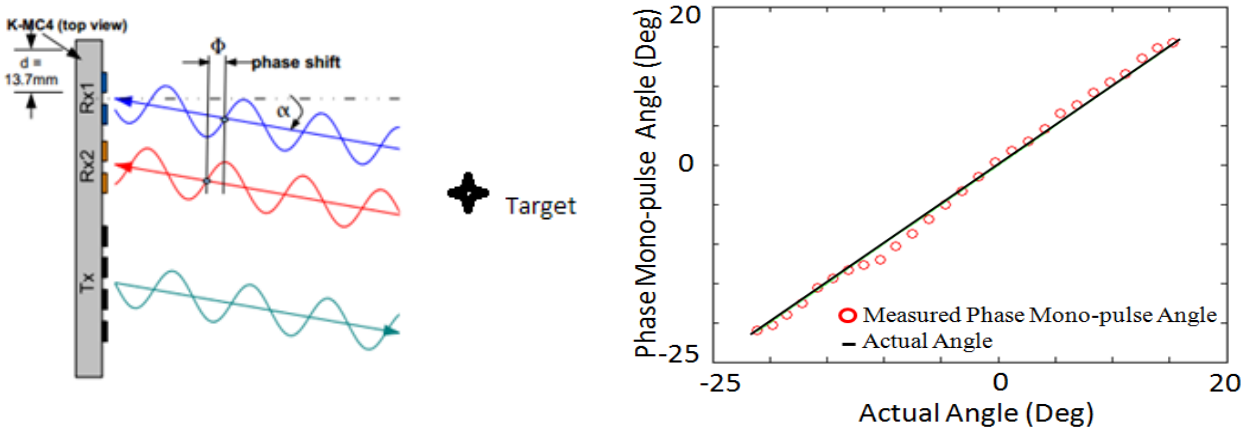

(a) (b)

Figure 105. (a) Direction of arrival measurement using phase difference measurement between antenna array element column 1 (RX1) and column 2 (RX2). DOA measurements with the RFBeam Microwave K-MC4 radar module.

The cross-range stabilization using the K-MC4 RF DOA capability was not implemented as it requires a real-time DAQ and processor in the feedback loop. The processor would need to be fast enough to compute the RD DOA in real-time and apply a feedback control mechanism similar to that implemented with the Arduino controller described earlier.

24.0 Conclusions

We demonstrated that unwanted platform motion can be compensated for using phase motion compensation individually or in conjunction with platform stabilization, thereby improving the SIR of a Doppler radar signal that would otherwise be corrupted. Simulation and the analysis of experimental data using secondary radar and ultrasonic sensors to derive motion compensation signals were performed.

Motion compensation was accomplished using a secondary radar that measured the platform motion. The secondary radar sensor output was then fused with the primary radar sensor that measured the composite motion of both the target and the platform motion. The motion compensation algorithm removes the unwanted platform motion from the primary radar signal by applying a cosine expansion algorithm to remove the unwanted phase modulation from the composite signal. The resulting performance improvement was 19 dB on average using motion compensation alone.

We also observed that the motion compensation algorithm performance degrades when the platform motion exceeds the radar wavelength (30 mm at 10 GHz) due to significant phase wrapping. With lesser degrees of phase wrapping, the motion compensation algorithm suppresses the harmonics that are introduced and enhances the target (respiration) signal frequency.

A second approach stabilizes the platform mechanically in real-time to minimize the motion induced phase modulation of the primary radar signal. An ultrasonic sensor or a secondary radar sensor is used to generate a feedback signal corresponding to the platform motion. A PID feedback loop uses the slope of the motion sensor signal to generate an error voltage that moves a mechanical actuator in anti-phase to the platform motion. Ultrasonic sensor platform stabilization improved the SIR by an average of 5.2 dB and the radar sensor platform stabilization improved the average SIR by 6.2 dB. The overall SIR improvement with motion compensation and platform stabilization was 12.4 dB.

While the expectation was that the combined platform stabilization and motion compensation algorithm performance would be superior to platform stabilization or motion compensation alone, we observed that the motion compensation algorithm performance by itself had the best SIR improvement. This is attributed to the imperfect platform motion cancellation by the platform stabilization mechanism. We found it challenging to match the motion amplitude, direction reversal timing (lag) and speed of the sub-platform with the platform motion and spent a significant effort tuning the PID feedback loop to minimize these mismatches.

We conclude that for platform motion magnitudes that are less than a half wavelength of the vital signs sensor, motion compensation using the secondary radar sensor is sufficient. When the platform motion magnitude exceeds a half wavelength, platform stabilization using the ultrasonic sensor can further improve the SIR, provided that the feedback loop mismatches are minimized. This could be achieved with a more powerful processor than the Arduino controller that was used for these experiments.

For platform motion exceeding the radar wavelength, where phase wrapping is severe, platform stabilization is required for the motion compensation algorithm to be effective.

Cross-range stabilization can also improve the vital signs signal by maintaining the target on the primary radar antenna array bore sight. RSSI tracking is problematic due to noise on the error voltage signal in the feedback loop. With appropriate filtering executed on a faster processor, the observed jitter could be alleviated.

RF DOA sensing can also be used as an alternative error voltage source to track the target of interest. Another option, to be explored in the future, is to use image tracking to maintain the cross-range position of the platform relative to the target.

25.0 Future Work

The author is the recipient of a NSF East Asia Pacific Summer Institute post-doctoral research grant during the summer of 2017. In collaboration with researchers at Ritsumeikan University in Japan, the research conducted on this project will be extended to include the integration of camera sensors for cross-range platform stabilization from ongoing research as described in Section 17.2.8 [19]. If a ground reference is present in the image sensor field of view, the horizontal platform motion can be stabilized by locking on to the target. For a quad copter platform, this can be accomplished by providing a corrective lateral thrust to compensate for any lateral drift due to cross-winds or turbulence. This is analogous to the mechanical camera de-blurring function described earlier.

Ultimately, the goal is to implement the platform stabilization and motion compensation described in this work on a quad copter platform. The platform stabilization controller and actuators described here would be replaced with an Ardu-copter or equivalent commercially available quad copter controller to drive the on-board Electronic Speed Controllers (ESCs) that control the propeller speeds. Altitude stabilization (in-range stabilization) would be achieved using the secondary radar or ultrasonic sensor. Lateral translational motion would be compensated using one of the cross-range stabilization

techniques described earlier. Similarly, any yaw, pitch and roll attitude variations would be compensated with the cross-range sensor.

26.0 ACKNOWLEDGEMENTS

The wearable sensor system for monitoring body kinematics research was conducted with funding from the US Army under a Phase I SBIR contract. The methods and data are the property of Oahu Group LLC with US government data rights per contract Contract NO. W911QX-13-C-0148.

Additional work was supported in part by Award No. U54MD007584 from the National Institute on Minority Health and Health Disparities (NIMHD), National Institutes of Health (NIH), National Science Foundation (NSF) under grants CBET-1160326, ECS-0702234, ECCS-0926076, the University of Hawaii at Manoa REIS, and by Department of Energy grant DEOE0000394.

27.0 References

[1] C. Bregler, " "Motion Capture Technology For Entertainment [In The Spotlight]."," *IEEE Signal Processing.*

[2] Granum, "A survey of computer vision-basedhuman motion capture," *Computer Vision and Image Understanding.*

[3] R. Feliz, "Pedestrian tracking using inertial sensors," *Journal of Physical Agents,* vol. 3, pp. 35-42, 2009.

[4] M. DiRenzo, "Pulse Shape Distortion and Ranging Accuracy in UWB–based Body Area Networks for Full–Body Motion Capture and Gait Analysis," *IEEE GLOBECOM proceedings,* 2007.

[5] R. Nakata, I. Mostafanezhad and R. J. Nakata, "Wearable Sensor System for Monitoring Soldier Body Dynamics," *Final Report,* Jan, 2014.

[6] V. Ferrara, "Technical Survey About Available Technologies For Detecting Buried People Under Rubble Or Avalanches," *WIT Transactions on The Built Environment,* vol. 150, no. May, pp. 91-101, 2015.

[7] V. Lubecke, O. Boric-Lubecke, J. Lin, C. Li, "A review on recent advances in Doppler radar sensors for noncontact healthcare monitoring," *IEEE Trans. Microwave Theory and Techniques,* vol. 61, no. 5, pp. 2046-2060, May 2013.

[8] A. Droitcour, V. Lubecke, J. Lin and O. Boric-Lubecke, "A microwave radio for Doppler radar sensing of vital signs," 2001.

[9] C. Li,. J. Lin, "Random Body Movement Cancellation in Doppler Radar Vital Sign Detection," *IEEE Trans. on Microw. Theory Techn,* vol. 56, no. 12, pp. 3143-3152, Nov 2008.

[10] I. Mostafanezhad, V. Lubecke, O. Boric-Lubecke, "Application of empirical mode decomposition in removing fidgeting interference in Doppler radar life signs monitoring devices," in *Annu. IEEE Int. Eng. Med. Biol. Soc. Conf*, Minneapolis.

[11] J. S. Paresh Rawat, "Review of Motion Estimation and Video Stabilization techniques For hand held mobile video," *Signal & Image Processing : An International Journal (SIPIJ,* vol. 2, no. 2, p. DO:10.5121/sipij.2011.2213 159, June 2011.

[12] C. Mongrédien, " Centimeter-Level Positioning for UAVs and Other Mass-Market Applications," in *Institute of Navigation GNSS Conference*, Portland, 2016.

[13] T. Suzuki, "Precise UAV Position and Attitude Estimation by Multiple GNSS Receivers for 3D Mapping," in *Institute of Navigation Pacific PNT Conference*, Portland, 2016.

[14] R. Vaghefi, "Cooperative RF Pattern Matching Positioning for LTE Cellular Systems," in *25th Annual International Symposium on Personal, Indoor and Mobile Radio Communications*, 2014.

[15] A. Freedman, "Prediction Based RSS Fingerprinting for Positioning and Optimization in Cellular Networks," in *IEEE 27th Convention of Electrical and Electronics Engineers in Israel*, 2012.

[16] S.-C. Yeh, "Performance improvement of offline phase for indoor positioning systems using Asus Xtion and smartphone sensors," *Journal of Communications and Networks,* vol. 18, no. 5, 2016.

[17] M. Skolnik, Introduction to Radar Systems 3rd Edition.

[18] A. Singh, "Subject isolation and non stationary clutter rejection using RF backscatter tag radar," Ph.D. dissertation, Dept. Elect. Eng., University of Hawaii at Manoa, Honolulu, HI, USA,," Honolulu, 2012.

[19] K. N. Y. Takaba, "Visual Feedback Altitude Control of Quadcopters," in *Proceedings of the 50th Annual Conference of the Institute of Sytems, Control and Information Engineers (ISCIE)*, Osaka, May 20-22, 2015.

[20] A. S. a. V. Lubecke, "Adaptive noise cancellation for two frequency radar using frequency doubling passive RF tags," *IEEE Trans. Microw. Theory Techn,* vol. 61, no. 8, pp. 2975-2981, 2013.

[21] S. Haykin, Kalman Filtering and Neural Networks, ISBN: 978-0-471-36998-1.

[22] O. Boric-Lubecke and e. al., Doppler Radar Physiological Sensing, Wiley, 2015.

[23] P. Gulden, S. Roehr, M. Christmann, “An overview of wireless local positioning system configurations”, IEEE Int. Microwave Workshop on Wireless Sensing, Local Positioning, and RFID, Sept. 2009, pp. 1 – 4

[24] H. Liu et al., “Survey of Wireless Indoor Positioning Techniques and Systems”, IEEE Transactions on Systems, Man, and Cybernetics, vol. 37, no. 6, Nov. 2007, pp. 1067 - 1080

[25] M. Vossiek et al., “Wireless local positioning”, IEEE Microwave Magazine, vol. 4, Issue 4, Dec. 2003, pp. 77 – 86

[26] G. Yanying, A. Lo, L. Niemegeers, “A survey of indoor positioning systems for wireless personal networks”, IEEE Communications Surveys & Tutorials, vol. 11, no. 1, 2009, pp. 13 – 32

[27] K. Pahlavan, L. Xinrong J. P. Makela, “Indoor geolocation science and technology”, IEEE Communications Magazine, vol. 40, no. 2, Feb. 2002, pp. 112 - 118

[28] Ni, L. M., Liu, Y., Lau, Y. C., and Patil, A. P., Indoor Location Sensing Using Active RFID, 2004, Wireless Networks, 10(6), pp. 701-710.

[29] Wang, J. S., and Shen, Z. X, An Improved Music TOA Estimator for RFID Positioning, 2002, Radar 2002, pp. 478-482.

[30] Nikitin, P. V., Martinez, R., Ramamurthy, S., and Leland, H., 2010, Phase Based Spatial Identification of UHF RFID Tags, RFID, 2010 IEEE International Conference on IEEE, pp. 102-109.

[31] Zhou, J., Zhang, H., and Mo, L. Two-dimension Localization of Passive RFID Tags Using AOA Estimation, 2011, IEEE Instrumentation and Measurement Technology Conference, pp. 1-5.

[32] Yang, L., Chen, Y., Li, X.-Y., Xiao, C., Li, M., and Liu, Y., Real-time Tracking of Mobile RFID Tags to High Precision Using COTS Devices, 2014, Proceedings of the 20th annual international conference on Mobile computing and networking ACM, pp. 237-248.

[33] M. Bouet, A. L. dos Santos, “RFID tags: Positioning principles and localization techniques”, 1st IFIP Wireless Days, Nov. 2008, pp.1 – 5

[34] J. Zhou, J. Shi, “RFID localization algorithms and applications—a review”, Journal of Intelligent Manufacturing, vol. 20, no. 6, December, 2009, pp. 695-707

[35] Youngsu Park et al., “Improving position estimation on RFID tag floor localization using RFID reader transmission power control”, IEEE Int. Conference on Robotics and Biometrics, Feb. 2009, pp. 1716 – 1721

[36] S. Azzouzi, M. Cremer, U. Dettmar, and R. Kronberger, “New measurement results for the localization of UHF RFID transponders using an angle of arrival (AOA) approach,” in Proc. IEEE Int. Conf. RFID, 2011, pp. 155–161.

[37] T. Xiong, J. Liu, Y. Yang, X. Tan, and H. Min, “Design and implementation of a passive UHF RFID-based real time location system,” in Proc. IEEE VLSI-DAT, Apr. 2010, pp. 95–98.

[38] J. Heidrich, D. Brenk, J. Essel, G. Fischer, R. Weigel, and S. Schwarzer, “Local positioning with passive UHF RFID transponders,” in Proc. IEEE MTT-S IMWS, 2009, pp. 1–4.

[39] A. Wille, M. Broll, and S. Winter, “Phase difference based RFID navigation for medical applications,” in Proc. IEEE Int. Conf. RFID, Apr. 2011, pp. 162–169.

[40] P. Nikitin, R. Martinez, S. Ramamurthy, H. Leland, G. Spiess, and K. Rao, “Phase based spatial identification of UHF RFID tags,” in Proc. IEEE Int. Conf. RFID, 2010, pp. 102–109.

[41] C. Hekimian-Williams, B. Grant, X. Liu, Z. Zhang, and P. Kumar, “Accurate localization of RFID tags using phase difference,” in Proc. IEEE Int. Conf. RFID, 2010, pp. 89–96.

[42] X. Li, Y. Zhang, and M. Amin, “Multifrequency-based range estimation of RFID tags,” in Proc. IEEE Int. Conf. RFID, 2009, pp. 147–154.

[43] D. Arnitz, K. Witrisal, and U. Muehlmann, “Multifrequency continuous-wave radar approach to ranging in passive UHF RFID,” IEEE Trans. Microw. Theory Tech., vol. 57, no. 5, pp. 1398–1405, May 2009.

[44] C. Zhou, J. Downey, D. Stancil, and T. Mukherjee, “A shoe to shoe RF ranging sensor for aiding inertial navigation,” in Proc. 74th IEEE VTC Fall, San Francisco, CA, Sep. 2011, pp. 1–5.

[45] Malavika Panicker1 , Tanzeela Mitha2 , Multisensor Data Fusion for an Autonomous Ground Vehicle, 2016 Conference on Advances in Signal Processing (CASP) Pune. Jun 9-11, 2016

Appendix A: Software Code
MATLAB Motion Compensation Simulation

```
clear all
close all;
clc;
lambda=3e8/10e9
respfreq=.25
platfreq=1
t=0:.001:10;
V2M=.0025;
%scalar amplitudes for respiration and platform motion
A=1
B=1

% respiration motion, platform motion and composite motion
platwav=A*cos(2*pi*platfreq*t);
respwav=B*cos(2*pi*(respfreq*t)+pi);

%alternative using angle sum identity cos(a+b)=cos(a)cos(b)-sin(a)sin(b)
composite_identity=A*B*cos(platwav).*cos(respwav)-sin(platwav).*sin(respwav)

%compensated = cos[(a+b)-a]=cos(a+b)*cos(a)+sin(a+b)*sin(a)
compensated=AmpMatchFACTOR*A*B*cos(2*pi*(platfreq+respfreq)*t).*cos(2*pi*platfre
q*t)+AmpMatchFACTOR*A*B*sin(2*pi*(platfreq+respfreq)*t).*sin(2*pi*platfreq*t);

%to simulate platform stabilization delay
delay=.0*pi
platwavdelay =
.1*AmpMatchFACTOR*A*B*cos(2*pi*(platfreq+respfreq+delay)*t).*cos(2*pi*platfreq*t)+.
1*AmpMatchFACTOR*A*B*sin(2*pi*(platfreq+respfreq)*t+delay).*sin(2*pi*platfreq*t)

plot (platwav),
hold on, plot(respwav,'r'),
hold on, plot (composite_identity,'g')
hold on, plot(platwavdelay,'-.m')
legend('platform','respiration','composite','compensated')
title('Time Domain Waveforms')
xlabel('Samples (1 mS/sample)')
ylabel('Voltage (V)')
figureHandle = gcf;
%# make all text in the figure to size 14 and bold
set(findall(figureHandle,'type','text'),'fontSize',14,'fontWeight','bold')
```

```
% platwavnoise = awgn(platwav,20,'measured','db');
% platwavnoise = awgn(platwav,10001,'measured');
% plot(platwavnoise)


Fs=1000
L=10000
NFFT = 2^nextpow2(L); % Next power of 2 from length of y
Y = fft((composite+respwav+platwav),NFFT)/L;
f = Fs/2*linspace(0,1,NFFT/2+1);
% Z=fft(compensated,NFFT)/L;

%plot uncompensated motion
figure(2)
Z=fft(composite+respwav+platwav,NFFT)/L;
% Z=fft(platwav,NFFT)/L;
stem(f,2*abs(Z(1:NFFT/2+1)))
title('Single-Sided Amplitude Spectrum of y(t)')
xlabel('Frequency (Hz)')
ylabel('|Y(f)|')

%plot compensated motion
figure(3)
Z=fft(compensated,NFFT)/L;
stem(f,2*abs(Z(1:NFFT/2+1)))
title('Single-Sided Amplitude Spectrum of y(t)')
xlabel('Frequency (Hz)')
ylabel('|Y(f)|')


%alternative using complex domain
respwavradar=A*real(exp(1i*(4*pi/lambda*respwav*V2M)));
platwavradar=B*real(exp(1i*(4*pi/lambda*platwav*V2M)));
compositeradar=A*B*real(exp(1i*(4*pi/lambda*(respwavradar+platwavradar)*V2M)));

platwav_angle=angle(hilbert(platwav));
PhaseConstant = -(4*pi/lambda)*platwav*V2M;
compensated = real(composite.*exp(1i*PhaseConstant));
%compensated=cos(platwav+respwav).*cos(platwav)+sin(platwav+respwav).*sin(platwav)

% Normalize Signal Amplitude
platwav = platwav-mean(platwav);
platwavradar = platwavradar-mean(platwavradar);
AmpMatchFACTOR = max(abs(platwavradar))/max(abs(composite));
```

```
composite = .7*AmpMatchFACTOR*composite;
compositeradar = .7*AmpMatchFACTOR*compositeradar;
compensatedradar=cos(platwavradar+respwavradar).*cos(platwavradar)+sin(platwavra
dar+respwavradar).*sin(platwavradar)

% plot (platwavradar),
% hold on, plot(respwavradar,'r'),
% hold on, plot (compositeradar,'g')
% hold on, plot(compensatedradar,'m','LineWidth',10)
```

MATLAB Motion Compensation Code

```
close all,
clear all, clc,

%  ====== SECTION 1 : CONSTANTS ======
%SET CONSTANTS
Length = 60000;
Start = 0001;
FreqSample = 1000;
dt = 1/FreqSample;
T = (dt:dt:(Length+1)*dt)';
V2M = 1e-3;
R2M = 1.5e-3; %radians to meters
AF2F = (FreqSample/(2*pi));
Freq = 10e9;
WaveLength = 2.99792458e8/Freq;
close all,

%  ====== SECTION 2 : IMPORT SIGNALS ======
file =
importdata('C:\Users\Bob\Dropbox\data\GALILONLY_ONEANDONEHALFIN_210000_P
T75HZ.txt');
% file = importdata('capture_2016-11-03--15-48-38 - Copy.txt');

%  ====== SECTION 3 : PROCESS SIGNALS ======

Galil_Motion = file(Start:Start+Length,4);
GalilRes_Motion = file(Start:Start+Length,2);

% Normalize Signal Amplitude
Galil_Motion = Galil_Motion-mean(Galil_Motion);
AmpMatchFACTOR =
max(abs(Galil_Motion(1000:5000)))/max(abs(GalilRes_Motion(1000:5000)));
% GalilRes_Motion = AmpMatchFACTOR*GalilRes_Motion;
GalilRes_Motion = AmpMatchFACTOR*GalilRes_Motion;
compensated=cos(GalilRes_Motion).*cos(Galil_Motion)+sin(GalilRes_Motion).*sin(Galil
_Motion)

%  ====== SECTION 4 : DATA PLOT ======
figure(1)
plot (Galil_Motion,'b'),
hold on, plot(GalilRes_Motion,'g'),
hold on, plot(compensated,'m')
title('Platform Motion Radar and Motion Compensation')
```

```
xlabel('Samples (1 mS/sample)')
ylabel('Voltage (V)')
legend('radar platform motion','primary radar','compensated')


Fs=1000
L=10000
NFFT = 2^nextpow2(L); % Next power of 2 from length of y
Y = fft(compensated,NFFT)/L;
f = Fs/2*linspace(0,1,NFFT/2+1);
% Z=fft(compensated,NFFT)/L;

%plot uncompensated motion
figure(2)
Z=fft(GalilRes_Motion,NFFT)/L;
stem(f,2*abs(Z(1:NFFT/2+1)))
title('Single-Sided Amplitude Spectrum of y(t)')
xlabel('Frequency (Hz)')
ylabel('|Y(f)|')


% comp=Y.*Z;
% Plot motion compensated spectrum.
figure(3)
Z=fft(compensated,NFFT)/L;
stem(f,2*abs(Z(1:NFFT/2+1)))
title('Single-Sided Amplitude Spectrum of y(t)')
xlabel('Frequency (Hz)')
ylabel('|Y(f)|')
```

MATLAB Adaptive LMS filter

```
clc
close all
clear all
 N=input('length of sequence N = ');
    t=[0:N-1];
   w0=.00125;  phi=0.1;%respiration freq
   w1=.0005;
   d=sin(2*pi*[1:N]*w0+phi);
x=d+sin(2*pi*[1:N]*w1);  %platform motion
   M = 5;
w=zeros(M,N);
mu=0.05;%input('mu = ')
  for i=(M+1):N
   e(i) = d(i) -  x((i-(M)+1):i)*w(:,i);
   e(i) = min(e(i),2);
   w(:,i+1) = w(:,i) + mu * e(i) * x((i-(M)+1):i)';
end
for i=(M+1):N
    yd(i) = x((i-(M)+1):i)*w(:,i);
    yd(i)=min(yd(i),2);
end
  subplot(221),plot(t,d),ylabel('Desired Signal (V)'),xlabel('mS'),legend('1.25Hz Resp'),
  subplot(222),plot(t,x),ylabel('Input Signal+Noise (V)'),xlabel('mS'),legend('1.25Hz Resp
+ .5Hz platform')
  subplot(223),plot(t,e),ylabel('Error (V)'),xlabel('mS'),
  subplot(224),plot(t,yd),ylabel('Adaptive Desired output (V)'),xlabel('mS'),
```

Arduino code for cross-range motion compensation using RSSI and RSSI slope.

```
I1readin = analogRead(analogPin3);
  Q1readin = analogRead(analogPin5);
  I1 = I1readin;
  Q1 = Q1readin;
  power = sqrt(I1 * I1 + Q1 * Q1);
  slope = power - powerold;
  slope = sFactor * slopeold + (1.0 - sFactor) * slope;
  powerold = power;
  spd = 160 + 20 - abs(power * (1e-2) * 2.5);
  if (abs(slope) > 0.02)
  if (slope < 0)
    if (digitalRead(directionPin) == LOW)
      digitalWrite(directionPin, HIGH);
      else digitalWrite(directionPin, LOW);
  analogWrite(speedPin, spd);
  delayMicroseconds(8);
```

Arduino code for ultrasonic sensor platform stabilization.

```
//SET VARIABLES
const byte trigPin = 7;
const byte echoPin = 6;
const byte speedPin = 11;
const byte directionPin = 13;
const byte maxSpeed = 250;
const float initialValue = 0.0;
const float sFactor = 0.95;
float newTarget = initialValue, oldTarget = initialValue, newError = initialValue, iError =
initialValue, output;
float Kp =50.0, Ki = 0, Kd = 0.0;
float P, I, D, pid, setpoint, oldError;

void setup(){
  Serial.begin (9600);

  pinMode(trigPin, OUTPUT);
  pinMode(echoPin, INPUT);
  pinMode(speedPin, OUTPUT);
  pinMode(directionPin, OUTPUT);

  //RESET TO MID-POSITION
  digitalWrite(directionPin, HIGH);
  analogWrite(speedPin,250);
  delay(400);

  digitalWrite(directionPin, LOW);
  analogWrite(speedPin,250);
  delay(150);
  analogWrite(speedPin,0);
  delay(1000);
}

void loop() {
  //OBTAIN NEW TARGET
  oldTarget = newTarget;

  digitalWrite(trigPin, LOW);
  delayMicroseconds(2);
  digitalWrite(trigPin, HIGH);
  delayMicroseconds(10);
  digitalWrite(trigPin, LOW);
  newTarget = (pulseIn(echoPin, HIGH, 11655))/58.2;
```

```
  //FILTER SENSOR
  if(!(oldTarget == initialValue))
  {
    newTarget = sFactor*oldTarget+(1.0-sFactor)*newTarget;
  }

    //VALID RANGE RETURNED
  if(!(newTarget == initialValue));
  {
    //DETERMINE ERROR
    oldError = newError;
    if(oldTarget == initialValue)
    {
      setpoint = newTarget;
    }
    else
    {
      newError = setpoint - newTarget;
    }

  // FILTER INTEGRAL ERROR
    iError = 0.0*oldError+1.0*newError;

  // CALCULATE OUTPUT
    P = Kp * newError;
    I = Ki * iError;
    D = -Kd * (newTarget - oldTarget);

    pid = P+I+D;

  // I-TERM FEEDBACK
    if (pid > 250)
    {
      iError -= pid - 250;
      output = maxSpeed;
    }
    else if (pid < -250)
    {
      iError += -250 - pid;
      output = maxSpeed;
    }
    else
    {
      output = abs(pid)+120; // rescale and adds offset and adds offset // little movement
until pwm > 150
    }
```

```
    //SET NEW DIRECTION AND SPEED IF GREATER THAN SETPOINT
    if(pid > 0)
    {
      digitalWrite(directionPin,LOW);//away
      analogWrite(speedPin,abs(output));
//      delayMicroseconds(8);
        delay(100);
    }
    else if (pid < 0)
    {
      digitalWrite(directionPin,HIGH);//towards
      analogWrite(speedPin,abs(output));
//      delayMicroseconds(8);
        delay(100);
    }
  }
  //OUTPUT TO SERIAL MONITOR
  Serial.println(pid,3);
}
```

Appendix B: Data Sheets

Microsemi

PLANAR TRANSCEIVERS

Fixed Frequency

MDU1020 Series

Operation

The basic principle of operation consists of detecting the frequency shift between a transmitted and a received signal reflected back from a moving object within the field of view of the unit.

The unit produces a low level output signal which can be amplified and processed to provide an audible or visual alarm signal and employs low cost surface mount manufacturing techniques which are field proven as being rugged and reliable.

Electrical Characteristics

Transmitter

Frequency	:	see table
Frequency Setting Accuracy	:	3MHz
Power Output (Min.)	:	13dBm EIRP
Operating Voltage	:	+5V ±0.25V
Operating Current (CW)	:	60mA max.
	:	40mA typ.
Harmonic Emissions	:	< -7dBm

Pulse Mode Operation

Average Current (5% DC)	:	2mA typ.
Pulse Width (Min.)	:	5µSec
Duty Cycle (Min.)	:	1%

Receiver

Sensitivity (10dB S/N ratio)	:	-86dBm
Noise	:	10µV
(Both in 3Hz to 80Hz bandwidth)		

Antenna

Gain	:	8dBi
-3dB Beamwidth		
E Plane	:	72°
H Plane	:	36°

Mechanical Characteristics

Weight	:	see table
Tab Connections	:	0.1" spacing

Environmental Characteristics

Power/Temp. Coefficient (over operating temp. range)	:	3dB
Frequency/Temp. Coefficient (over operating temp. range)	:	6.5MHz
Operating Temperature	:	-10°C to +55°C
Storage Temperature	:	-30°C to +70°C

Outline Drawings

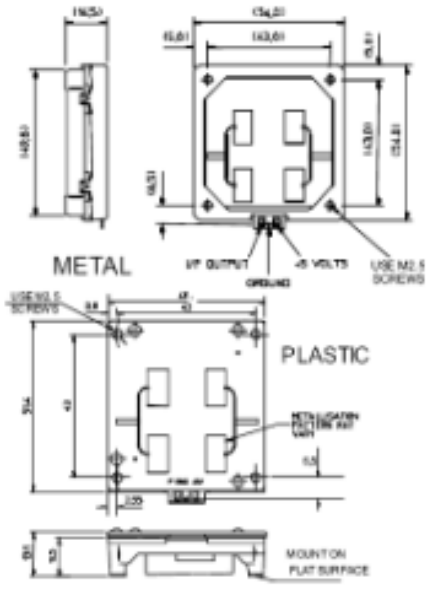

NOTES: Detection range is dependent on size and reflectivity of target and S/N ratio.
Doppler shift at 10.687GHz is 31Hz/m.p.h.
Unit functions over -30°C to +70°C but harmonics may exceed specified levels.

Model	Application	Order Code	Frequency	Weight	Comments
MDU1020	USA, Canada etc.	C900505 C900503 C900506	10.515GHz 10.525Ghz 10.535GHz	80 grams	USA FCC Part 15 Indoors Metal Housing
MDU1020	USA, Canada etc.	C900605 C900603 C900606	10.515GHz 10.525Ghz 10.535GHz	15 grams	USA FCC Part 15 Indoors Plastic Housing

Microsemi
Microwave Products
75 Technology Drive, Lowell, MA. 01851, 978-442-5600, Fax: 978-937-3748

K-MC4 MONOPULSE RADAR TRANSCEIVER

Datasheet

Features

- 24 GHz short range monopulse transceiver
- Dual receiver +/- 15° angle coverage
- Beam aperture 30°/ 12° @ -3dB
- 180MHz sweep FM input
- High sensitivity, integrated RF/IF amplifier
- Buffered I/Q IF outputs for both channels
- Temperature compensated oscillator
- RSW Rapid Sleep Wakeup for power saving
- Extremely compact: 78x98x7mm³ construction

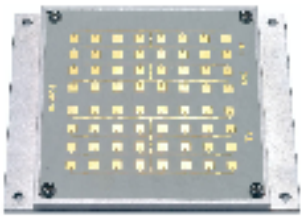

Applications

- Ranging, distance and direction finding measurements
- Traffic supervision and counting
- Object speed measurement systems
- Industrial sensors

Description

K-MC4 is a Doppler Transceiver with an asymmetrical beam and two receiver antennas. This configuration allows measuring the angle of moving objects. This technique is often simply called "Monopulse Radar", but in fact it is a "Phase-Comparison Monopulse" technique.
Target deviation of +/-15° from main axis results in a phase deviation of +/- 100° at the IF outputs I1/I2 or Q1/Q2 respectively.

The unique "RSW" Rapid Sleep Wakeup function with <5µs wakeup time makes this module ideal for battery operated equipment. Typical duty cycle in RWB mode may be < 1% with full movement detection capability by sampling the IF signals.
An extremely slim construction with only 6mm depth gives you maximum flexibility in your equipment design.
A powerful evaluation kit BT200 is available.

Blockdiagram

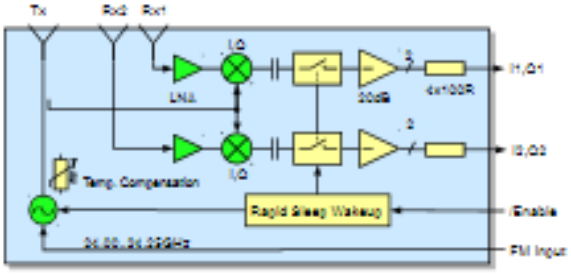

Fig. 1: K-MC4 Blockdiagram

Characteristics

Parameter	Conditions / Notes	Symbol	Min	Typ	Max	Unit
Operating conditions						
Supply voltage		V_{cc}	4.75	5.00	5.25	V
Supply current	Module enabled (Pin 1 = V_{cc})	I_{cc}		140		mA
	Module RSVI mode (Pin 1 = V_{cc})			5	7	mA
VCO input voltage		V_{VCO}	1		13	V
VCO pin resistance	Internal pullup to 5V	R_{VCO}		10K		Ω
Operating temperature		T_{op}	-20		+60	°C
Storage temperature		T_{st}	-30		+80	°C
Power down/Enable						
Module power down	Input tied high with pullup 100k	V_{pd}	V_{cc}-0.7		V_{cc}+ 0.3	V
Module enable		V_{en}	-0.3		2	V
Minimum enable time	RF- and IF-part fully functional	t_{en}	5			µs
Minimum duty cycle	Signal amplitude degradation < 3dB	t_{pr}	0.05			%
Transmitter						
Transmitter frequency	U_{cc}= 5V, T_{op}=-20°C .. +60°C	f_{Tx}	24.050	24.125	24.200	GHz
Frequency drift vs temp.	V_{cc}=5.0V, -20°C .. +60°C	Δf_{Tx}		-0.1		MHz/°C
Frequency tuning range (VCO)		Δf_{Tx}		150		MHz
VCO sensitivity		S_{VCO}		15		MHz/V
VCO Modulation Bandwidth	at=10MHz	B_{VCO}		21		MHz
Output power	EIRP	P_{Tx}	+16	+19	+20	dBm
Output power deviation	Full VCO tuning range	ΔP_{Tx}			+/- 3	dB
Spurious emission	According to ETSI 300 440	P_{SP}			-50	dBm
Receiver						
Antenna gain	F_{Tx}=24.125GHz	G_{Ant}		13.5		dBi
LNA gain	F_{Tx}=24.125GHz	G_{LNA}		16		dB
Mixer Conversion loss	f_{IF} =500Hz	D_{Mixer}		-12.5		dB
Receiver sensitivity	f_{IF} =500Hz, BW=1Hz, S/N=6dB	P_{Rx}		-116		dBm
Overall sensitivity	f_{IF} =500Hz, BW=1Hz, S/N=6dB	D_{sens}		-134		dBc
IF output						
IF output impedance		R_{IF-out}		100		Ω
IF amplifier gain		G_{IF-out}		30		dB
I/Q amplitude balance	f_{IF} =500Hz, U_{IF}=100mV$_{pp}$	ΔU_{IF}		3		dB
I/Q phase shift	f_{IF} =500Hz, U_{IF}=100mV$_{pp}$	β_{IF}	70	90	110	°
Amplitude balance Rx1 / Rx2	f_{IF} =500Hz, U_{IF}=100mV$_{pp}$, Object in front	ΔU_{IF}		3		dB
Phase balance Rx1 / Rx2	f_{IF} =500Hz, U_{IF}=100mV$_{pp}$, Object in front	β_{IF}		+/- 5		°
Monopulse resolution	Phase Rx1 / Rx2 divided by object angle 1	K		6.7		-
IF frequency range	-3dB Bandwidth	f_{IF}	15		200k	Hz
IF noise voltage	f_{IF} =500Hz	U_{noise}		1.0		µV/√Hz
	f_{IF} =500Hz	U_{noise}		-120		dBV/Hz
IF output offset voltage	V_{cc}=5.0V	U_{IF}	2.0	2.5	2.9	V
Supply rejection	Rejection supply pins to IF outputs, 1kHz	D_{supply}		10		dB

Note 1) Refer to chapter Object Angle Phase Conditions

Parameter	Conditions / Notes	Symbol	Min	Typ	Max	Unit
Antenna						
TX vertical -3dB beamwidth	E-Plane	W_E		12		°
TX horizontal -3dB beamwidth	H-Plane	W_H		30		°
RX vertical -3dB beamwidth	E-Plane	W_E		12		°
RX horizontal -3dB beamwidth	H-Plane	W_H		30		°
Horiz. sidelobe suppression		D_H		-20		dB
Vert. sidelobe suppression		D_V		-20		dB
Rx1, Rx2 mechanical distance		d_{Rx}		12.7		mm
Body						
Outline Dimensions	Connector left unconnected			86*79*7		mm³
Weight				90		g
Connector	Module side: JST P-2mm			8		Pins

Antenna System Diagram

This diagram shows module sensitivity (output voltage) in both azimuth and elevation directions. It incorporates the transmitter and one receiver antenna characteristic.

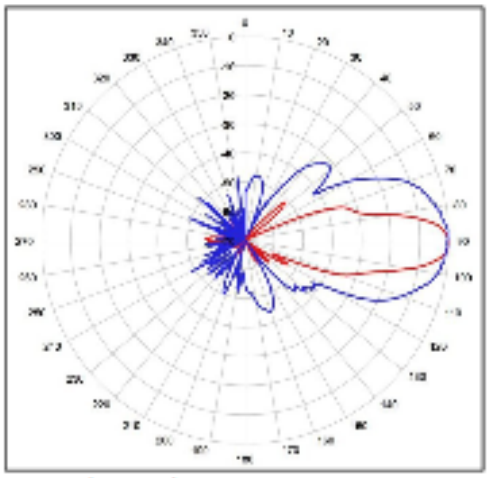

Azimuth 30°, Elevation 12°
At IF output voltage -6dB
(corresponds to -3dB Tx power)

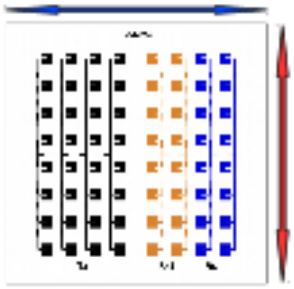

Fig. 2: Antenna system diagram